THERMAL SHOCK AND CFD STRESS SIMULATIONS FOR A TURBINE BLADE

by

Deepak Preabruth Ganga

Dissertation submitted in fulfilment of the academic requirements for the degree of Master of Science in Engineering in the School of Mechanical Engineering.

University of Natal

Durban

December 2002

ABSTRACT

A 2-D CFD / FEM model to simulate thermal stresses in a turbine blade has been set up using the software FLUENT and FIDAP. The model was validated against the data of Bohn et. al. (1995) and was used to simulate 5 test cases. The numerical model was set up for a single Mark II nozzle guide vane (NGV) and utilised the appropriate boundary conditions for the surrounding flow field. A commercially available software code, FLUENT, was used to resolve the flow field, and heat transfer to the blade. The resulting surface temperature profile was then plotted and used as the boundary conditions in FIDAP (a commercial FEM code) to resolve the temperature and stress profile in the blade. An additional solver within FLUENT essentially superimposes an additional flow field as a result of the NGV vibration in the flow field.

The pressure, temperature and heat transfer coefficient distribution, from FLUENT, were compared to those from Bohn et. al. (1995). The model predicted the distributions trends correctly, with an average over-prediction for temperature, of 10 % on the suction side and 6 % on the pressure side. This was restricted to the region from leading edge to 40 % chord on both sides of the blade. The blade temperature and equivalent stress contour trends were also correctly predicted by FIDAP. The blade temperature was over-predicted by and average of 1.7 %, while the equivalent stress magnitude was under-predicted by a worst case of 43 %, but the locations of maximum stress were correctly predicted.

The reason for the differences between the stresses predicted by FLUENT / FIDAP and the data given in Bohn et. al. (1995), is believed to be the results of the temperature dependence of the material properties for the blade (ASTM 310 stainless steel), used in the two studies, not being identical. The reasoning behind this argument is because the distribution trends and contour variation, predicted by the model, compared favourably with the data of Bohn et. al., and only the equivalent stress magnitude differed significantly. This completed the validation of the FLUENT / FIDAP model. The model was used to simulate test cases where temperature (i.e. turbine inlet temperature or TIT), at the model inlet (i.e. the pressure inlet boundary in FLUENT), was set up to be time varying.

Four simplified cases, viz single shock, multiple shocks, simplified cycle and multiple cycles, and a complex cycle (a mission profile) were simulated. The mission profile represented typical gas

turbine operational data. The simulation results showed that stress was proportional to TIT. Changes in TIT were seen at a later time in the stress curve, due to conduction through the blade. Steep TIT changes, such as the shock loads, affected stress later than gentler TIT changes – the simplified and multiple cycles. These trends were consistently seen in the complex cycle.

The maximum equivalent stress was plotted against TIT to try and develop a loose law that gives maximum equivalent stress as a function of TIT. A 4^{th} order polynomial was fitted through the maxima and minima of the maximum equivalent stress plot, which gave the maximum and minimum stress as a function of TIT. This function was used calculate the maximum and minimum and mean equivalent stress using the TIT data for the mission profile. Thus, the FLUENT / FIDAP model was successfully validated, used to simulated the test cases and a law relating the equivalent stress as a function of TIT was developed.

PREFACE

The author hereby states that this entire dissertation, unless specifically indicated to the contrary in the text, is his own original work, and has not been submitted in part or whole to any other University. This dissertation records the work carried out by the author in the Department of Mechanical Engineering at the University of Natal from January 2001 to December 2002. This project was supervised by Prof. S Govender and forms part of an ongoing study in the field of turbine blade heat transfer and thermal stress prediction.

"True wisdom lies is in knowing you know nothing"

- Socrates

... and if that fails

"Beer is proof that God loves us and wants us to be happy"

- Benjamin Franklin

... I dedicate this Thesis to my Father, the late P. S. Ganga

ACKNOWLEDGMENTS

The author wishes to acknowledge the following people.

My parents, for providing me with every opportunity they possibly could.

Jacques De Villiers and Andrew Bannerman for their friendship, support, and interesting commentary during the past 2 years.

Prof. Saneshan Govender for his guidance and supervision throughout the project.

Faisal Rahman and Danie de Cock at University of Pretoria for their input and assistance with the simulations.

Glenn Snedden at CSIR for providing the T56 Mission Profile.

CONTENTS

NOMENCLATURE

Acronyms

TIT	-	Turbine Inlet Temperature
CFD	-	Computational Fluid Dynamics
FEM	-	Finite Element
NGV	-	Nozzle Guide Vane
RANS	-	Reynold's Averaged Navier-Stokes
AMG	-	Algebraic Multigrid Method
FAS	-	Full Approximation Storage
LRN	-	Low Reynold's Number
HRN	-	High Reynold's number
CSD	-	Computational Structural Dynamics
CMD	-	Computational Mesh dynamics
UL	-	Updated Legrangian

Symbols

T	-	Temperature
t	-	Time
x	-	Axial chord and x-coordinate direction where specifically indicated
y	-	y-coordinate direction
z	-	z-coordinate direction
L	-	Axial chord length and cylinder length where specifically indicated
D	-	Cylinder diameter
r	-	Cylinder radius variable and r-coordinate direction
θ	-	θ-coordinate direction
y^+	-	Non-dimensionalised distance from the wall
R	-	Cylinder outer radius
Re	-	Reynold's number
Re_x	-	Reynold's number based on axial chord
Re_y	-	Turbulent Reynold's number
a	-	FLUENT meshing parameter – first cell height
GR	-	FLUENT meshing parameter – growth rate
Rows	-	FLUENT meshing parameter – number of rows
M	-	Mach number
Mexit	-	Exit mach number

Cp	-	Specific heat
k	-	Turbulent kinetic energy and thermal conductivity where specifically indicated
E	-	Young's Modulus unless specifically indicated to the contrary
ρ	-	Density
μ	-	Viscosity
ν	-	Poisson's ratio
α	-	Volumetric Expansion Coefficient
γ	-	Specific heat ratio and thermal diffusivity coefficient where specifically indicated
σ	-	Stress

Subscripts

x	-	x-coordinate direction
y	-	y-coordinate direction
z	-	z-coordinate direction
r	-	r-coordinate direction
θ	-	θ-coordinate direction
Nr	-	Non-dimensionalised in the r-coordinate direction
Nθ	-	Non-dimensionalised in the θ-coordinate direction
Nz	-	Non-dimensionalised in the z-coordinate direction
s	-	Cylinder surface
i	-	Cylinder centre
e	-	Equivalent

CHAPTER 1
INTRODUCTION

The propulsion gas turbine engine used in modern aircraft boasts higher power to weight ratios and efficiencies than any reciprocating engine. However, in comparison to reciprocating engines, gas turbine engines are far more expensive. It is for these reasons that its use is limited to areas, such as propelling aircraft, where its performance justifies the cost. The basic layout of a gas turbine engine is shown in Figure 1-1 and the schematic diagram in Figure 1-2, with the main components being the compressor combustor and turbine.

The performance of the engine is directly related to the temperature of the gas entering the turbine – referred to as the turbine inlet temperature or TIT (temperature at point 4, in Figure 1-2). Increasing the TIT, by adding more fuel thereby increasing the heat input to the engine (q_{in}), and increases the overall performance of the engine. Equations A-1 to A-10 (Appendix A) show the basic thermodynamic calculations for each process in the engine, including the inlet diffuser and exit nozzle not shown in Figure 1-2. Using these calculations, one may determine, (hypothetically) that the best engine requires a TIT of 4000 K. This is physically impossible since this exceeds the melting point of any alloy presently known.

While metallurgists try to develop alloys that can withstand higher operating temperatures, gas turbine designers have tried to push the TIT limit by developing ways to cool the turbine blades. Blade cooling is achieved in one of two ways - internal cooling or film cooling, both using cold air bled from the compressor. Film cooling ejects the cold air into the hot gas stream creating a layer of cooler air around the blade. Internally cooled blades have internal serpentine passages through which the cold air flows, creating a temperature gradient within the blade to conduct the heat away from the surface.

Part of the process of improving the thermal design of turbine blades is to determine the heat load created by the hot gas stream moving over the blade. Computing the heat transfer to the blades is by no means a trivial task. Turbine blade flows are complex enough being three-dimensional and unsteady, but for the heat transfer calculation, one must also account for the effects of free stream turbulence, boundary layer transition, separation and reattachment, shock waves and main flow acceleration and deceleration. Numerical solutions for the flow and heat transfer play an integral role in turbine blade design and has been the focus of intensive research over the last 30 years. The development of numerical codes for predicting flow and heat transfer

was accompanied by advancements in heat transfer measurement techniques to produce quality data for the purpose of validating the numerical codes. Presently, the state-of the-art of numerical heat transfer prediction has advanced to the point were numerical codes are used with confidence in the design process.

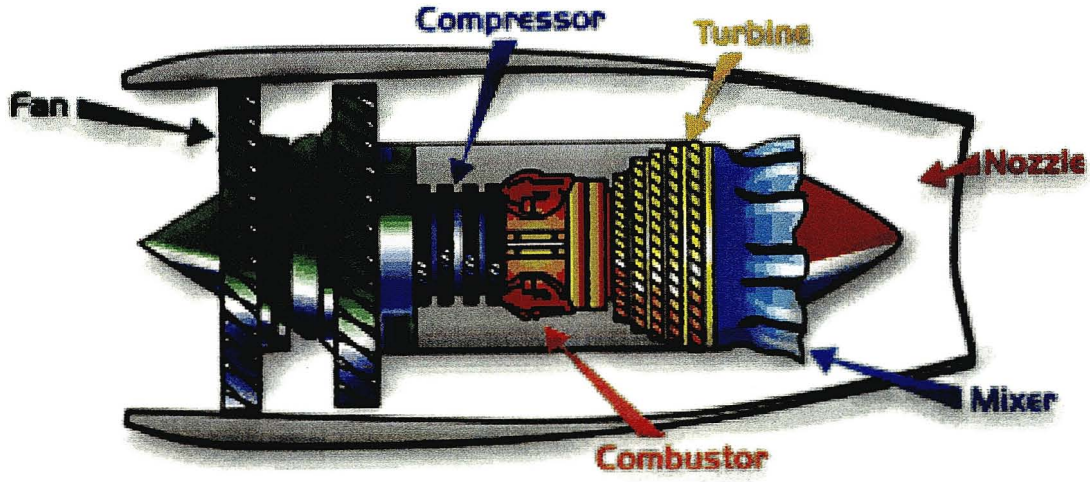

Figure 1-1: Layout of the components of a gas turbine engine, reproduced from the Ultra Efficient Engine Technology (UEET) website

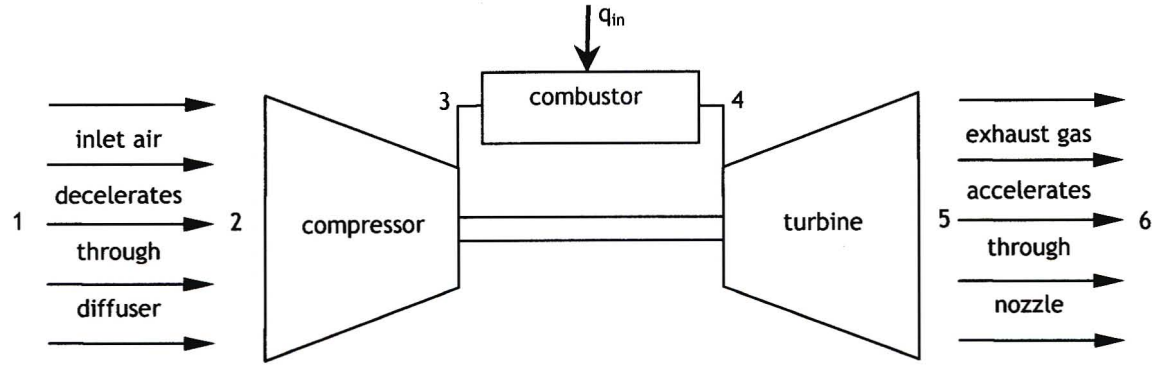

Figure 1-2: Schematic layout of the gas turbine engine components

Operating a propulsion gas turbine engine is extremely expensive, and the user aims to minimise the engine maintenance downtime and more importantly avoid catastrophic failure of any of the hot-gas-path components. Engine health monitoring and life assessment plays an important role in determining the degree of degradation and wear in an engine and assists users

in strategically planning maintenance action. The strategy of engine monitoring is to assess the condition of an engine and its components through dependant measurable parameters such as pressures and temperatures, and independent non-measurable such as efficiencies, flow rate and thrust.

This kind of assessment is only possible if it is known, a priori, the effect that the different kinds of degradation have on the measurable and non-measurable parameters, not only for the entire engine but also on a component level. Quantifying the effect of degradation in terms of measurable and non-measurable parameters, within a component (the turbine blades for example), is the first step. The analysis can then expand to the component and finally, the entire engine.

Turbine blades, in particular the first stage, suffer the brunt of the hot combustor gas, and blade cooling is a necessity. Internal cooling results in large temperature gradients within the blade, which leads to high thermal stresses. The gas temperature that the blades are exposed to varies during an aircraft's flight. The record of the TIT during a flight is referred to as the mission profile. At startup, the blades, which are at ambient temperature, are suddenly struck by a gas stream of rapidly increasing temperature, which can rise from ambient to as much as 2000 K in as little as 30 seconds. The TIT will then vary during the mission depending on what the pilot does with the throttle.

Due to the unsteady nature of the TIT, one can expect the thermal stresses within the blade to also be unsteady which can cause the formation of thermal fatigue cracks and eventually result in structural failure of the blade. From the engine monitoring perspective, if one can quantify the thermal fatigue life of the blades in terms of TIT then monitoring the TIT will allow engine user to asses the extent of fatigue cracks without having to ground the aircraft and remove the engine for inspection. Thermal fatigue data of this kind can be obtained from experimentation, where blades, exposed to flows that mimic actual engine operation, are tested to the point of failure, or by thermal fatigue life calculations. The accuracy of the thermal fatigue life calculations depends on the thermal stress used in the calculations. If the thermal stresses quantitatively represent those that would be found in the blades, then the fatigue calculations would be more accurate.

A major step toward achieving this would be to determine the thermal stresses that occur in a blade for an entire mission profile. With the advanced state of numerical prediction techniques (thanks to the intense development over the last 30 years fuelled by the need to raise the maximum allowable TIT) and the improved capability of modern day computers, it is possible

to obtain a numerical solution for realistic turbine blade thermal stresses. This dissertation discusses the development of a CFD model using a commercially available numerical code to simulate thermal stresses in a turbine blade with unsteady inlet flow temperatures.

The numerical aerodynamic and thermal analyses were done using the codes FLUENT and FIDAP respectively. The first part of the work was to validate the codes, which was done using data from the available literature. Finding suitable data proved to be more difficult than was first anticipated. Very little work involving turbine blade thermal stress prediction has been published in the open literature, and those that do relate to the topic were either steady state analyses or focused in thermal fatigue calculations and did not do an in-depth analysis into the quality of the thermal stress data used in the fatigue calculations. The findings of these studies were useful in developing the CFD model of a turbine blade and the data therein had to be used to validate the model, as it was the only data available.

The CFD model was developed using the geometry of the stationary inlet nozzle guide vane known as Mark II. Steady state aerodynamic and thermal data was available for this blade and was used to validate the FLUENT and FIDAP solutions. FLUENT was used for the aerodynamic analysis and resolved the flow field and heat transfer on the blade surface. FIDAP was used for the thermal analysis and solved the internal blade temperature and thermal stresses. The CFD model with the Mark II NGV configuration was used to simulate four simplified unsteady test cases and a representative mission profile, which represented a complex cycle.

The TIT profiles for the simplified test cases were derived using the mission profile from a T56 engine on a C130 cargo plane, which was used for the complex cycle simulation. The simplified test cases were for a simple shock load and a simplified mission profile. The maximum equivalent stress that occurred in the blade was plotted against time, together with the TIT profile for that cycle. This plot gave an indication as to how the maximum stress varied with TIT. For the complex cycle, the predicted stress data was plotted against TIT, and a 'loose law' (in the form of a fitted polynomial curve) that approximates the maximum equivalent stress an a function of TIT was developed. The maximum equivalent stress profile for the complex cycle was calculated using the polynomial approximation and the result compared very well with the prediction from the CFD.

In the following chapters of this dissertation, the literature that was surveyed during the study is reviewed. The development of the CFD model of a turbine blade is detailed and an overview of the codes used, is outlined. Thereafter, the validation of the CFD model is discussed in detail, and finally the results of the thermal stress simulations for the unsteady test cases are discussed.

CHAPTER 2
LITERATURE SURVEY

An early examination of available gas turbine literature revealed the endless extent of research in the gas turbine field. It was also discovered, to the author's dismay, that the literature relating to turbine blade thermal stress prediction was severely limited. The extent of the available literature dealing specifically with turbine blade aerodynamics and heat transfer was also incessant, but finding thermal stress literature and heat transfer literature for the same turbine blade profile was again difficult. Even more difficult was finding literature that gave the geometric configuration of a blade, for which, one could also find heat transfer and thermal stress data.

The literature on aerodynamic and heat transfer prediction is vitally important since the flow problem is far more complex than the thermal stress problem. Research into turbine blade heat transfer was fuelled by the need to up the maximum allowable TIT and thereby increase the performance and efficiency of the propulsion gas turbine engine. The intention of the research was the development of CFD codes that can accurately predict the flow and heat transfer in a gas turbine. The development of such codes has been ongoing since the early 1970's and even though significant progress has been made over the last 30 years, the state-of-the-art is not yet at a stage where the complexity of real turbine blade flows can be completely and correctly represented mathematically.

This literature review will cover thermal stress literature first and then get into the complex world of turbine blade heat transfer prediction. The end users of the research discussed in this dissertation will be the gas turbine maintenance and life assessment sector. It is thus appropriate that this literature review begins with the keynote paper, Singh (1999), which outlines the gas turbine life assessment and engine monitoring research that has been done at Cranfield University in the United Kingdom, but of more importance to this dissertation is the overview of engine monitoring that is given. An outline of the role that the work discussed in this dissertation will play in the engine monitoring arena was given in the Introduction of this dissertation.

An early study of turbine blade thermal stresses was done by Maya et. al. (1978). This paper represents the idea embraced by the work in this dissertation. Maya performed a thermal fatigue analysis for a turbine blade for the cases of engine acceleration and deceleration. Of interest to

the present study, is the method by which the unsteady thermal stress profiles where obtained. First, a FEM prediction was done for the 2-D steady and unsteady internal blade temperature profile. The boundary condition for the simulation was of a convection type requiring a surface heat transfer coefficient distribution and a free stream temperature – the TIT profiles for the acceleration and deceleration cases.

The predicted internal blade temperature distribution was used as the boundary condition for the 3-D FEM prediction of the unsteady thermal stresses. The temperature distribution was assumed to be constant in the spanwise direction. Maya showed that thermal stresses were as a result of the chordwise blade temperature distribution, which were six to seven times greater than the spanwise distribution. The maximum stress was determined to be at the leading edge, and was represented as the stress component in the z-coordinate direction, which was ten times larger than the other two components.

The unsteady stress component in the z-coordinate direction was used as the boundary condition in the thermal fatigue analysis. Maya's thermal fatigue calculations were compared to and were in fair agreement, with experimental thermal fatigue test data for the blade. The data in this paper would have been useful for validating the CFD model if the geometric configuration was known, even though a CFD analysis was not done, but instead the TIT applied to the blade surface directly. It was unfortunate that Maya et. al. (1978) was only obtained during the latter stages of the research. A more recent study, Swaminathan and Allen (1995), also performed thermal fatigue experiments on cooled turbine blade. Again the data could have been useful if sufficient information was given to allow the problem to be reproduced in a numerical code. Not in its favour is the fact that no discussion of the flow conditions was given and no thermal calculation, numerical or otherwise, was done.

A paper directly relating to the present study was Bohn et. al. (1995). In this paper, a numerical solution for turbine blade thermal stresses, using a combined aerodynamic and thermal analysis is given. Unlike Maya et. al. (1978), Bohn et. al. (1995) did not simplify the problem by applying the TIT to the blade surface, instead, a CFD analysis was done for a blade cascade. The analysis showed that the surface temperature is not only, different from the TIT but also not spatially uniform along the surface due to the effect of aerodynamic features in the flow and boundary layer.

Bohn's analysis was done for a Mark II NGV cascade, for which additional aerodynamic data in the literature - Hylton et. al (1983) and Nealy et. al. (1984) - was found. More importantly, the geometric configuration for the Mark II cascade was given and the problem was sufficiently

defined allowing it to be reproduced. The numerical analysis for the flow field solved the Navier-Stokes equations with the Baldwin-Lomax algebraic turbulence model using the finite volume form of the governing equations. Bohn et. al. (1995) compared the CFD predictions with the experimental data of Hylton et. al. (1983). The thermal analysis solved the internal blade temperature and stresses using the finite element method. An in-depth discussion of the numerical procedure, computational grid, boundary conditions and the predicted results was given.

Even though the analysis was steady state only, the completeness of the data presented by Bohn et. al. (1995) warranted its use in validating the CFD model. A detailed discussion of Bohn's data is given in chapter 4 of this dissertation where the validation of the CFD model is discussed. From Bohn's analysis and from the heat transfer literature in general, it is clear that an accurate thermal stress prediction is only possible if the flow field is first accurately resolved to determine the temperature distribution on the blade surface. The complex physics off the flow must be well predicted if its effects on the predicted heat transfer are to be considered thus emphasising the importance of an accurate flow field and heat transfer prediction. An understanding of numerical prediction for turbine blade flows is therefore necessary.

The available literature on turbine blade heat transfer prediction and its related topics is so vast that a young researcher entering the field will quickly discover that finding a suitable starting point may seem impossible, but all is not lost! An incredibly useful recent paper, Dunn (2001), reviews the progress of turbine blade aerodynamics and heat transfer research over the last 30 years. This review brings together the progress of many of the research programs that were run by different organisations and contains 489 references.

It documents the progress from the early days of plain cascade measurements and the predictions using the original form of the Boundary-Layer code STAN 5 to the more recent fully instrumented rotating rig experiments and predictions using 3-D Boundary-Layer and 3-D Navier-Stokes codes. This literature survey will focus more on numerical code development and prediction and will also comment on the experimentation that accompanied the code development. Progressive development of numerical codes was also accompanied by advancements in heat transfer experimentation used to validate the codes' predictions. Numerical code development was also accompanied by advancement in numerical techniques and turbulence modelling.

A discussion of turbine blade heat transfer cannot be attempted without discussing experimental data and turbulence modelling. The author has set out the following literature survey on heat

transfer prediction to chronologically document the development of the state-of-the-art. By the mid 1970's, the mathematical treatment of turbulence had not advanced enough to allow full Navier-Stokes solutions for turbine heat transfer. Common practice was to obtain surface pressures by solving the bulk flow using an inviscid Navier-Stokes or Euler code, and use the pressure and velocity fields as boundary conditions for the heat transfer calculation in a Boundary-Layer code. Intensive experimentation was also underway by the mid 1970's and one of the early pioneers of quality data was Langston et. al. (1977) who performed aerodynamic measurements in a subsonic plane turbine cascade.

Brown and Burton (1978) experimentally investigated the effect of free stream turbulence intensity and velocity distribution on heat transfer to curved surfaces. The findings were that heat transfer increased with increasing turbulence intensity for a lamina boundary layer region but was unaffected in a turbulent boundary layer. The point at which transition occurred was found to be sensitive to free stream turbulence intensity, velocity distribution and Reynold's number. Dunn and Stoddard (1979) performed heat transfer experiments on a sector of the first stage stationary inlet nozzle of an AiResearch TFE-731-2 test engine using thin film heat transfer gauges.

One of the early papers that compares experimental data with predictions was Graziani et. al. (1980). Graziani performed 3-D heat transfer measurements using the Langston cascade and compared the mid-span results to predictions done using the Boundary-Layer code STAN 5 developed by Crawford and Kays (1976). The Graziani data showed good agreement with the experimental data of Blair (1974), and the mid-span pressure distribution and Stanton numbers predicted using STAN 5 compared well with the experimental data. Graziani's data is considered to be a quality data set for the purpose of code validation, and is referenced in many other papers.

Daniels and Browne (1981) used 5 different computer programs, each using a different turbulence model closure for the boundary layer equations, to calculate heat transfer rates to gas turbine blades and compared the results with the experimental data of Daniels (1978). By this time, significant advancement had been made in the area of turbulence modelling for a number of different models to be tested. The 5 models used where the Cebeci-Smith (1974), Patankar-Spalding (1970), Cebeci-Smith-McDonald, Wilcox 'EDDYBL' and Wilcox (W-T) model. The Cebeci-Smith model calculated the Reynold's stress terms using a mean field turbulent model and the eddy viscosity using Prandtl's mixing length model.

In the Cebeci-Smith-McDonald program, the Reynold's stress is calculated using a mixing length, dissipation of turbulent kinetic energy is modelled using a dissipation length scale and turbulent kinetic energy in the boundary layer is calculated with a one-equation model. Patankar-Spalding also uses mixing length and eddy viscosity models but include and experimentally derived turbulence model. The Wilcox 'EDDYBL' program is based on the two-equation k-ω model of Wilcox (1975) and the Wilcox (W-T) model uses tabular values for the turbulent Prandtl number (Pr_t).

The predictions of all five programs showed good agreement with the Daniels experimental data in the lamina and fully turbulent regions on the suction surface but poor agreement in the transition region on the suctions surface and on the entire pressure surface. With no difference between the one and two-equation models, Daniels and Browne concluded that there was no advantage in a using complex turbulence model. Dunn and Hause (1982) furthered the work of Dunn and Stoddard (1979) by performing heat transfer measurements on a section of a complete stage (stationary inlet nozzle, shroud and rotor). The study showed that the heat transfer rate for the stator-only measurements were less than that for the full stage implying that the presence of the rotor affected the heat transfer to the upstream stator. The data set was also considered to be a quality set for code validation since the flow conditions were well defined. The influence of the rotor on the upstream vane heat transfer was further emphasised by Dring et. al. (1982).

Hylton et. al. (1983) and Nealy et. al. (1984) performed heat transfer measurements in a 3-vane cascade for the Mark II NGV and the C3X blade. The study investigated the effect of Reynold's number, and exit Mach number on the surface pressure and heat transfer distributions. Predictions were done using a time-dependant, transonic, inviscid cascade code and a version of STAN 5 modified to include zero-order turbulence modelling. The predictions show reasonably good agreement with the experimental surface heat transfer coefficient distributions. The Nealy paper proved to be very useful and with the flow conditions well defined, falls in the same quality data category as Graziani et. al. (1980) and Dunn and Hause (1982). The Mark II NGV data from Nealy et. al. (1984) was used in the validation of the CFD model.

The work done by Dunn and Stoddard (1979) and Dunn and Hause (1982) on the TFE-731-2 engine, was furthered by Dunn et. al. (1984). Therein were reported heat flux measurements on a sector of a full stage and presented predictions made using STAN 5 and a code developed by TDS (Turbine Design Systems). The heat flux data were presented as Stanton number distributions and were the experiments were carried out for different wall to gas temperature ratios (T_w/T_g). The TDS predictions showed satisfactory correlation for the NGV and rotor

pressure surface but poor correlation on the rotor suction surface. The STAN 5 predictions were generally good, but the heat flux was consistently under-predicted on the NGV and rotor.

A solution for 3-D turbulent flows using the compressible Navier-Stokes equations was presented by Hah (1984). The numerical procedure used a control volume based formulation of the governing equations with an algebraic Reynold's stress turbulence modified for the effects of streamwise curvature and rotation. The predictions were compared with the aerodynamic analysis of Langston et. al. (1977). The numerical solution was in excellent agreement with Langston's data for 50 % blade span.

Wang et. al. (1985) incorporated a low Reynold's number version of the k-ε two-equation turbulence model of Jones and Launder (1973) into the 2-D Boundary-Layer code STAN 5. A two-zone model was used to treat the k and ε variables in the near-wall (low Reynold's number) region. The heat transfer predictions were done for a plat plate, the C3X blade and the Turner airfoil and compared with the experimental data of Hylton et. al. (1983) for the C3X blade and Turner (1971) for the Turner airfoil. For the C3X blade, the heat transfer predictions using the low Reynold's number of the k-ε two-equation turbulence model were better than the mixing length turbulence treatment used by Hylton. The overall heat transfer trends were well predicted except at the leading where Wang's solution over-predicted the heat transfer.

The heat transfer for the Turner airfoil was well predicted except at the trailing edge. It was argued that the overall heat transfer prediction could be improved if a better velocity field was used at the boundary layer edge in the Boundary-Layer code. The leading edge heat transfer was not over-prediction because the inlet Reynold's number for the Turner airfoil was much lower than that for C3X blade. The flow for the Turner airfoil was therefore slower than for C3X blade resulting in a thicker viscous sub-layer thereby explaining the better performance of the low Reynold's turbulence model. A finite difference formulation, using the Prandtl mixing length model of turbulence, was used by Moore and Moore (1985) to compare the performance of two, geometrically similar turbine cascades. As was seen in Wang et. al. (1985), the predictions with a mixing length model presented in Moore and Moore (1985) was not in as good agreement with the experimental data of Langston et. al. (1977).

A low Reynold's number version of the k-ε turbulence model developed by Lam and Bremhorst (1981), was used by Rodi and Scheuerer (1989) to predict turbine blade heat transfer using the finite difference form of the boundary layer equations. The Lam-Bremhorst model was used because of its apparent ability to predict transition and its suitability for near-wall flow due its

low Reynold's number nature. The predictions were compared with those of Daniels and Browne (1981). The pressure surface heat transfer was well predicted and the on the suction surface, the heat transfer for the fully lamina and turbulent was also well predicted. The transition region heat transfer was in fair agreement with the data. Thus far, it appears that the low Reynold's number turbulence models work well when used to provide closure for the boundary layer equations, but does not provide adequate closure for a Navier-Stokes solution.

Joslyn and Dring (1992 – Parts I and II) carried out an experimental aerodynamic study on a one and half stage (stator and rotor – 1 stage, and stator of the following stage). The study aimed at developing an improved understanding of the 3-D nature of turbine blade flow with the intention of it leading to and improved ability to predict 3-D flows. The measurements were compared with the 3-D, compressible, viscous, time accurate, full stage Navier-Stokes predictions of Rai (1987) and Adamczyk et. al. (1990). The predictions were in excellent agreement with the measured data. The study not only produced quality, 3-D, full stage experimental data but also showed that full Navier-Stokes solutions for full stage and multistage turbine flows can produce excellent aerodynamic predictions.

By the early 1990's, CFD codes had advanced to the point were steady 3-D predictions of full stage turbine blade rows, using either viscous Navier-Stokes codes or the practice of a combined inviscid Euler and Boundary-Layer codes, were possible. The true test of a CFD code is to be able to predict the unsteadiness in the flow that is present in real turbines. Cascade experiments produced data that allowed code developers to assess the prediction of fundamental flow physics, but were unable to reproduce realistic operating environments. Full stage and multistage experiments brought about improved understanding of the three dimensional nature of the flow and provided an avenue for realistic, unsteady experimentation. Up to that point, Navier-Stokes solutions of unsteady 3-D flows were restricted by the turbulence model limitations and limited computational capability of computers at the time.

Sharma et. al. (1992) assessed the impact of unsteadiness on turbine blade flows and discussed the ability of both experimentation and prediction in realistically capturing the unsteady features. The unsteady features identified were upstream temperature streaks and vortices that result from rotor-stator interaction. Earlier studies, such as Hah (1984) showed that Navier-Stokes codes with wall functions and Euler codes incorporating aerodynamic loss models were capable of defining the flow through turbine blade rows. Sharma showed that 3-D multistage flow prediction was accurate in the presence of unsteady flow features, but the effect of upstream temperature unsteadiness was not well predicted. The results were promising and it

was concluded that further development in both Navier-Stokes and Euler codes would lead to increased accuracy for unsteady 3-D multistage flows.

In contrast, Dunn et. al. (1992) performed pressure measurements on the vane and blade of transonic turbine stage, which show only reasonable agreement with Rao and Delaney's (1990) predictions from an unsteady Euler and an unsteady Navier-Stokes code. The latter years of code development have shown increased interest in the Navier-Stokes solutions for turbine blade aerodynamic and heat transfer predictions. The main drawback of using Navier-Stokes codes was the large computational grid density required the resolve the viscous affected regions. The consequence of completely resolving the flow field is the large computational resources and solution time required.

Advances in modern day computers have allowed the use of finer grids leading to more accurate solutions. Dorney and Davis (1992) provide an excellent review of the development of 3-D Navier-Stokes predictions and established computational grid density requirements for accurate heat transfer predictions. An important aspect of a Navier-Stokes solution is the choice turbulence closure model. Previous investigations with the k-ε turbulence model (Chan and Sheedy 1990 and Hah 1984, 1989), the low Reynold's number q-ω model (Lee and knight 1989) and an algebraic mixing length turbulence model (Moore and Ransmayr 1984 and Moore and Moore 1985) have shown only fair agreement with experimental data.

Dorney and Davis employed the Baldwin-Lomax algebraic turbulence model, and showed agreement with experimental data that, in general, was better than the previous studies. The predicted 3-D pressures were only 4 % larger than the measurements of Graziani et. al. (1980). The heat transfer was, in general, well predicted. It was shown in the experiments that on the suction surface, transition occurred at 25 % chord. The Stanton numbers were well predicted ahead of the transition point but were under-predicted after transition. The predicted 3-D Stanton numbers on the pressure surface showed only fair agreement with the data. It was concluded that no general formula could be proposed for the optimum grid density and that full span grid resolution of 900000 grid points should only be used as a guide. The Baldwin –Lomax algebraic turbulence model produced comparable results but accurate heat transfer prediction will only be realised with a model that can accurate predict lamina to turbulent transition.

Previous work in the research program involving Dunn had reached the stage were measurements and prediction were done for one full stage of vane-blade rows. Dunn et. al. (1994) extended this research to two full stages of vane-blade rows. The measurements were done to compare the predictions of a version of STAN 5 (Gaugler 1981), modified to include

the Dunham transition model, and a quasi 3-D Navier-Stokes code (Chima 1986). The Navier-Stokes code incorporates the transition model of Mayle (1991) and the boundary layer edge condition for STAN 5 was obtained using the inviscid code TSONIC.

The STAN 5 prediction was generally in good agreement with the data though the prediction under-predicted the data beyond the point of transition. This trend was seen previously in the analysis by Nealy et. al (1984). Dunn attributed the under-prediction to the flow not becoming fully turbulent with the Dunham transition model. The Navier-Stokes prediction with the Mayle transition model agreed better with the data. The difference between STAN 5 and the Navier-Stokes predictions was more pronounced for low Reynold's number flows than for high Reynold's numbers. This is most likely because for high Reynold's numbers, transition occurs close to the leading edge, making the flow fully turbulent over almost the entire blade.

A very recent and useful paper, Adamczyk (2000), gives a review of current 3-D CFD models for time-averaged flow predictions. Adamczyk gives an in-depth discussion on the development of mathematical models from the simple mean flow governing equations through the averaged – passage model and Reynold's averaged Navier-Stokes equations to the present day state-of-the art of full Navier-Stokes solutions. Relating more to the finite volume code used in this dissertation - FLUENT, De Villiers (2001), reviewed the turbulence models available in FLUENT for predicting cascade flows. De Villiers performed aerodynamic measurements for the SMR-95 turbine blade using a supersonic cascade rig at the University of Natal, and compared the data with predictions done in FLUENT using the different turbulence models. De Villiers concluded that the one-equation Spalart-Allmaras model (Spalart and Allmaras 1992) did not perform as well as the Realizable k-ε turbulence model (Shih et. al. 1995) with a two-zone model for the near-wall treatment.

The state-of-the-art of turbine blade heat transfer prediction has significantly advanced over the last 30 years, yet cannot boast a numerical code with the universal ability to accurate predict the flow and heat transfer through an entire gas turbine. This is purely because of the complex nature of turbulent flow that renders complete mathematical treatment of it almost impossible. A single universal turbulence model that can mathematically define all the complexities of turbulent flow is still unlikely. The advancements in turbulence modelling have resulted in a number of variations that between them can cater for almost all the unsteadiness in gas turbine flows.

The model that is closest to being universal is the k-ε turbulence model of Jones and Launder (1973). This has made it attractive to researchers and many have made modifications to handle

the viscous affects of near-wall flow, effects of free stream turbulence, transition, separation and reattachment etc. Some of the literature worth noting, that review turbulence modelling are Blair (1982), Rhie and Chow (1983), Hodson (1985), Patel et. al. (1985), Chen and Patel (1988), Schmidt and Patankar (1991, Parts I and II), Mayle (1991) and Menter (1994).

The author consulted various textbooks to obtain a fundamental understanding of the science encountered in the study. The principles governing fluid flow and heat transfer were adequately covered by Edwards et. al., Incropera and De Witt (1990), Myers (1987), Osisik (1980), Roshenow et, al., Zukausha and Slanciauskas (1987), Temam (1977), Frost and Moulden (1977), Schlichting (1955), Chia-Shun Yih (1969), Binder (1958), Prandtl (1969), White (1974), Patankar and Spalding (1970), and Hinze (1959).

CFD codes use numerical techniques to solve flow and heat transfer problems. Using these codes without an understanding of the numerical techniques is unwise, and is why the author consulted Abbot, Baker (1976), Cuvelier et. al. (1986), Patankar, and Connor (1976), to develop a fundamental understanding of the numerical solution process.

CHAPTER 3

DEVELOPMENT OF THE CFD MODEL OF A TURBINE BLADE

The numerical procedure presented by Bohn et. al. (1995) (hereafter referred to as Bohn), i.e. a combined aerodynamic and thermal analysis, proves to be a valuable tool that will aid turbine designers in optimising the thermal design of turbine blades. The aerodynamic analysis was done using a finite volume (FV) code and the thermal analysis with a finite element (FEM) code. The earlier investigation by Maya et. al. (1978), demonstrated the ability of FEM to predict turbine blade thermal stresses. Maya et. al. (1978) calculated the unsteady thermal stresses for the cases of rapidly increasing and decreasing TIT - indicative of engine acceleration and deceleration. The unsteady thermal stresses were used in a thermal fatigue analysis to determine crack growth and the results compared sufficiently well with experimental thermal fatigue test results of the time to be considered accurate.

Maya et. al. (1978) simplified the FEM boundary conditions for the unsteady calculation by assuming a fixed surface heat transfer coefficient distribution and imposed the time varying TIT as the blade surface boundary condition. This simplification was acceptable for the simple acceleration and deceleration cases. For more realistic TIT changes, the resulting unsteady surface heat transfer must be accounted for if the results are to be considered realistic. Swaminathan and Allen (1995) - and the open literature in general - comments that accurate prediction of surface heat transfer distribution is necessary to accurately predict the blade surface temperature distribution. This in turn results in accurate prediction of the internal blade temperature and stress distribution.

By performing a combined aerodynamic and thermal analysis, one takes into account the aerodynamic effects on surface heat transfer and temperature, thereby giving a more realistic solution for the internal blade temperature. Bohn's procedure can be extended to simulations were the TIT is unsteady as most present day CFD solvers are fully capable of simulating unsteady flows. The unsteady aerodynamic analysis will yield the resulting unsteady surface temperature distributions. Using these as the boundary condition in the thermal analysis will give the unsteady internal blade temperature and stress distribution.

The shortfall of the procedure does become evident when trying to impose the unsteady surface temperature boundary condition in the FEM analysis. Because of the complex nature of even 2-D unsteady turbine blade flow, the unsteady blade surface temperature distribution is expected

to not only vary with time, but also spatially along the blade surface. It is thus apparent that if the governing flow and stress equations were discretized by the same formulation, then the two sets of discrete equations could be coupled via the blade temperature.

During the solution process, even for unsteady flows, the stress equations will be continuously updated with the unsteady temperatures thereby allowing the computation of unsteady blade thermal stresses resulting from an unsteady TIT. It was for this reason that the decision to try and use FIDAP - a commercially available FEM code - for the thermal shock simulations was taken. Version 8.5 of FIDAP was equipped with Fluid-Solid-Interaction (FSI) capability. FSI referrers to problems were deformation and stresses in a solid body are the result of the action of a surrounding flow field. FIDAP 8.5 has made FSI simulations a reality by using FEM formulation for all the governing equations of a problem. The fluid and solid equations are coupled by a common variable, this being the temperature for the turbine blade thermal stress problem.

An initially review of the FIDAP literature indicated that FIDAP contained all the models and tools necessary for performing the thermal shock simulations. The author proceeded to set up and validate the FIDAP CFD model using the data of Bohn's investigation for the Mark II NGV. After numerous failed attempts at running a simulation, it was discovered that while FIDAP is capable of solving a wide range of flow, structural and FSI problems, it is incapable of simulating supersonic and transonic flows, and flows with severe changes in density. The data for the Mark II NGV showed that the flow is transonic and with the fluid being air, which is compressible, has its density as a function of pressure and temperature. Thus, FIDAP could not be used to set up a CFD model to simulate both the flow field and thermal stresses, but could be used for the thermal analysis.

Based on these findings, the CFD model for the thermal shock test cases would have to carry out a combined aerodynamic and thermal analysis. The commercial finite volume (FV) code – FLUENT 6.0 was available for the aerodynamic analysis, and it was decided that FIDAP would be used for the thermal analysis. For the aerodynamic analysis, the blade and the flow field must be modelled, while only the blade is modelled in the thermal analysis. Bohn comments that one of the problems in a combined aerodynamic and thermal analysis is the change in computational grids between the FV and FEM codes. This problem is overcome by using FLUENT and FIDAP because the computational grids for both are created in the same geometry and mesh generator called GAMBIT. This would guarantee identical grids on the blade in both solutions.

3.1. FLUENT – An Overview

Numerical simulation of even steady state 2-D turbine blade aerodynamics with heat transfer is a complex issue. Flow features such as boundary layer transition, free stream turbulence, mainstream acceleration and deceleration, flow separation and reattachment and shockwave / boundary layer interaction significantly effect the surface heat transfer and must be correctly treated. Years of research have resulted in the development of numerous procedures, models and correlations to treat the effects of these features on flow predictions. While a number of different codes exist, the commercial FV code – FLUENT, was available for the aerodynamic analysis in this study.

A numerical solution involves conversion of the governing differential equations into a set of discrete algebraic equations, which are solved numerically by an iterative solution technique. A finite volume code uses the control-volume-based technique to discretize the governing continuity, momentum and energy transport equations using a computational grid. The governing equations are then integrated over each control volume to yield discrete equations, which are linearized and solved by a linear equation solution algorithm. Adding or removing terms determined by the specifics of the problem results in modified form of the general transport equations, which then define the problem. The modifications result from the various numerical models that have been developed to treat the different features, such as turbulence, that may be present in the flow.

3.1.1. Governing Equations for Fluid Flow

Describing fluid flow, which in its most general form is complex and highly unsteady, is no trivial task. The Navier-Stokes equations, which derived from the principles of conservation of mass, momentum and energy, are used to describe fluid motion. The resulting equations, given below, are termed the continuity (Eq 3-1a), momentum (Eq 3-1b), and energy (Eq 3-1c) equations. These are given in their most general form and are modified by the addition and / or subtraction of terms determined by the inclusion of mathematical models to describe specific, and often 'irregular' behaviour of the flow, such as turbulence. This results in a set of transport equations that specifically define the flow for a given problem or class of problem.

Continuity Equation:

$$\frac{\partial \rho}{\partial t} + \nabla \cdot (\rho \vec{V}) = S_m \qquad \text{Eq 3-1a}$$

Momentum Equation:

$$\frac{\partial}{\partial t}(\rho \vec{V}) + \nabla \cdot (\rho \vec{V}\vec{V}) = -\nabla p + \nabla \cdot (\bar{\bar{\tau}}) + \rho \vec{g} + \vec{F} \qquad \text{Eq 3-1b}$$

Energy Equation:

$$\frac{\partial}{\partial t}(\rho E_E) + \nabla \cdot (\vec{V}(\rho E_E + p)) = \nabla \cdot [k \nabla T - \sum_j h_j \vec{J}_j + (\bar{\bar{\tau}} \cdot \vec{V})] + S_h \qquad \text{Eq 3-1c}$$

In the general for of the governing equation given above, $\vec{V}$ is the vector of velocity components, ρ is the fluid density, p is the fluid static pressure, $\bar{\bar{\tau}}$ is the stress tensor described by Eq 3-2a with μ being the molecular viscosity and I the unit tensor, $\rho \vec{g}$ and $\vec{F}$ represent the gravitational and body forces respectively. For the energy equation, E_E is given by Eq 3-2b with h being the enthalpy and k representing the thermal conductivity. The summation term accounts for the diffusion of species j. The source terms S_m and S_h are the mass addition and volumetric or species heat source respectively.

$$\bar{\bar{\tau}} = \mu[(\nabla \vec{V} + \nabla \vec{V}^T) - \frac{2}{3} \nabla \cdot \vec{V} I] \qquad \text{Eq 3-2a}$$

$$E_E = h - \frac{p}{\rho} + \frac{V^2}{2} \qquad \text{Eq 3-2b}$$

For the purpose of illustration, the modified Navier-Stokes equation for constant ρ and μ in Cartesian coordinates for the x-coordinate direction is shown below:

$$\rho\left(\frac{\partial V_x}{\partial t}+v_x\frac{\partial V_x}{\partial x}+v_y\frac{\partial V_x}{\partial y}+v_z\frac{\partial V_x}{\partial z}\right)=-\frac{\partial p}{\partial x}+\ldots$$
$$\ldots\rho g_x+\mu\left(\frac{\partial^2 V_x}{\partial x^2}+\frac{\partial^2 V_x}{\partial y^2}+\frac{\partial^2 V_x}{\partial z^2}\right) \qquad \text{Eq 3-3}$$

The physical nature of turbulent fluid motion is highly, but not complete, irregular. If it were entirely irregular, then mathematical treatment of it would be impossible. A more precise definition of turbulent fluid motion that allows mathematical treatment, and therefore closure of the transport equations for turbulent flow, given by Hinze (1959) is that turbulent fluid motion is an irregular condition of flow that shows random variation with time and space for which distinct average values can be attained. This definition allows the variables in the transport equations to be written in terms of mean and fluctuation components, shown in Eq 3-4 for the velocity in the x-component direction. This approached results in the Reynold's Averaged form of the transport equations, which are referred to as Reynold's Averaged Navier-Stokes (RANS) equations.

$$V_x=\overline{V}_x+V_x' \qquad \text{Eq 3-4}$$

3.1.2. Numerical Solution of the Governing Equations

FLUENT employs the RANS equations for turbulent flow solutions. Two algorithms for the solution of the RANS equations are available in FLUENT – SEGREGATED and COUPLED, so named because of the manner in which each solves the set of governing equations. The SEGREGATED approach solves the equation set sequentially and the COUPLED approach solves it simultaneously. Both solution algorithms use finite volume discretization but utilize different linearization techniques in the solution process. The two linearization techniques available in FLUENT are Implicit and Explicit linearization. The numerical solution of the

linearized discrete algebraic equation set, which yields the updated flow variables, is carried out by a linear equation solver.

3.1.2.1. Discretization

FLUENT uses a control volume based technique to convert the governing differential equations to algebraic equations, which can be solved numerically. Using a computational grid, the flow domain is divided into discrete control volumes. The governing equations are integrated over each control volume (shown by Eq 3-5 for the transport of an arbitrary scalar quantity ϕ) to yield discrete equations that conserve each flow variable in each control volume. The discrete form of the transport of the arbitrary variable ϕ is given by Eq 3-6.

$$\oint \rho\phi\vec{V}\cdot d\vec{A} = \oint \Gamma_\phi \nabla_\phi \cdot d\vec{A} + \int_V S_\phi dV \qquad \text{Eq 3-5}$$

$$\sum_f^{N_{faces}} \rho_f \vec{V}_f \phi_f \cdot \vec{A}_f = \sum_f^{N_{faces}} \Gamma_\phi (\nabla\phi)_n \cdot \vec{A}_f + S_\phi V \qquad \text{Eq 3-6}$$

In Eqs 3-5 and 6, $\vec{A}$ is the surface area vector, Γ_ϕ is the diffusion coefficient of ϕ, S_ϕ is the source of ϕ per unit volume where V is the cell volume, N_{faces} is the number of faces enclosing the cell, ϕ_f is the value of ϕ convected through face f, and $\rho_f \vec{V}_f \cdot \vec{A}_f$ is the mass flux through the face where $\vec{A}_f$ is the area of face f. The discrete value is stored at the cell centre but face values (at the cell faces) are required for the convection terms in the discrete equations. The face values are interpolated from the cell centre values by an upwinding scheme, implying that the upstream cell centre value is used to derive the face value.

Four upwinding schemes, viz. First-Order, Second-Order, Power Law and QUICK are available in FLUENT. A discussion of the upwinding schemes was deemed to be excessively lengthy and also unnecessary. The choice of upwinding scheme used for a simulation in FLUENT is limited by the choice of solver and linearization technique. When the algebraic equations are linearized implicitly, the unknown value, for a given variable, in each cell is calculated using a relation that includes both existing and unknown values from neighbouring cells. Each unknown will therefore appear in more than one equation in the set and thus can only be solved

simultaneously. For explicit linearization, the unknown value, for a given variable, in each cell is calculated from a relation than uses only known values. Each unknown appears in one equation in the set and each equation can be solved sequentially to give the unknown values.

3.1.2.2. Segregated Solution Algorithm

The SEGREGATED solver allows only implicit linearization of the discrete governing equations, and solves the system using the Point Implicit (Gauss-Siedel) linear equation solver together with the Algebraic multigrid Method (AMG). The steps involved in the SEGREGATED algorithm are outlined as follows. The velocity field is updated by solving the momentum equations for each velocity component using existing pressure and face mass flux values.

A pressure correction is then applied to obtain corrections for the velocity, pressure and mass fluxes, such that the continuity equation is satisfied. Equations for scalars such as turbulence etc. are solved using the current updated values. A check for convergence is made, and if the convergence criteria are satisfied, then the solution process is stopped. If the solution has not converged, the steps are repeated until convergence is reached. Several iterations of the solution may be necessary to achieve a converged solution since the governing equations are non-linear and coupled.

3.1.2.3. Coupled Solution Algorithm

The coupled solution algorithm solves the set of governing momentum, continuity and energy transport equations simultaneously, i.e. coupled together. This is because the unknown variables appear in more than one equation in the set and can therefore not be solved separately. The governing equations for the additional scalars (turbulence etc.) are solved sequentially, separate from the coupled set. The iteration loop for the coupled solver consists of first updating the fluid properties based on either the current solution or the initial values. The governing equations are then solved by the steps mentioned above. A check for convergence is done and the solution is stopped if the criteria are net or the loop repeated, usually several times, until convergence is reached.

The Coupled method allows either implicit or explicit linearization. A Coupled-Implicit solution results in a coupled system of equations for each cell. Point Implicit (Gauss-Siedel) linear

equation solver in conjunction with the AMG method is used to solve the coupled equation set. For the Coupled-Explicit solver, the multistage (Runge-Kutta) solver is used with the option of using Full Approximation Storage (FAS) to accelerate the multistage solver.

3.1.3. Turbulence Models and Near-wall Treatment

FLUENT affords the user the flexibility to choose between four turbulence models and two near-wall treatments for the RANS equations as well as a Large Eddy Simulation (LES) model. This may seem to indicate that FLUENT is a very powerful tool when it comes to modelling turbo machinery flows, but FLUENT is a commercial code and caters for all types of fluid flow and heat transfer problems from simple pipe flow to chemical reactions and combustion modelling. No turbulence model is universal, but most flow scenarios are accommodated by the variety of combinations of different versions of the turbulence models. These turbulence models were incorporated because of their applicability to a wide range of flows but for turbo machinery flows, careful consideration must be given to the expected flow features when choosing a turbulence model.

The turbulence models available in FLUENT are outlined below:

- Spalart-Allmaras model
- k - ε models
    - Standard k - ε model
    - Renormalization-group (RNG) k - ε model
    - Realizable k - ε models
- k - ω models
    - Standard k - ω model
    - Shear-Stress Transport k - ω model
- Reynolds Stress Model (RSM)
- Large Eddy Simulation (LES)

And the following Near-Wall Treatments are available:

- Wall Functions
- Enhanced Wall Treatment

The Spalart-Allmaras model (Spalart and Allmaras 1992) is a one-equation model where the length scale is related to the local shear layer thickness. It is a low-Reynolds-number (LRN) model in its original form and requires that the viscous affected zone be properly resolved. Wall Functions must be used when the near-wall mesh cannot be made fine enough to resolve the viscous affected layer. The Standard k - ε model (Launder and Spalding 1972) is a semi-empirical, two-equation, high Reynolds number model. The two-equation models allow the independent calculation of turbulent viscosity and length scales for the solution of two separate transport equations.

Continued research and development have resulted in a number of variations of the Standard k - ε model. Two of these incorporated in FLUENT are the RNG k - ε model (Yakhot and Orszag 1986) and the Realizable k - ε model (Shih et. al. 1995). The RNG model was derived from Renormalization Group Theory. It contains an additional term in the ε equation and computes the turbulent Prandtl number from an analytical formula. Low-Reynolds-number effects are handled by an analytically derived formula for effective viscosity. The model's performance is however dependant on the treatment of the near-wall region.

The Realizable k - ε model employs a new formulation for turbulent viscosity and a new transport equation for ε. This modified version of the Standard k - ε model satisfies the mathematical constraints on Reynolds stress consistent with the physical nature of turbulent flows. FLUENT uses a Standard k - ω model based on the Wilcox k - ω model (Wilcox 1998) which is modified for low-Reynolds-effects. The SST k - ω model (Menter 1994) incorporates a blending function that switches from the Standard k - ω model in the near-wall region to the k - ε model in the free stream. The RSM solves the Reynolds stress transport equations together with the ε equation resulting in four additional equations for a 2-D problem and seven for a 3-D problem. For the LES model, large eddies are computed in a time dependant simulation using a set of NS equations that are manipulated to remove eddies above a predetermined size.

For turbulent flow simulations with surface heat transfer, correct treatment of the near-wall region is essential. The viscous effect, of the no-slip condition at the wall boundary, on the

velocity field must be accounted for. The open literature shows that two methods of treating the near-wall region - the Wall Function approach and Near-wall models - have met with a fair amount of success. The wall function approach does not solve the viscous sub layer, but instead uses semi-empirical formulae to bridge the viscous affected zone with the fully turbulent region. Near-wall models modify the turbulence models so that the viscous affected region, including the viscous sub layer can be resolved. Based on the review by De Villiers (2001), the recommendations made in the FLUENT 6.0 online help manuals, and from the open literature (Launder and Spalding 1972, Jones and Launder 1973 / 1974, Wilcox 1975, Lam and Bremhorst 1981, Rhie and Chow 1983 and Menter 1994), the turbulence models most suited for turbine blade flow are the Spalart-Allmaras, Realizable k - ε model and SST k - ω model.

3.1.4. Heat Transfer Models

FLUENT includes models for conduction and / or convection heat transfer, buoyancy and natural convection driven flows, as well as radiation models. FLUENT will solve a modified energy equations depending on the heat transfer model specified. For the turbine blade heat transfer problem, one needs to model convection heat transfer at the fluid-solid interface (i.e. the blade surface) and conduction heat transfer within the blade thickness, which FLUENT is fully capable of modelling. Giving the entities in the FLUENT model the relevant Boundary Condition definition imposes the appropriate boundary conditions for the FLUENT model.

3.1.5. Boundary Conditions

The solution of the differential equations governing a problem can only be completed if appropriate boundary conditions for the problem are defined. For flow problems, the boundary conditions usually take the form of a specified inlet mass flow, velocity, inlet and exit pressures etc. The FLUENT interface incorporates a list of boundary condition definitions that can be applied to boundary entities of the model, which allows the user to easily impose the boundary conditions for the problem. Through the inputs associated with a specific boundary condition definition, FLUENT will derive the numerical formulation of the boundary condition and incorporate it into transport equations.

3.2. FIDAP – An Overview

FIDAP is a general purpose FEM code designed for simulating inviscid and viscous flows with heat and mass transfer. More recently, FIDAP 8.5, was equipped with FSI capability, allowing the solution of problems that involve interacting fluid and solid bodies. The numerical solution procedure in FIDAP is similar to that described for FLUENT, and indeed for any numerical solution, the difference being that FIDAP discretizes the governing equations using the finite element formulation. This discussion will focus on the Structural solver and the thermal / solid problem formulation in FIDAP since the FIDAP model was only used for the thermal analysis.

FIDAP employs the Galerkin finite element method of weighted residuals to discretize the governing equations by dividing the computational domain into discrete elements. The governing equations are then interpolated over the each element with an interpolation function to produce the discrete algebraic equations, which are solved iteratively, using a linear equation solver.

3.2.1. Solution Procedure for the Thermal Stress Problem

Structural analysis in the present version of FIDAP can only be done assuming elastic, isotropic materials. Geometric non-linearity is handled by the Updated Lagrangian (UL) formulation, where all static and kinematic variables are referred to the most recent calculated values. The solution strategy, employed in FIDAP, for a thermal / solid problem is based on loose coupling of the equation systems for the thermal problem, the structural problem (CSD), and the dynamic mesh (CMD). The computational structural dynamics (CSD) applies the traction from the thermal solution (the temperature distribution in the solid) and uses the UL formulation to solve the displacements of the structure.

An elastostatic model is used in the computational mesh dynamics (CMD) to solve the mesh displacement. The CMD is only required for problems were the structural displacements are large enough to significantly affect the mesh. The simulations done in FIDAP during the study all involved small deformations negating the use of CMD, for that reason, a discussion thereof will not be given. The governing elastodynamic equations for the CSD are the constitutive stress equations (modified to include thermal effects), which are solved together with the equilibrium conditions for the problem. These equations are discretized by the Galerkin finite element procedure taking the UL formulation into account.

The result is a system of non-linear, discrete matrix equations. The discrete equations are solved using the Segregated algorithm, which must be used for when there is CSD in the problem. As in FLUENT, the Segregated solver in FIDAP solves the system of discrete equations in a sequential manner. The Segregated algorithm in FIDAP decomposes the global system matrix into sub-matrices, each governing the nodal variables for one conservation equation. The sub-matrices are solved in a sequential manner using either Gaussian Elimination or a Conjugate Gradient type linear equation solver.

The governing equations for a thermal / solid comprise the Fourier heat conduction equation and the thermal stress and equilibrium equations. FIDAP allows the imposition of thermal boundary conditions (heat fluxes or temperatures) as well as displacement, stress or mixed boundary conditions for the CSD. Plain-strain formulation, meaning that the simulations represent a slice of a 3-D problem in which the third dimension is much larger than the characteristic 2-D dimension, is used for 2-D simulations. This is accounted for by a simplification to the elasticity tensor in the constitutive equation, and thermal effects are taken into account by modifying the strain tensor. This again represents only a brief overview of the code. A more in-depth discussion of important aspects in the FIDAP formulation will be given later.

CHAPTER 4
VALIDATING THE CFD MODEL OF A TURBINE BLADE

4.1. Data for the Mark II NGV

Bohn performed a CFD analysis for the flow and heat transfer around a Mark II NGV, compared the results with the experimental data of Hylton et. al (1983), and also performed a FEM analysis for the internal blade temperature and thermal stresses. The geometry configuration and boundary conditions for the CFD simulations are given in Figure 4-1. The geometric coordinates for the blade were given in Nealy et. al. (1984), who also presented experimental and predicted pressure and heat transfer results for the Mark II NGV.

Bohn's CFD analysis solved the compressible RANS equations discretized using the implicit FV formulation, with the Baldwin-Lomax, algebraic, eddy-viscosity, turbulence model providing closure for the RANS equations. The Fourier heat conduction equation was solved in the solid body with the fluid and solid regions coupled via a common wall temperature. The resulting linear system of equations was solved by Gauss-Siedel point iteration. The flow passage was meshed with 11920 grid points, and the blade with 3212 grid points. The boundary layer mesh at the blade surface contained 10 cells with the height of the first cell centre being at a y^+ (Eq E-9, Appendix E) value of 0.3.

The comparisons were given as distributions of pressure, temperature and heat transfer coefficient as a function of x/L (dimensionless axial chord) for the pressure and suction surfaces of the blade. These were compared with the results of the current study. The results given in Nealy et. al. (1984) compared experimental data with predictions done using a time-dependant, transonic, inviscid, cascade code (Delaney 1982), together with a modified version of the boundary layer code STAN 5 (Crawford and Kays 1976) which features zero-order turbulence modelling. Nealy's comparison was done for three exit Mach numbers, one of which, exit Mach number = 0.98, was the case used in Bohn's study. For completeness, the aerodynamic results of the present study were also compared with Nealy's results for exit Mach numbers of 0.75 and 1.04.

Bohn's FEM simulation was done using MARC/Mentat - a commercially available FEM code. The FEM computational grid for the blade employed higher order elements and contained 2032 elements with 6743 nodes. The simulation was done as 2-D, plane strain and took into account

temperature dependence of thermal conductivity, thermal expansion coefficient and Young's modulus. The blade material was ASTM 310 stainless steel, which was used by the experimenters because of its low thermal conductivity. The temperature distribution on the blade surface, which was solved in the CFD analysis, along with the cooling hole heat transfer coefficients which were determined from the experiments, was used as the boundary condition for the FEM analysis. The FEM solved the blade temperature distribution and the resulting thermal stresses. The results of the FEM simulation were given as contours of blade temperature and equivalent stress (σ_e), as well as σ_e and stress in the Z–coordinate direction (σ_z) along line AB through the blade.

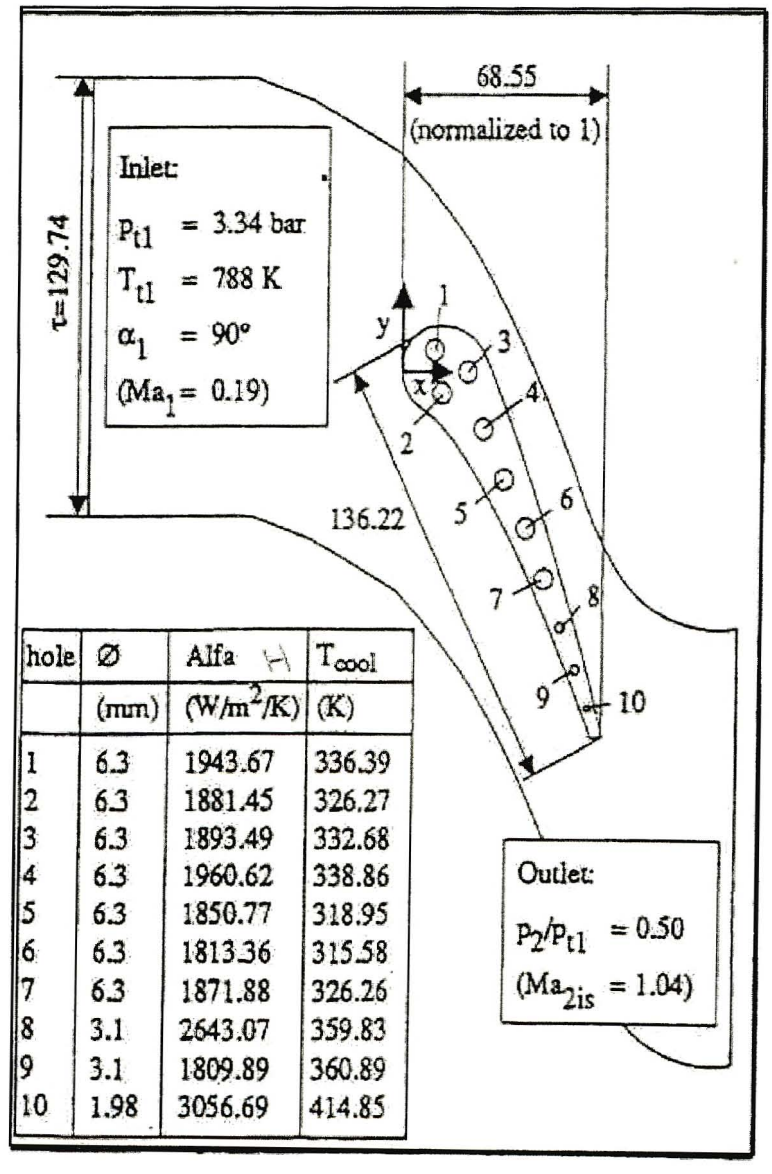

hole	Ø	Alfa	T_{cool}
	(mm)	($W/m^2/K$)	(K)
1	6.3	1943.67	336.39
2	6.3	1881.45	326.27
3	6.3	1893.49	332.68
4	6.3	1960.62	338.86
5	6.3	1850.77	318.95
6	6.3	1813.36	315.58
7	6.3	1871.88	326.26
8	3.1	2643.07	359.83
9	3.1	1809.89	360.89
10	1.98	3056.69	414.85

Figure 4-1: Geometric configuration and boundary conditions for the Mark II NGV reproduced from Bohn et. al. (1995)

4.2. Data for a Cylinder

Prior to the data for the Mark II NGV becoming available, some simple thermal stress simulations were done for a long cylinder. A cylinder was chosen because it represented a simple geometry for which theoretical, analytical and numerical data were readily available. From simple heat transfer, thermal stress and elasticity theory, one can solve the classical Fourier equation and equations of equilibrium (extended to cover thermal stresses), in cylindrical coordinates, together with appropriate boundary conditions, to yield the internal temperature and stress profiles for the cylinder.

Ali and Alam (1997) presented a steady state thermal stress result for a long cylinder with a prescribed internal temperature profile. The study validated the authors' semi-empirical solution with a numerical solution done using a commercial FEM code - ABAQUS. The results were presented for the mid-span of the cylinder making them representative of a 2-D, plain-strain solution. The FEM analysis used a computational grid consisting of 750 elements, 25 elements in the radial direction and 30 along the length. The focus of the study was a solution with temperature dependant material properties, but a solution with constant material properties was also given. These were used for the steady state validation exercise.

The non-dimensionalised temperature profile (Eq E-2a, Appendix E) is for the cases of a cylinder initially at temperature T_i, placed in a hot environment such that its surface temperature changes to T_s. This temperature profile is the solution to the steady 1-D Fourier equation (Eq E-1a) with boundary conditions T_i at $r = 0$ and T_s at $r = R$. The mid-span stress profile from the numerical solution in Ali and Alam is what would have resulted if the thermal stress integral (Eqs E-4a to c) were calculated with the profile in Equation E-2a substituted for T. The thermal stresses were non-dimensionalised by dividing by $E\alpha\Delta T$. The problem solved by Ali and Alam is similar in nature, although much simpler, to that found in a turbine blade.

It was interesting to note that the temperature profile given by Equation E-2a was similar to the solution for a cylinder with a constant heat flux at the surface given by Carslaw and Jaeger (1956). The Carslaw and Jaeger solution was an unsteady problem, but at large times, was almost identical to Equation E-2a. With the foresight that the test cases, which the model would be used to simulate, were unsteady, it was decided to use the Carslaw and Jaeger solution to analytically generate thermal stress data for a cylinder with an unsteady temperature profile. This data would be used to validate the numerical solution for the same problem.

Carslaw and Jaeger solved the unsteady Fourier equation (Eq E-1b) for a cylinder with zero initial temperature and a constant heat flux at the surface. Equation E-2b gives the resulting unsteady temperature profile. The profile described by Equation E-2b is easily computed analytically for a particular set of conditions, but solving the stress integral (Equations E-4a to c) with an unsteady temperature profile is a complex, but not impossible, task. The dead end lies in trying to analytically compute the unsteady thermal stress profile, which could not be accurately done because a significantly large number of roots were necessary for the Bessel function series to diminish. Most mathematical handbooks (e.g. Abramowitz and Stegun 1972) give the first 20 roots of the commonly encountered transcendental equations. For an unsteady thermal stress profile, 20 roots are not sufficient.

To get around this problem, it was decided to solve the unsteady problem in two FEM codes and compare the results. To do this successfully, one must have prior knowledge of the expected results. This is to guard against the scenario where both codes give the same incorrect result. It is already known what the steady stress profile, i.e. after a large time, will be, and one can easily determine, from the relevant literature (Goodier and Timoshenko 1970, Burgreen 1971 and Hetnarski 1986), what the unsteady stress profiles will look like. The FEM codes used were MSC NASTRAN and FIDAP. The steady state case reported in Ali and Alam (1997) was used to determine any discrepancies between the two numerical FEM solutions. The two codes were than used to solve the unsteady problem.

4.3. Aerodynamic Analysis

The first step in validating the CFD model is to validate FLUENT for predicting the flow field and surface heat transfer. The open literature has emphasised that correct prediction of the blade surface pressure is a necessary first step in obtaining good heat transfer prediction. Correct surface pressure prediction would be the result of the flow field being accurately resolved. It follows then that the process of setting up and refining a FLUENT model must first achieve surface pressure distributions that compare well with the data. This involves choosing a suitable turbulence model, and refining the near-wall mesh based on the choice of near-wall model.

The desired surface pressure distribution will be achieved when the mesh is sufficient refined to provide mesh independent resolution of the flow field and the turbulence model provides adequate closure to the RANS equations. At this point, the heat transfer model can be included in the aerodynamic analysis. The near-wall mesh will need considerable additional refinement to attain even fair surface heat transfer prediction. Also, close attention must be paid to the

turbulence model and near-wall model, as the models that proved adequate to realise good surface pressures may not do so for heat transfer. It is highly unlikely that mesh independent surface heat transfer results will be achieved, since heat transfer is highly sensitive to the wall y^+ values, which depend on the height of the wall adjacent cell and predicted flow values (Eq E-9). The FLUENT model, which yields surface pressure and heat transfer distributions comparable with the data, will be used to perform the aerodynamic analysis for the test cases.

4.3.1. Defining the Problem in FLUENT

The geometry and mesh for the FLUENT analysis was created using a program called GAMBIT. The coordinates for the blade, given by Nealy et. al. (1987), were not for a blade oriented at the vane setting angle used in the analysis by Bohn et. al. (1995), but for a blade in a standard XY axis system with the leading edge and trailing edge / pressure surface corner, on the X-axis. With the vane setting angle (63.69^0) given, Nealy's coordinates were transformed such that the resulting coordinates generated a blade oriented correctly with respect to the axis system as shown in Figure 4-1. The flow field around the blade was set up to exactly replicate Bohn's model (Figure 4-1). The FLUENT geometry is shown in Figure 4-2.

The blade surface and cooling holes were defined as WALL boundaries. The purpose of a WALL boundary is to impose a no-slip condition for the flow at that boundary. The surface heat transfer model is also enforced through the choice of WALL boundary heat transfer models. The top and bottom edges were defined as PERIODIC boundaries. A solution for the blade surface temperature necessitates that the Fourier heat conduction equation be solved. For this, the blade must be included in the model thereby making it necessary to not only model one blade-to-blade flow passage, but two such passages so that one blade is included in the model.

To reduce the computational domain, a section of the flow field containing one blade is modelled with the section boundaries being defined as PERIODIC. The justification is that the flow above and below the top and bottom edges respectively, will be the same thereby rendering them periodic. This type of boundary definition, ensures that the flow entering / leaving the top boundary, matches the flow leaving / entering the bottom boundary respectively. The fluid inlet and outlet was defined as a PRESSURE INLET and PRESSURE OUTLET respectively. These are the mandatory flow inlet and outlet definitions for compressible flow with the required model inputs being total and static pressure, and free stream turbulence level for the inlet and static pressure and free stream turbulence level for the outlet.

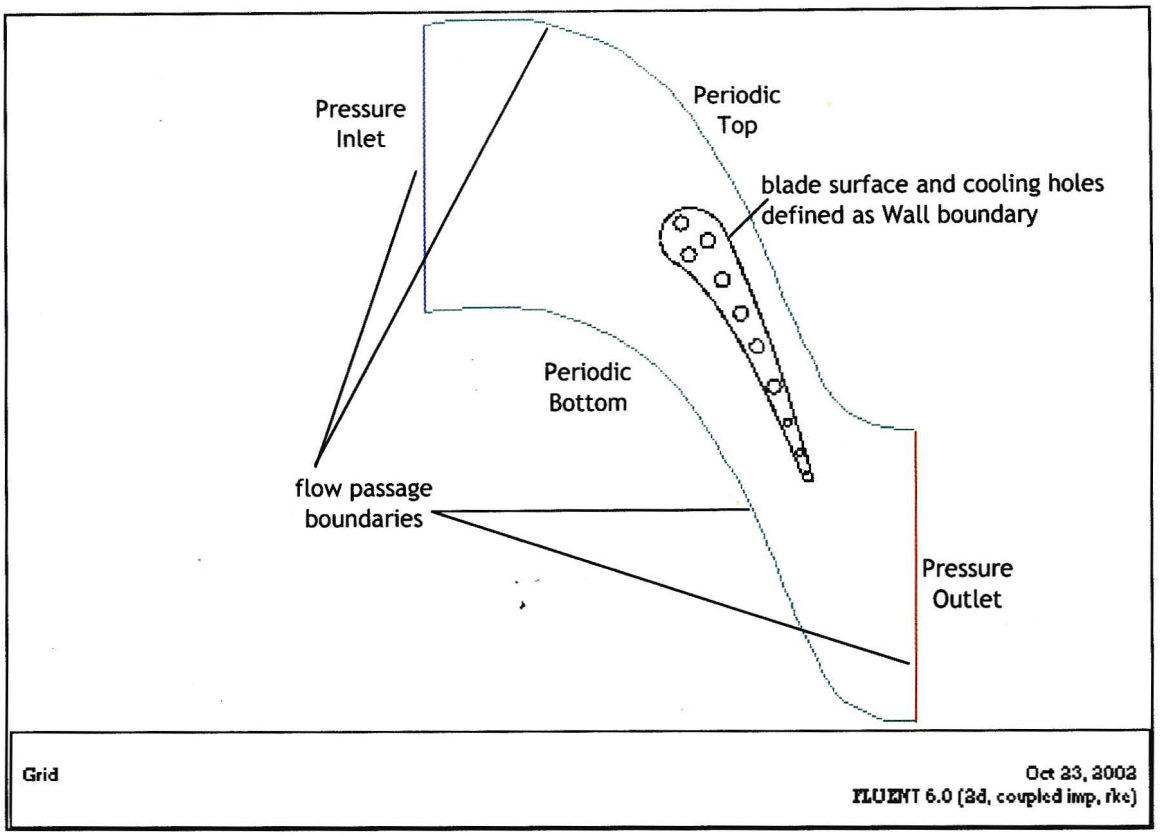

Figure 4-2: FLUENT geometry for the aerodynamic analysis showing the boundary definitions

The solver, viscous model and energy equation are enabled via the DEFINE > MODELS menu. For compressible flow, the energy equation must be enabled since the fluid density will be defined as some function of pressure and / or temperature, the former being the case for air where Equation E-12 calculates the density. Defining the density as IDEAL GAS in the DEFINE > MATERIALS menu, enables Equation E-12, and this results in the fully compressible form of the Navier-Stokes equations being solved. Closure of the compressible RANS equations is achieved with a turbulence model enabled in the DEFINE > MODELS > VISCOUS panel. The Spalart-Allmaras, k - ε model and the SST k - ω model were tested.

The appropriate solver for a compressible flow solution is the coupled implicit solver, which uses 2nd order upwinding for the governing equations and 1st order upwinding for the additional scalar equations (i.e. turbulence etc.). The discrete equations are solved by Gauss-Siedel point iteration together with the AMG solver. The default CFL (Courant) number for the coupled implicit solver is 5, which may be increased to speed up convergence or decreased for highly non-linear changes such as at the start of a solution.

The boundary condition at the already defined model boundaries are set via the DEFINE > BOUNDARY CONDITIONS panel. The boundary conditions given by Bohn (see Figure 4-1)

were imposed on the model. The FLUENTS inputs for the PRESSURE INLET are total and static pressure, total temperature and free stream turbulence intensity, and PRESSURE OUTLET are static pressure, total temperature and free stream turbulence intensity.

These were all the necessary boundary conditions for the aerodynamic analysis without heat transfer i.e. to obtain only the surface pressure distributions. The heat transfer model used at the fluid-solid interface (the blade surface) was a COUPLED thermal condition, which is used for 2-sided wall heat transfer, i.e. convection from the fluid to solid and conduction within the blade. For the cooling holes, a CONVECTIVE heat transfer model was enabled, using the heat transfer coefficients and free stream temperatures given in Figure 4-1. These were determined from the experiments by Hylton et. al. (1983).

The fluid - air, was modelled as an ideal gas because of compressibility, and FLUENT database values of viscosity (1.7894 E – 05 kg/ms) and thermal properties (Cp = 1006.43 J/kgK and k = 0.0242 W/mK) were used. For the blade, the database values for steel (density = 8030 kg/m^3, Cp = 502.48 J/kgK and k = 16.27 W/mK) were used, even though Bohn and the experimenters used ASTM 310 stainless steel. The difference between the database values and those of ASTM 310 (looked up in a Metals Handbook – ASM International) were small.

4.3.2. CFD Computational Grid Development

The curvature of the geometry caused excessive skewness when quadrilateral cells were used for the computational grid. Reducing the amount of skewness encountered with quadrilateral cells involve intense manipulation of the geometry in GAMBIT. The face making up the flow field must be split into a number of carefully adjusted four sided regions. This can be avoided by generating an unstructured grid using triangular cells, as FLUENT (from FLUENT 5.5 onwards) is designed to used unstructured grids.

A boundary layer mesh was used on the blade surface at the fluid-solid interface since this is a necessity for problems with heat transfer. This was also used for the simulations without heat transfer thereby reducing the effort to regenerate a heat transfer capable grid for the simulations that require it. The purpose of the boundary layer mesh is to give control over the wall y^+ values, which is a critical issue when it comes to the near-wall treatment. The chosen near-wall treatment - enhanced wall treatment - combines the two-layer model with enhanced wall functions, and requires a near-wall mesh fine enough to fully resolve of the viscous affected region.

The two-layer model uses the k - ε model for the fully turbulent region and the Wolfstein (1969) one-equation model in the viscous affected zone. The differentiation between fully turbulent and viscous affected zones, is accomplished by the turbulent Reynolds number (Re_y – Eq E-10), which defines fully turbulent as the region for which $Re_y > 200$. The enhanced wall functions use a single-wall-law for the entire near-wall region by blending the linear and logarithmic (laminar and turbulent respectively) laws of the wall using the blending function of Kader (1993). The blended single-wall-law ensures correct asymptotic behaviour for small and large y^+ values, and reasonably predicts the velocity profile for $3 < y^+ < 10$, i.e. in side the buffer region. For enhanced wall treatment, FLUENT suggests a y^+ value of order 1, but not greater than 4 to 5. This keeps the first cell within the viscous affected region. Furthermore, there should be at least 10 cells within the viscous affected region i.e. $Re_y < 200$.

FLUENT includes the capability of refining the wall adjacent grid cells with a y^+ value based, grid adaption feature. The user can specify a maximum (and / or minimum) allowable y^+ value for the adaption process. Cells with a y^+ value outside the maximum allowable are spilt symmetrically into four, reducing the cell height, thereby reducing the y^+ value. It is difficult to predict the reduction in y^+ that will result from an adaption, as the y^+ value is not only dependent on cell height, but also on turbulent velocity and viscosity, all of which are affected by the adaption. The desired y^+ values should be reached in as few adaptions as possible (2 to 3), as too many successive adaptions leads to oscillations in the flow quantities in the wall adjacent cells.

It was extremely difficult to replicate, in FLUENT, the y^+ value that Bohn used because of the combination of flow features, and the method by which FLUENT adapts the grid. In addition, using grid adaption alters the grid node spacing on the blade surface, which defeats the purpose of generating the same grid for the CFD and FEM. Exporting the adapted grid to FIDAP is also not possible as grid adaption results in hanging nodes, a formulation that FEM is not designed to handle. It is for these reasons that y^+ adaption was not used to refine the near-wall grid. Instead, the meshing parameters (a, GR and Rows) for the boundary layer mesh were tweaked till the closest comparison between FLUENT's temperature distribution and the data was achieved. The temperature distribution was used as the gauge since it was the variable that linked the CFD and FEM analyses.

The near-wall region requires an extremely fine grid, but is not the case for the bulk flow where the gradients are not as steep as the near-wall region. It follows that the grid would have to be fine near the wall and coarser in the free stream. The linear sizing function in FLUENT enables

the user to generate a grid that gradually increases in coarseness from the wall region to the outer boundaries of the domain. The interval size on the blade surface was 0.0787 cm and 0.7 cm on the outer boundaries.

The computational grid for the CFD analysis is shown below. Figure 4-3a shows the grid used for the simulations without heat transfer, which contained 10797 cells and a boundary layer mesh with first cell height of 0.001 cm. The solid region (the blade) was not meshed, as this region was not solved at this point. For the heat transfer simulations the blade was also meshed resulting in 11544 cells for the fluid and 5025 for the solid (Figure 4-3b). The boundary layer mesh (Figures 4-3c and d), which resulted in the closest comparison with the data, contained a first cell height, a = 0.00001 cm, a growth rate, GR = 1.72 and 16 rows of cells.

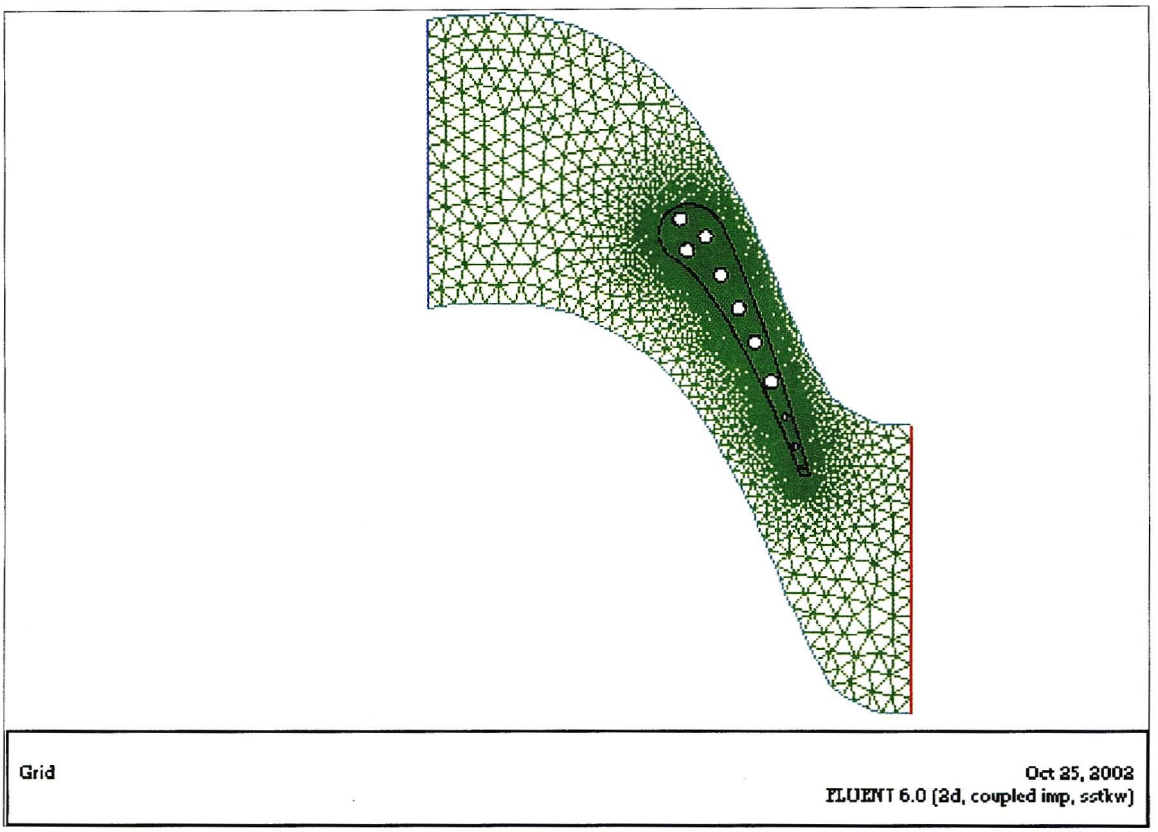

Figure 4-3a: Computational grid for aerodynamic analysis without heat transfer

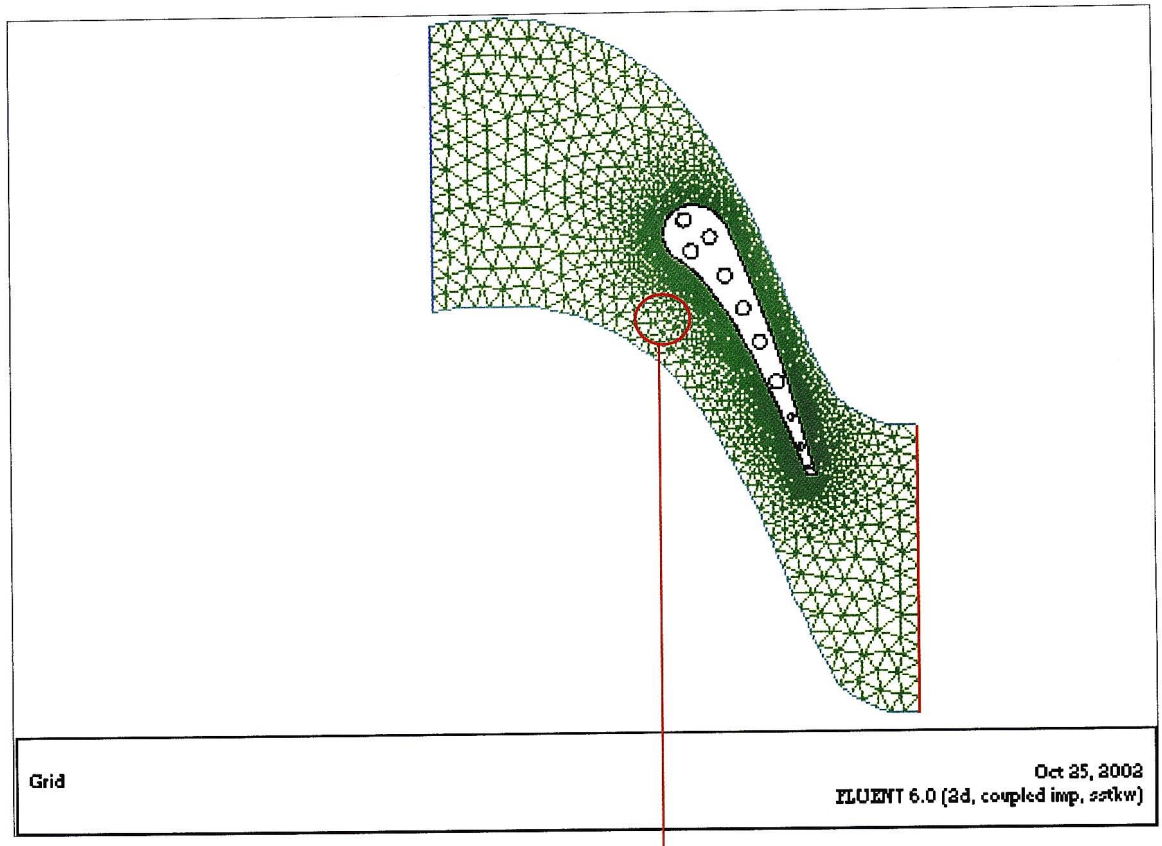

Figure 4-3b: Computational grid for the aerodynamic analysis with heat transfer

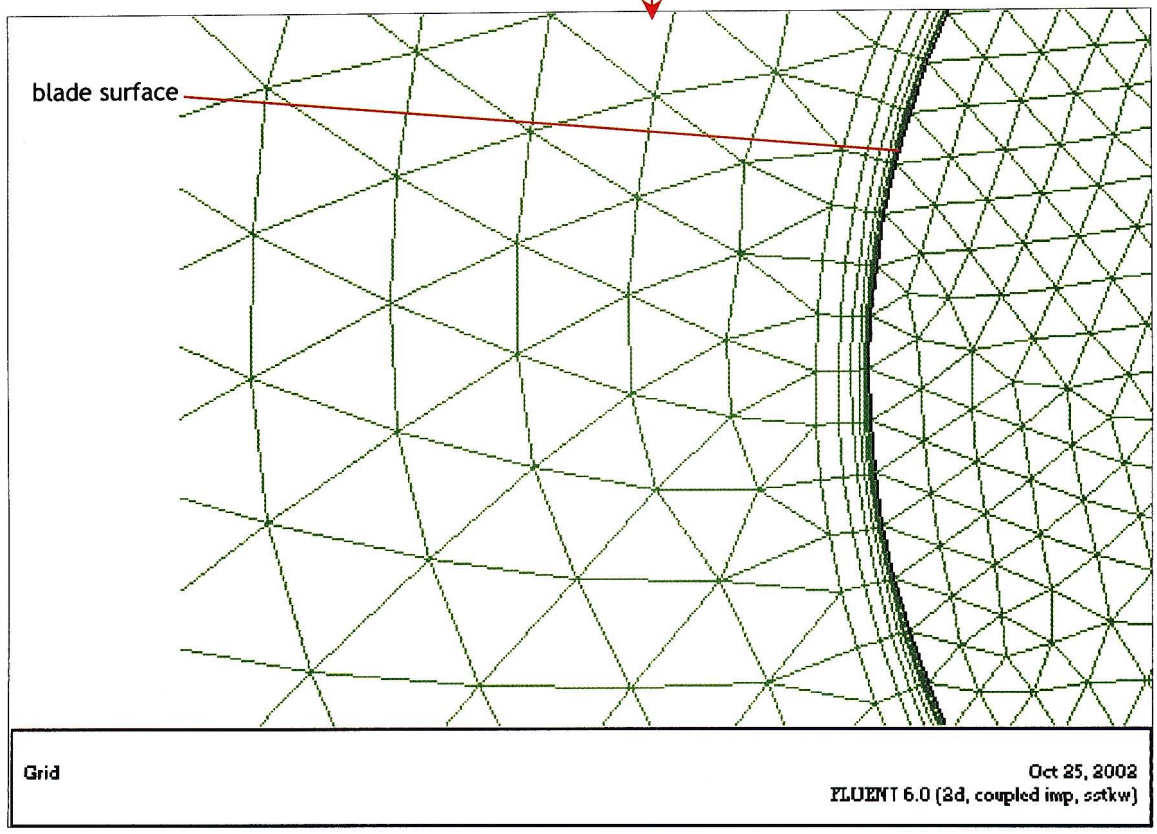

Figure 4-3c: Close-up of near-wall mesh (boundary layer mesh) and mesh in the solid region shown at the leading edge

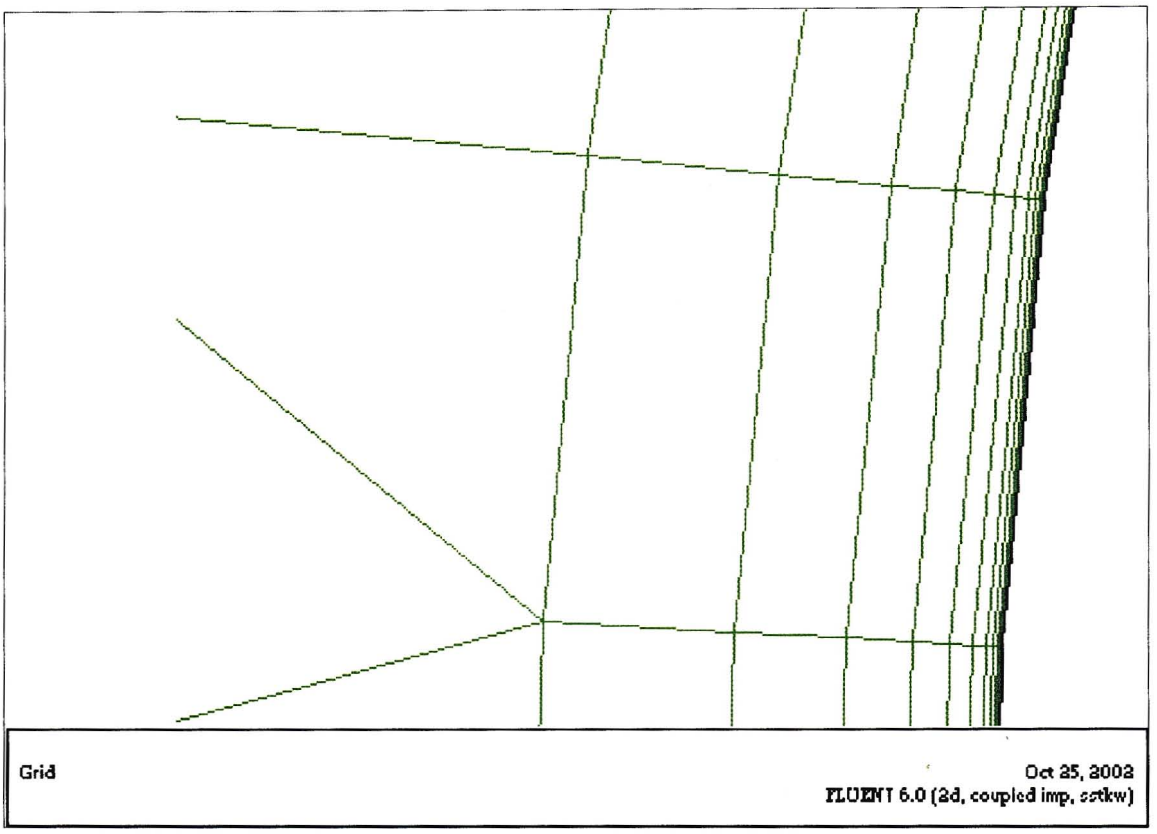

Figure 4-3d: Extreme close-up of boundary layer mesh shown for the leading edge region

4.3.3. Validation of FLUENT

The first step in the validation of FLUENT is to ensure that the flow field is properly resolved. The focus can only shift to the viscous, near-wall region once the inviscid bulk flow has been correctly predicted. The two factors that influence the inviscid flow prediction for turbulent flow are the computational grid and the turbulence model. For the case being modelled, the bulk flow is fast and turbulent in nature, implying that the Reynold's number will be high. For the given aerodynamic boundary conditions the Reynold's number, based on exit velocity and axial chord length, is 2 E 06. This warrants the use of a HRN turbulence model for the main flow. The near-wall region is a low-Reynold's number region because of the low flow velocities, therefore requiring a LRN turbulence model.

Of the three possible turbulence models pertinent to the problem, the SST k - ω model, which was supposed to be designed for such flows, performed the worst. It gave the poorest surface pressure prediction of the three. The reason for the SST k - ω model performing poorly is believed to be because its formulation is designed for LRN flow in the near-wall region. Menter

(1994) recommends that the SST k - ω model be the model of choice for airfoil application, but showed only its superiority over other models in predicting pressure induced separation and the resulting viscous-inviscid interaction. The study gives only the predicted velocity profiles and makes no comparison for pressure and heat transfer prediction.

The open literature has not made known a particular value of Re that renders a turbine blade flow as being LRN, and most researchers rely on past experience. The problem for the Mark II NGV is considered to be a HRN problem with the Re = 2 E 06 - based on exit velocity and chord length. In addition, the velocity profile on the blade surface (Figure E-2d to g, Appendix E) is turbulent in nature over most of the blade, making the viscous affected region (i.e. the LRN zone) thin. It is believed that the combination of very fast moving flow and thin LRN zone are responsible for the poor performance of the SST k - ω model. The SST k - ω model was thus discarded and the Spalart-Allmaras and Realizable k - ε models were further investigated

The first set of simulations were done without heat transfer, i.e. to solve the flow field only. Both turbulence models were used, and the case presented by Bohn was simulated. The boundary layer mesh for the simulation had a = 0.001, GR = 1.2 and Rows = 20. The computational grid, almost identical to the one shown in Figure 4-3a except for the boundary layer mesh, contained 11544 cells. The solutions converged in approximately 1200 iterations taking approximately 21 minutes to do so. The predicted surface pressure distribution is shown in Figure 4-4.

Both turbulence models show excellent agreement with the data implying that either provides adequate closure of the RANS equations. On the pressure surface ($-1 < x/L < 0$) the predictions follow the data almost identically. The flow on this surface begins to slowly increase in velocity from the stagnation point causing the gentle drop in static pressure up to 70 % axial chord. Thereafter, the flow rapidly accelerates through the reducing blade passage throat area causing the steep drop in pressure over the last 30 % axial chord of the blade pressure surface and the first 40 % axial chord of the suction surface. This is clearly shown in Figure E-2b where the velocity vectors go from blue (low velocity) to light green and rapidly to red (high velocity) through the blade passage throat.

The suction surface pressure distribution also compares tremendously well with the data. The prediction follow the drop in pressure down to the minimum which corresponds to the maximum velocity of M = 1.6 at 44 % axial chord. Between 16.7 and 18.9 % axial chord, the pressure ceases to drop but continues thereafter. This small region of no change in pressure

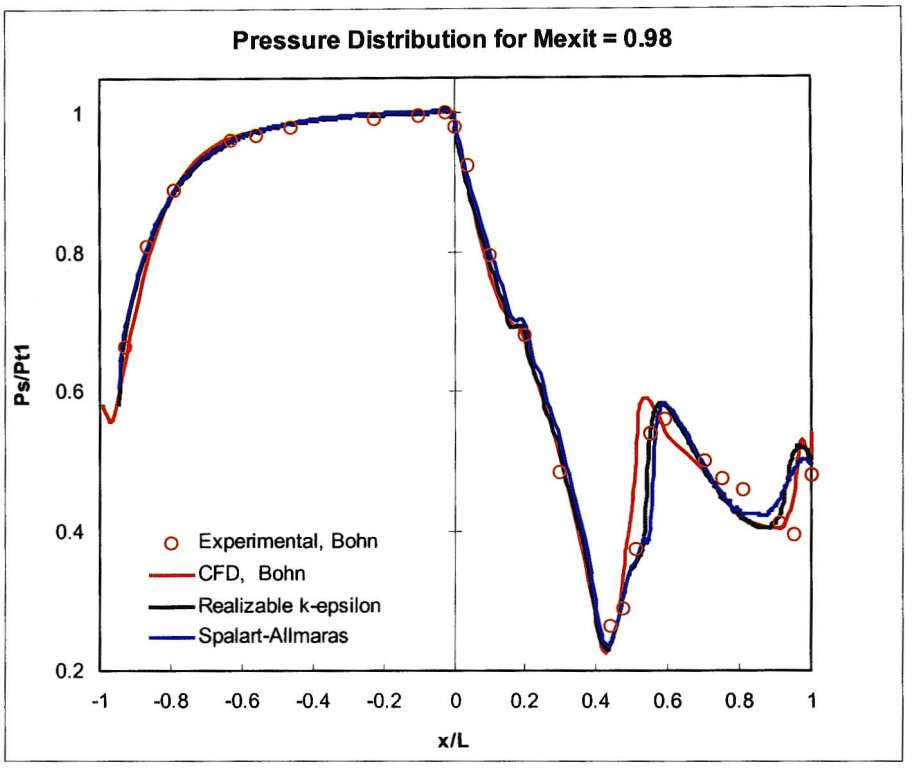

Figure 4-4: Pressure distribution from aerodynamic analysis without heat transfer using Realizable k-ε and Spalart-Allmaras turbulence models for Mexit = 0.98 and a boundary layer mesh with a = 0.001

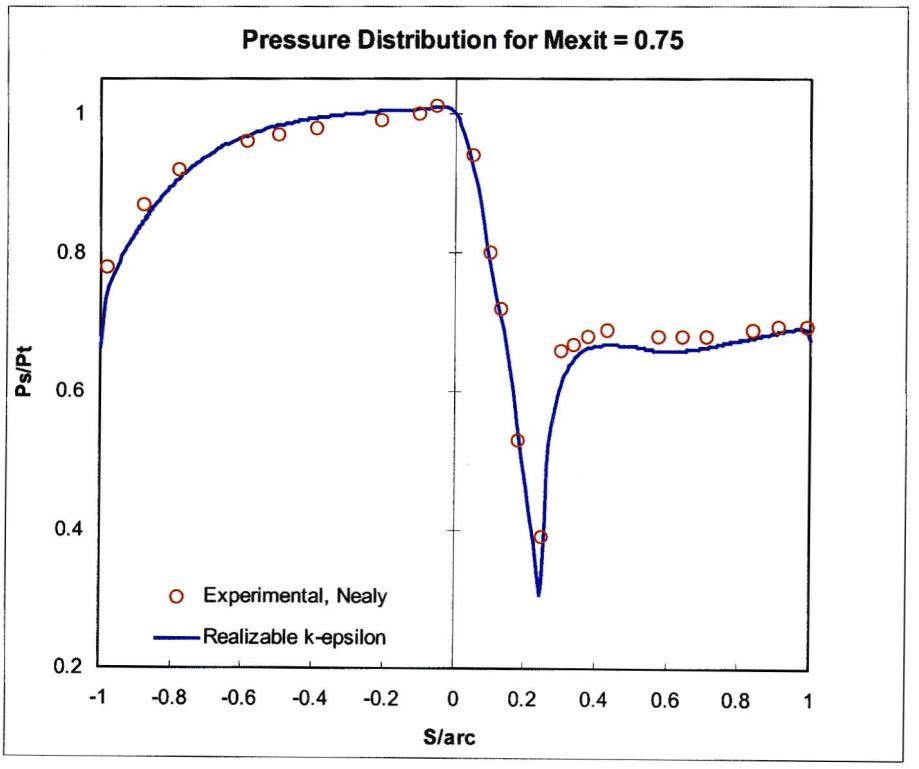

Figure 4-5: Pressure distribution from aerodynamic analysis without heat transfer using Realizable k-ε and Spalart-Allmaras turbulence models for Mexit = 0.75 and a boundary layer mesh with a = 0.001

corresponds to $Re_x \approx 3.1 - 3.4$ E 05 (Eq E-11). For a flat plate, Incropera and DeWitt (1996) gives the critical Reynold's number $Re_{x,c} = 5$ E 05 whereas Schlichting (1955) uses $Re_{x,c} = 3.2$ E 05 given. It is apparent; from the open literature that pressure gradient and free stream turbulence tend to hasten boundary layer transition. It can thus be argued that because of these effects, the critical Reynold's number for the blade is expected to be less than that for a plate. It is believed that this feature in the pressure distribution, between 16.7 and 18.8 % axial chord on the suction surface, could indicate transition of the boundary layer from laminar to turbulent.

FLUENT also predicts the steep increase in pressure from 44 to 58 % axial chord, very close to the data. In fact, the FLUENT predictions (both Spalart-Allmaras and Realizable k - ε) follow the experimental data slightly better than Bohn's CFD prediction. The jump in pressure at this position on the suction surface indicates a normal shockwave. From the velocity vectors (Figure E-2c to f) it is clear that no separation is predicted, yet the flow almost instantaneously decelerates from it maximum, supersonic velocity to a subsonic velocity in a plane normal to the blade surface. This satisfies all the criteria to be a normal shock wave. All the CFD analyses predict the decrease in pressure thereafter, slightly faster than the experimental. The Spalart-Allmaras turbulence model predicts the trailing edge shock sooner than the Realizable k - ε and Bohn's CFD. The differences between the Realizable k - ε predictions and Bohn's are less than 5 % for the trailing edge shock.

All three turbulence models, Spalart-Allmaras, Realizable k - ε (FLUENT) and Baldwin-Lomax (Bohn's CFD), do an excellent job in resolving the flow field. The Realizable k - ε and Baldwin-Lomax turbulence models seem to have better overall performance than the Spalart-Allmaras. This is possibly due the fact that both are two-equation models whereas the Spalart-Allmaras is a one-equation model. Jones and Launder (1973) concluded that only a two-equation type turbulence model would permit universal modelling of the near-wall region, and this is apparent by the overall better performance of the Realizable k - ε and Baldwin-Lomax turbulence models.

Because of its overall superior performance in resolving the flow field, the Realizable k - ε turbulence model was earmarked as the model of choice for use in resolving the flow field for the test cases. For completeness, simulations for the same configuration but with Mexit = 0.75 and 1.04 (Nealy et. al. 1984) was done using the Realizable k - ε. The predicted pressure distributions are compared with Nealy's experimental data in Figures 4-4 and 4-6. Again, the predictions compare very well with the data. For the Mexit = 0.75 case, FLUENT under-

predicts the minimum pressure on the suction side but predicts the pressure recovery due the shock very well. Identical trends discussed for the Mexit = 0.98 case are seen in the Mexit = 1.04 case. The Realizable k - ε turbulence model with enhanced wall treatment has thus far performed consistently well in resolving the flow field for the given configuration.

The heat transfer problem was included in the simulation by specifying COUPLED heat transfer at the fluid-solid interface and CONVECTIVE heat transfer for the cooling holes. It was known a priori that the heat transfer solution was unlikely to be independent of the wall adjacent cell size i.e. the y^+ value (Eq E-9). The boundary layer mesh parameters were varied until the closest comparison with the temperature data was reached. Importance was given on the blade surface temperature distribution since for the test cases; the temperature distribution from the CFD analysis will be used as the boundary condition for the FEM analysis. The resulting boundary layer mesh will be used in the simulation of the test cases. Both the Spalart-Allmaras and Realizable k - ε turbulence model with enhanced wall treatment were investigated for the solution to the problem with heat transfer.

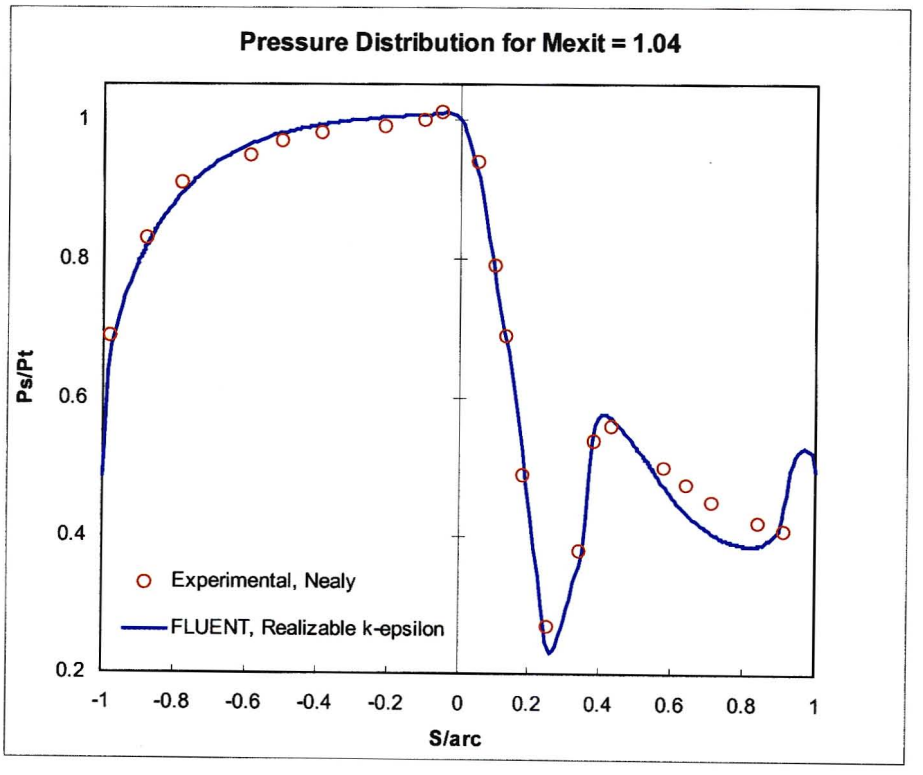

Figure 4-6: Pressure distribution from aerodynamic analysis without heat transfer using Realizable k-ε and Spalart-Allmaras turbulence models for Mexit = 1.04 and a boundary layer mesh with a = 0.001

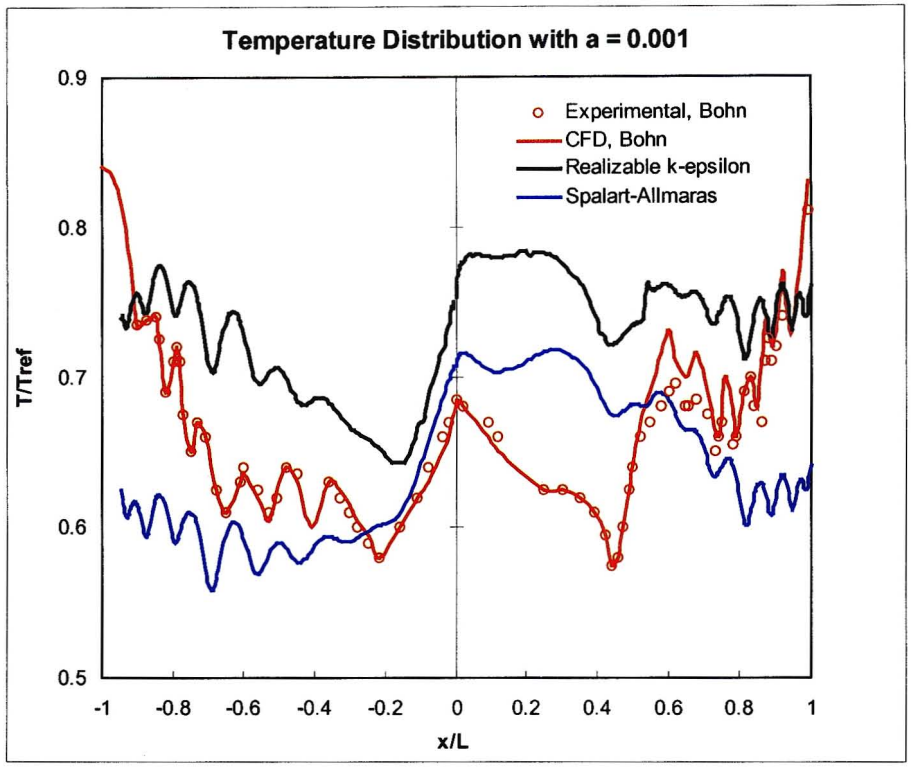

Figure 4-7a: Temperature distribution from aerodynamic analysis with heat transfer using the Realizable k - ε and Spalart-Allmaras turbulence models and a boundary layer mesh with a = 0.001

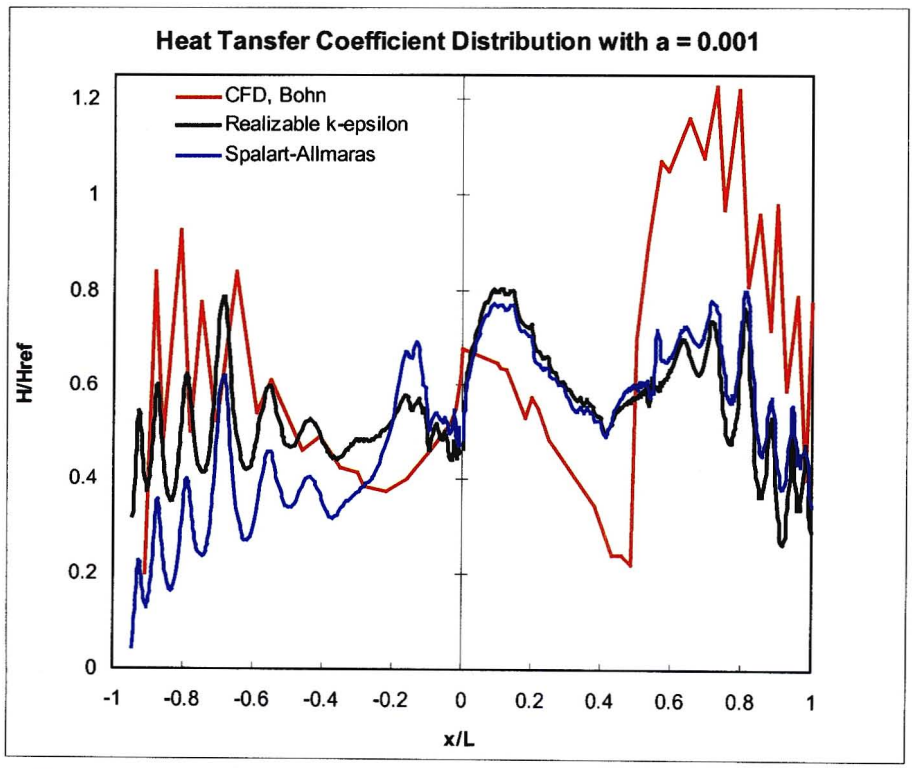

Figure 4-7b: Heat transfer coefficient distribution from aerodynamic analysis with heat transfer using the Realizable k - ε and Spalart-Allmaras turbulence models and a boundary layer mesh with a = 0.001

Both turbulence models were investigated since the differences in the predictions for the flow field only simulations were minor, and the literature has shown that one-equation turbulence models have had some success in modelling turbine blade heat transfer. The first simulation used the same boundary layer mesh and flow field grid used for the simulations without heat transfer but with the solid region meshed as well (Figure 4-3b). The temperature and heat transfer distributions for the boundary layer mesh with a = 0.001 cm, GR = 1.2 and Rows = 16 are shown in Figure 4-7a and b respectively.

Clearly, neither turbulence model is able to give an accurate prediction of the temperature and heat transfer coefficients with the boundary layer mesh used. The Realizable k - ε turbulence model is predicting the trends seen in the data better than the Spalart-Allmaras model. Both over-predict the leading edge temperature - the Realizable k - ε model worse than the Spalart-Allmaras model. Both predict the initial drop in temperature on the pressure on the pressure surface, but Spalart-Allmaras fails to predict the increase in temperature from 20 % axial chord to the trailing edge. On the suction surface, the region from the leading edge to 40 % axial chord is over-predicted with some hint of the drop in temperature prior to the shock being seen. Spalart-Allmaras again under-predicts over the remainder of the suction surface and worst still predicts decreasing temperature.

The heat coefficient transfer distribution (Figure 4-7b) is also poorly predicted. Instead of decreasing during the first 20 % axial chord on the pressure, the predictions increase with a larger increase predicted by the Spalart-Allmaras model. The predictions then decrease from 20 to 40 % axial chord when the data shows increasing trend. From 40 % axial chord to the trailing edge, both show trends consistent with the data, but Spalart-Allmaras again under-predicts much worse than the Realizable k - ε model. On the suction side, the predictions initially increase up to 20 % axial chord, and then follow the slope of the data, while still over-predicting, up to 40 % axial chord. The large spike in heat transfer coefficient due the shock is not predicted. The decreasing trend from 70 % axial chord to the trailing edge is seen, but is under-predicted. The Realizable k - ε model is showing more promise than Spalart-Allmaras but more refinement of the boundary layer mesh is warranted.

The boundary layer mesh initial cell height was reduced to a = 0.0001 cm, and the growth rate increased to 1.44 so that the boundary layer mesh depth with 16 rows remained unchanged. The temperature and heat transfer coefficient distribution for this mesh is shown in Figures 4-8a and b respectively. The Realizable k - ε temperature prediction has dropped below the Spalart-Allmaras, and both are showing fair prediction of the pressure surface temperature distribution. The Realizable k - ε temperature prediction on the suction surface has dropped as well, with

both models performing almost identically. The first 40 % axial chord is over-predicted, the spike due the shock is not predicted, but from 60 % axial chord to the trailing edge is well predicted.

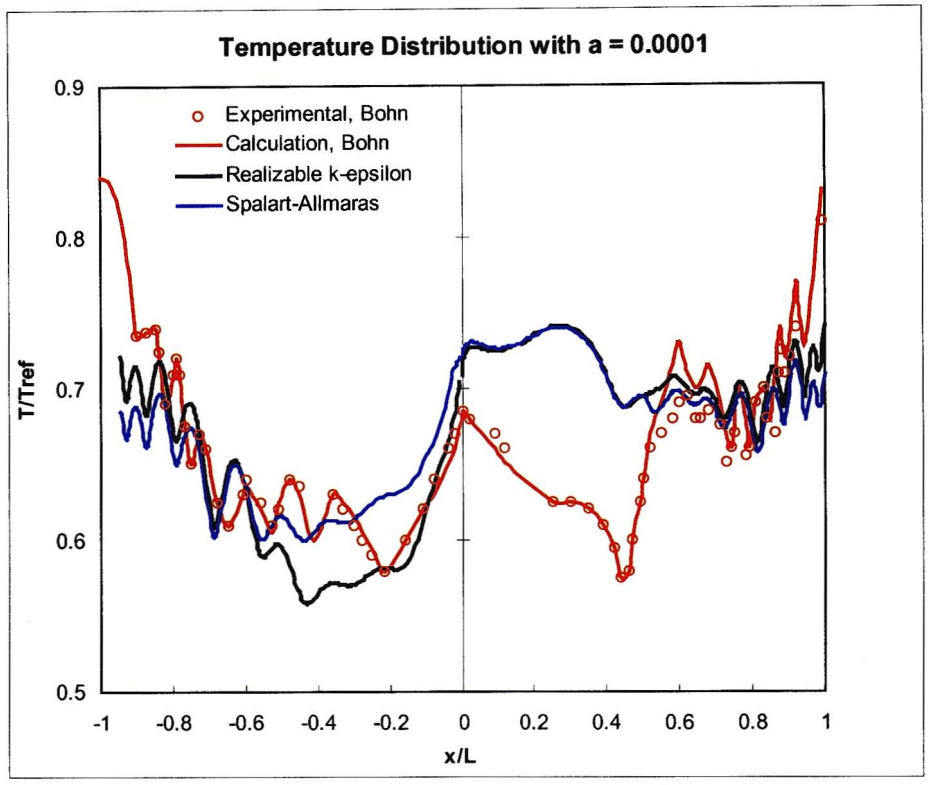

Figure 4-8a: Temperature distribution from aerodynamic analysis with heat transfer using the Realizable k - ε and Spalart-Allmaras turbulence models and a boundary layer mesh with a = 0.0001

The heat transfer coefficient distribution (Figure 4-8b) shows no change on the suction surface but on the pressure surface, the initial rise predicted with the Spalart-Allmaras model is much larger and so is the drop after 18 % axial chord predicted by the Realizable k - ε. With the exception of the first 60 % axial chord on the pressure surface, the prediction from both turbulence models are almost identical. These changes seen in the predictions for the two boundary layer mesh configurations shown highlight the dependence of heat transfer prediction on the boundary layer mesh and y^+ value. The results for the boundary layer mesh parameters of a = 0.00005 cm and GR = 1.43 are shown in Figures 4-9a and b.

Not much change is seen in the temperature prediction, except for a hint of a spike at the shock location. The Realizable k - ε under-prediction on the pressure surface, in the first 60 % axial chord has worsened. The Spalart-Allmaras model is predicting a spike in heat transfer

coefficient at the shock location, which then drops sharply immediately after the shock and the prediction proceeds as it did for the previous two boundary layer mesh configurations.

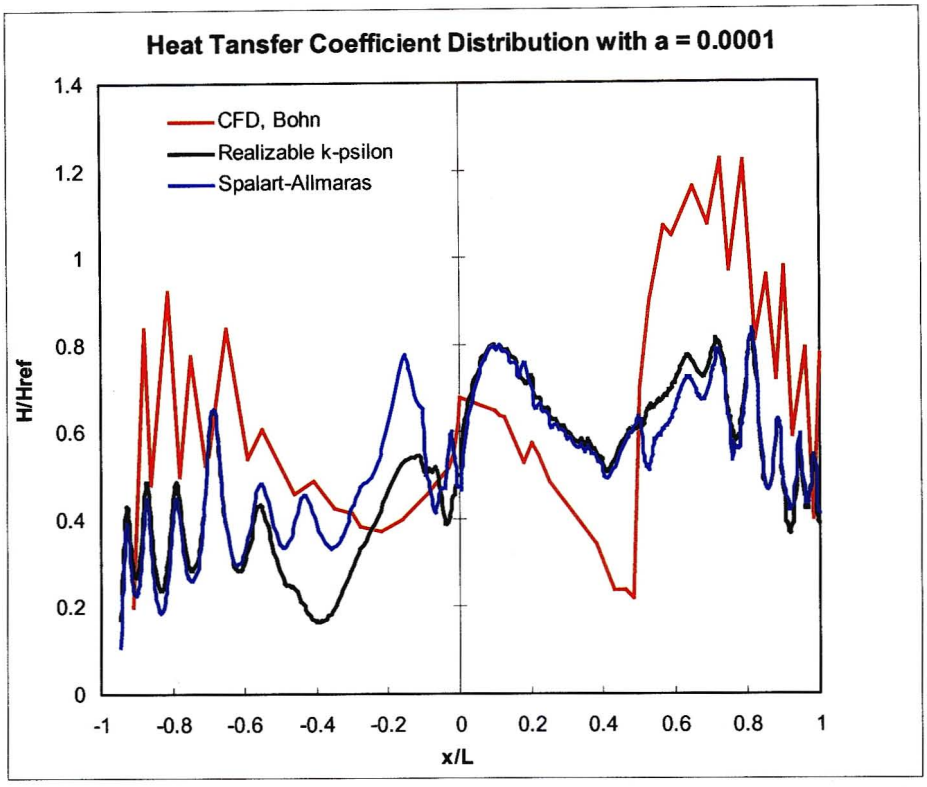

Figure 4-8b: Heat transfer coefficient distribution from aerodynamic analysis with heat transfer using the Realizable k - ε and Spalart-Allmaras turbulence models and a boundary layer mesh with a = 0.0001

From Figures 4-7 to 4-9, it is clear that a deeper understanding of the effect of the boundary layer mesh parameters on heat transfer prediction is necessary. Both turbulence models give qualitatively, the trends seen in the data. At this stage it was decided to make a choice regarding the turbulence model, since the investigations thus far have not been able to show a vast superiority of one over another, and focus on boundary layer mesh refinement. The Realizable k - ε turbulence model with enhanced wall treatment was chosen because of its superior resolution of the flow field and more stable convergence. Using the Realizable k - ε model, the first cell height was varied with all other parameters fixed. The first cell height was fixed to that giving the closest temperature prediction and the growth rate and rows adjusted keeping the boundary layer mesh depth almost fixed.

The result of this investigation was a set of boundary layer mesh parameters, which gave the closest possible comparison of temperature prediction with the data using the Realizable k - ε

turbulence model with enhanced wall treatment. Only the temperature distribution for this part of the analysis will be shown since it was the variable of interest. Figure 4-10 shows the results for varying first cell height (a). The over-prediction on the first 40 % axial chord on the suction surface is not severely affected by varying the first cell height. The pressure side prediction on the other hand is. From Figure 4-10 it is clear that he best overall comparison occurs for a = 0.00001.

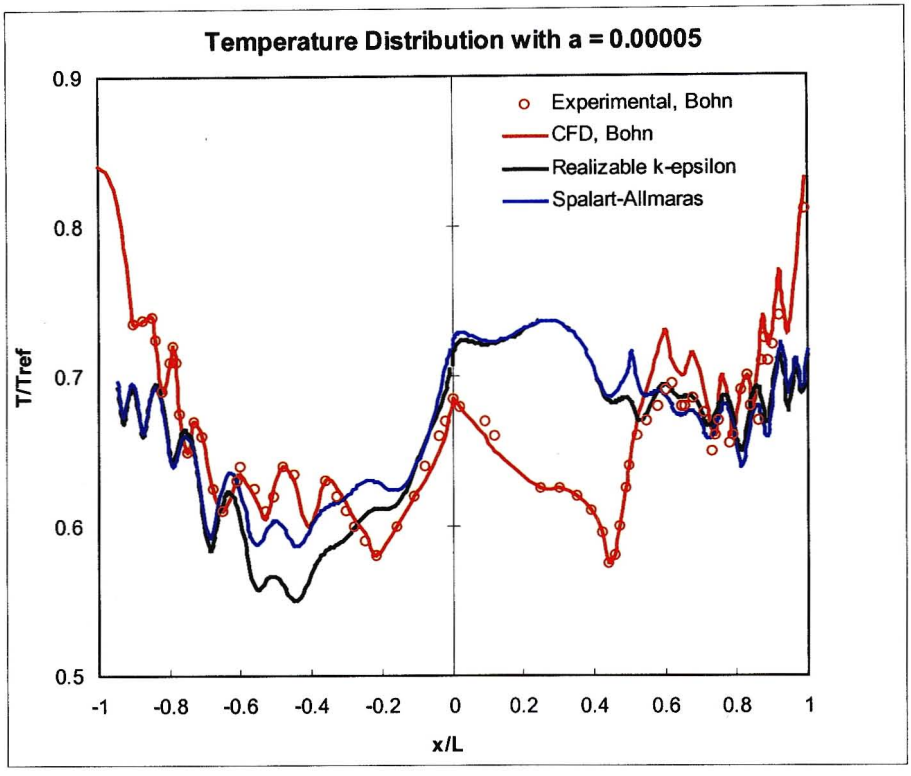

Figure 4-9a: Temperature distribution from aerodynamic analysis with heat transfer using the Realizable k - ε and Spalart-Allmaras turbulence models and a boundary layer mesh with a = 0.00005

The first cell height was fixed at a = 0.00001, and the growth rate and number of rows varied, keeping the boundary layer mesh depth fixed. This was done because the depth of 0.08 cm was sufficient to contain the viscous sub-layer around the entire blade. This is evident from the velocity vectors (Figures E-2e to g, Appendix E) and the Re_y plot (Figure E-2h) with Re_y = 200, indicating the demarcation between turbulent and viscous affected zones, coinciding with edge of the boundary layer mesh. One can therefore go on and say that boundary layer around the entire blade is fully contained within the boundary layer mesh.

Decreasing the growth rate of the boundary layer mesh, results in the increased over prediction on the pressure surface and well as leading edge. It also results in a mildly improved prediction

of the temperature spike due to the shock. The trailing edge region on both surfaces appears to be minimally affected by changes in the boundary layer mesh, and more significantly affected by changes in the first cell height. Figures 4-10 to 4-12 show that there is a trend towards an optimal set of boundary layer mesh parameters. A too course or too fine first cell height causes a shift away from the data, and so does decreasing the growth rate. Finally, the effect of node spacing was investigated. The simulations were done using the optimal boundary mesh, and two surface node interval spacings 0.16 cm (coarse) and 0.08 cm (fine) were investigated.

These results are shown in Figure 4-12. It can thus be concluded that the optimum boundary mesh should have a node interval spacing in the order of 0.08 cm, and boundary layer mesh parameters of, a = 0.00001 cm, GR = 1.72 and 16 rows. This mesh gives surface temperature distributions closest to the data, and will be the configuration used for the test cases. The pressure, temperature and heat transfer coefficient distributions from the final, validated CFD model is given in Figures 4-13a to c. The over-predicted temperature at the leading edge stagnation point is the result of the under-predicted local heat transfer coefficient at this point.

Adjusting the boundary layer mesh at the leading stagnation point to improve the predicted local heat transfer coefficient is difficult as it would result in large changes in the boundary layer moving away from the stagnation point causing highly skewed cells which adversely affects convergence of the solution. A similar situation exists in the vicinity of the strong shock on the suction surface. The sudden deceleration of the flow places very different boundary layer mesh requirements on each side of the shock. Accommodating these changes would again result in highly skewed cell being fitted between the drastically changing boundary layer mesh sides, which would destabilise the convergence. Based on these factors, the present predictions by the model were considered acceptable, as it would be known that further simulations with the model would behave in the same way.

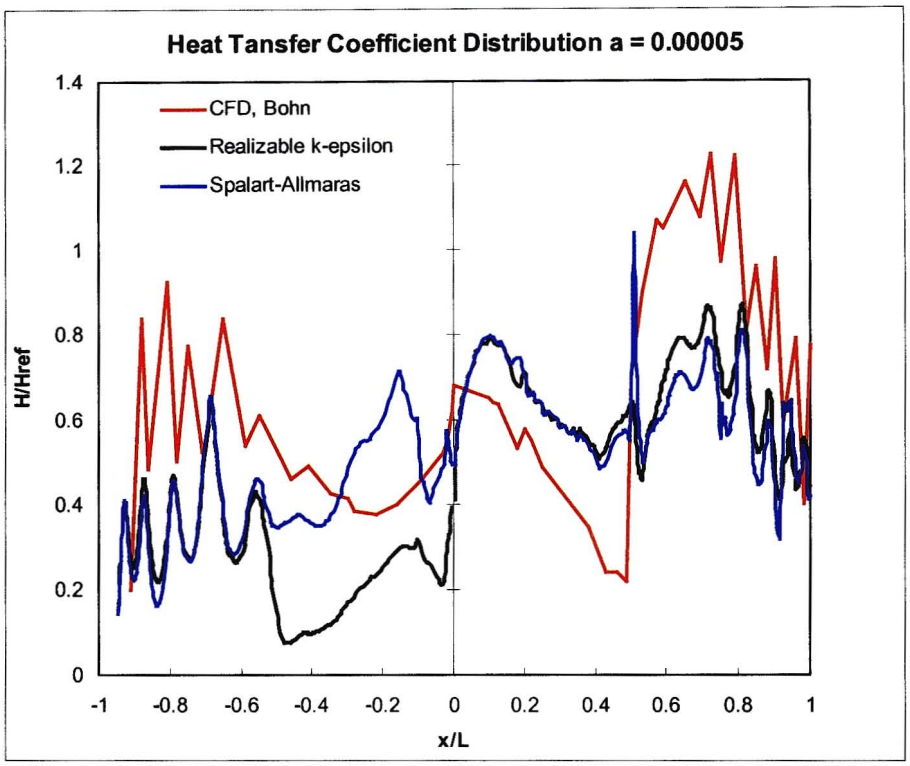

Figure 4-9b: Heat transfer coefficient distribution from aerodynamic analysis with heat transfer using the Realizable k - ε and Spalart-Allmaras turbulence models and a boundary layer mesh with a = 0.00005

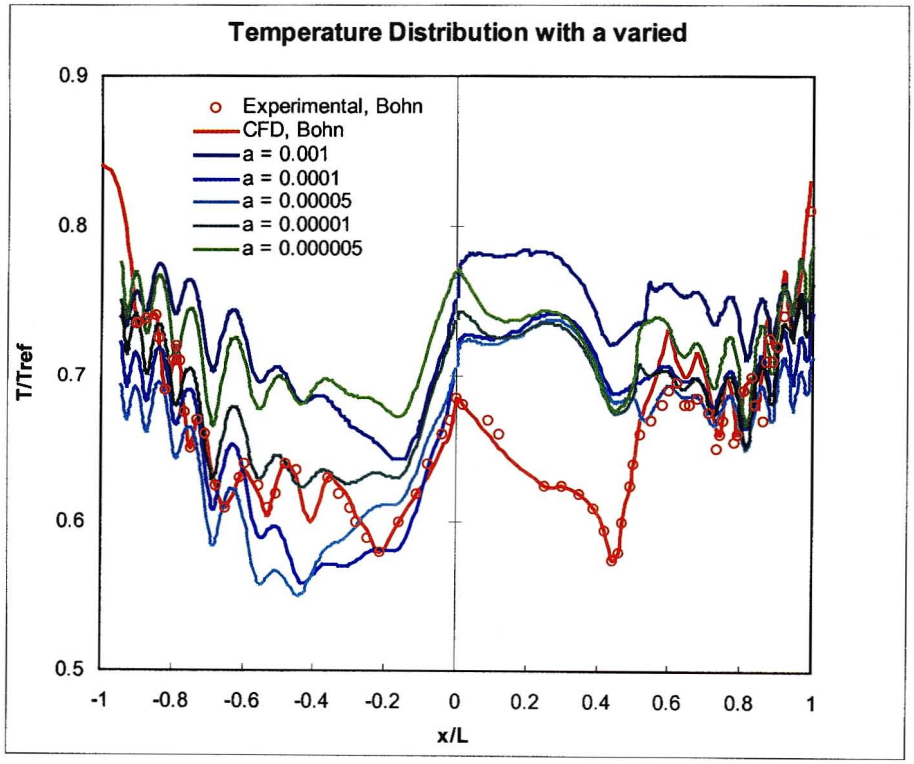

Figure 4-10: Temperature distribution from aerodynamic analysis with heat transfer using the Realizable k - ε turbulence models and varying first cell height

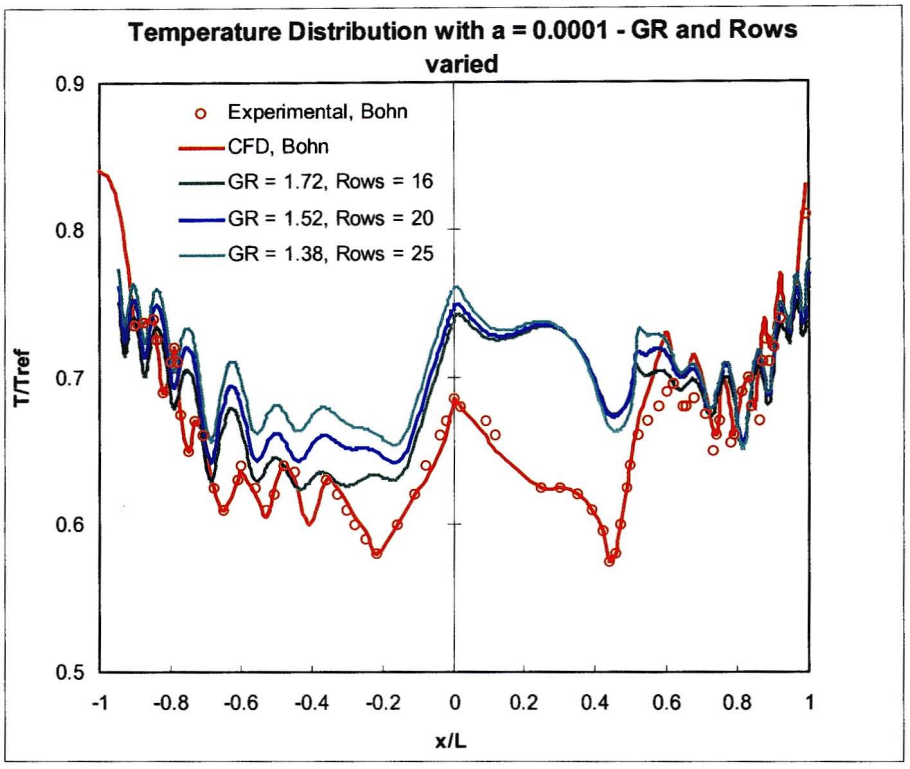

Figure 4-11: Temperature distribution from aerodynamic analysis with heat transfer using k-epsilon turbulence model for Mexit = 0.98 and a boundary layer mesh with a = 0.00001 and the growth rate and number of rows varied

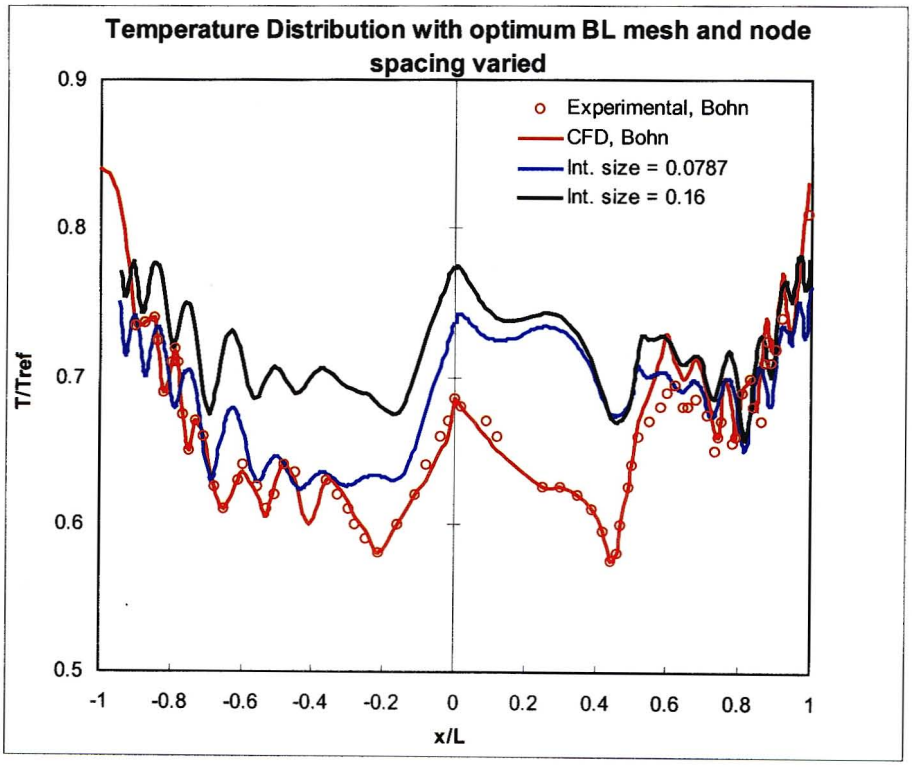

Figure 4-12: Temperature distribution from aerodynamic analysis with heat transfer using the Realizable k - ε turbulence models with optimum boundary layer mesh and node spacing varied

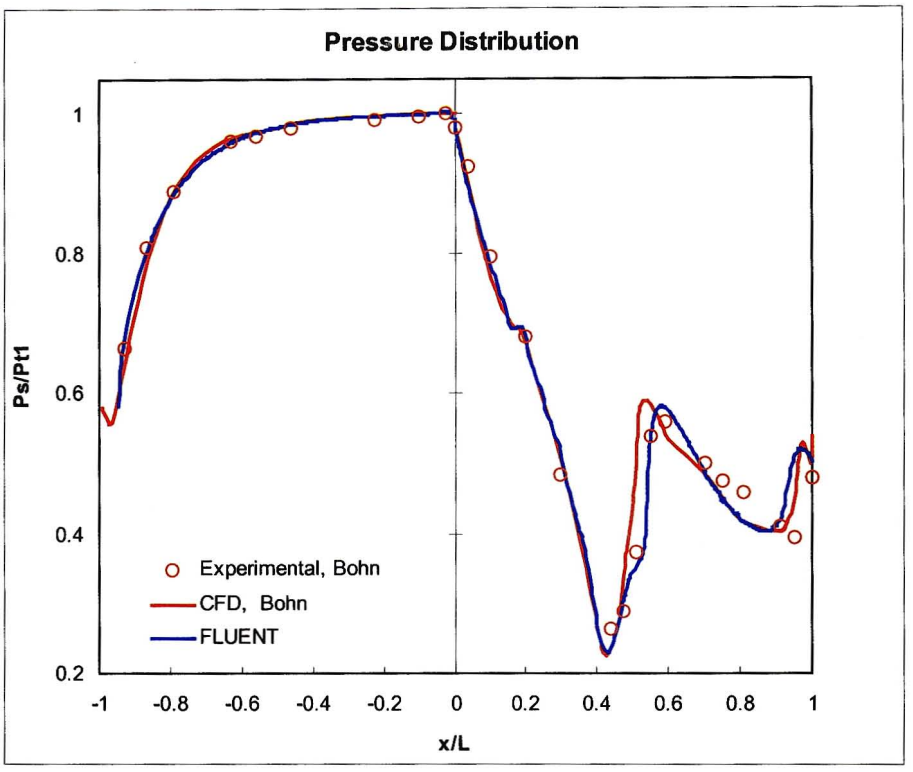

Figure 4-13a: Pressure distribution from aerodynamic analysis with heat transfer using the validated CFD model

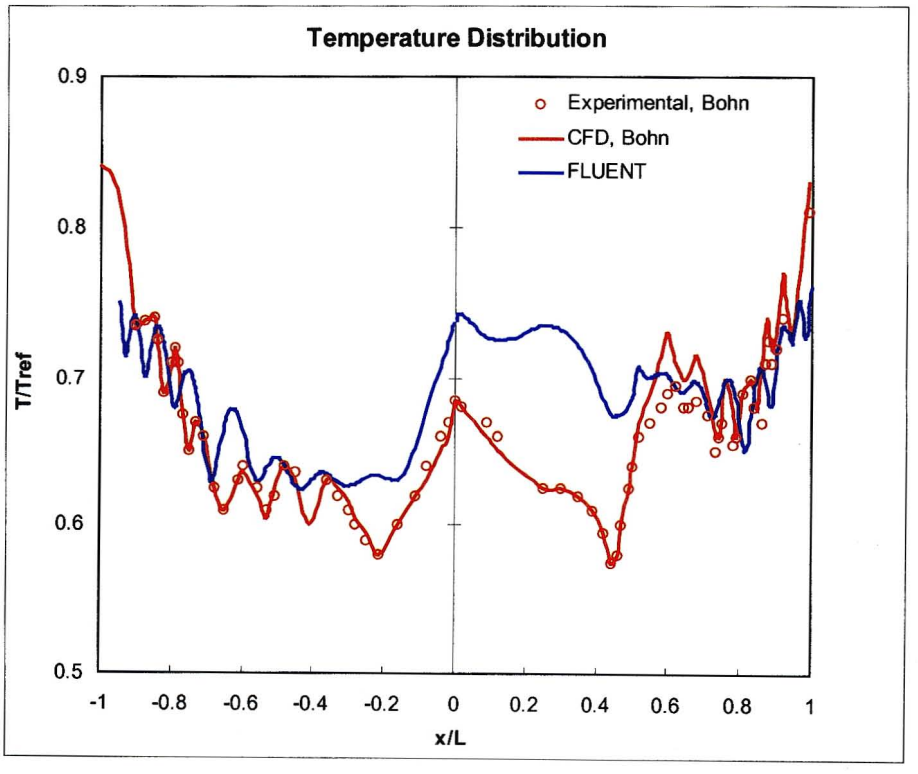

Figure 4-13b: Temperature distribution from aerodynamic analysis with heat transfer using the validated CFD model

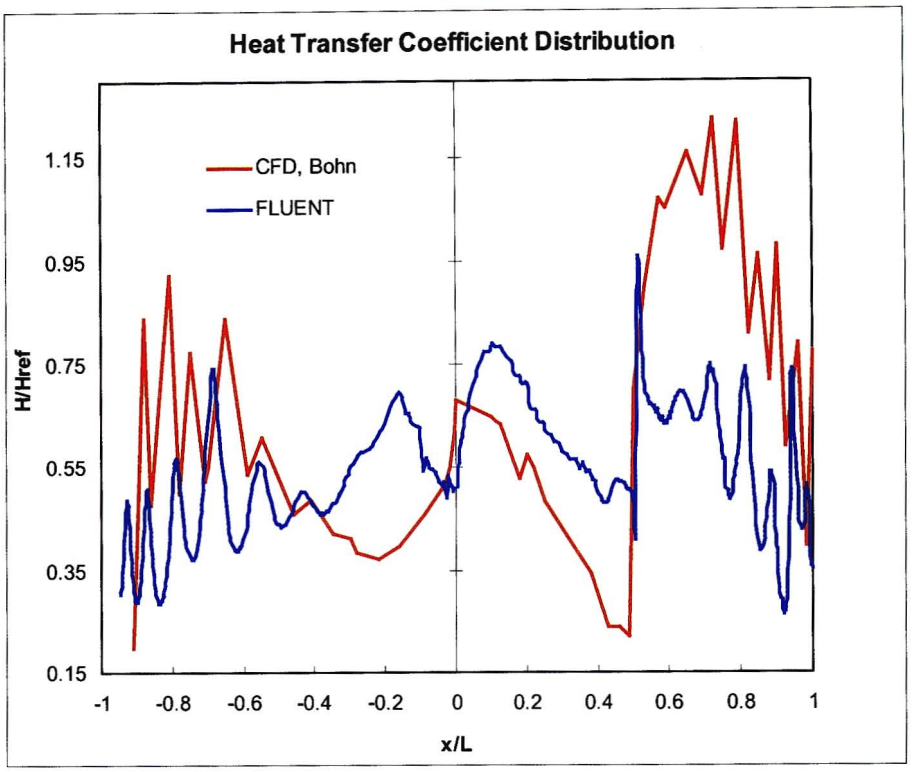

Figure 4-13c: Heat transfer coefficient distribution from aerodynamic analysis with heat transfer using the validated CFD model

4.4. Thermal Analysis

Validating FIDAP for performing a thermal analysis was done in two parts. Prior to the data for Mark II NGV becoming available, data for the case of a cylinder was used as a preliminary validation exercise. First, the steady state problem presented by Ali and Alam (1997) was solved in two FEM codes – MSC NASTRAN and FIDAP. The two solvers were then used to perform an unsteady thermal analysis for the same cylinder. Carslaw and Jaeger (1956) gave the unsteady cylinder temperature used for this analysis, with additional information regarding the thermal analysis coming from Goodier and Timoshenko (1970), Burgreen (1971), Hetnarski (1986) and Maya et. al. (1978).

4.4.1. Problem Definition if FIDAP

4.4.1.1. Cylinder – Steady State Case

The geometry used in Ali and Alam's analysis was a circular cylinder with a length to diameter ratio (L/D) of 10. The cylinder was constrained by fixing one end, which satisfied the plain strain conditions and equilibrium condition (Eq E-6, Appendix E). In FIDAP, the constraint condition was achieved by defining zero displacement for the fixed end via the BCNODE > DISPLACEMENT command. The temperature profile given by Equation E-2a was the boundary condition for the problem, and was inputted in FIDAP as Equation E-3. Inputting the temperature profile in the form of Equation E-2a was rather complex, but was easily done if the profile was represented as a polynomial that was function of one or more geometric coordinate.

Equation E-2a gives temperature as a function of radius; therefore a polynomial approximation of Equation E-2a should use the radius as the independent variable. The coordinate system for the geometry was changed from the default Cartesian system to cylindrical coordinate system using the COORDINATE command. Equation E-8 was inputted to define the temperature profile as boundary condition through the POLYNOMIAL keyword in the BCNODE command. From Figure 4-14, it is clear that the approximation (Eq E-3) is an accurate representation of the temperature profile (Eq E-2a). The polynomial was defined such that the temperature at the centre was 293 K and 593 K at the surface.

The material properties of carbon steel were used for the cylinder (Table B-1, Appendix B). The properties could have been arbitrarily chosen since the results were non-dimensionalised, but carbon steel data was easily located and representative of turbine blade material properties. The inputs for MSC NASTRAN were almost identical to those used for FIDAP. The only differences were because of slightly different interfaces between the two codes.

4.4.1.2. Cylinder – Unsteady Case

The same geometry, computational grid and constraints from the steady state case were used for the unsteady analysis. The boundary condition for the unsteady case was a constant heat flux of 150 kW/m^2 applied to the surface of the cylinder. This was inputted in FIDAP through the HEAT keyword in the BCFLUX command. The initial condition was a uniform temperature of 298 K defined using the TEMPERATURE keyword in the ICNODE command. It was

determined; from 1-D conduction heat transfer theory, that a heat flux of 150 kW/m^2 would results in a temperature difference between the cylinder centre and surface of 200 K. This ensured that the unsteady profile would, after a large time (i.e. once the solution reached steady state), be identical to the steady state profile given by Ali and Alam (1997).

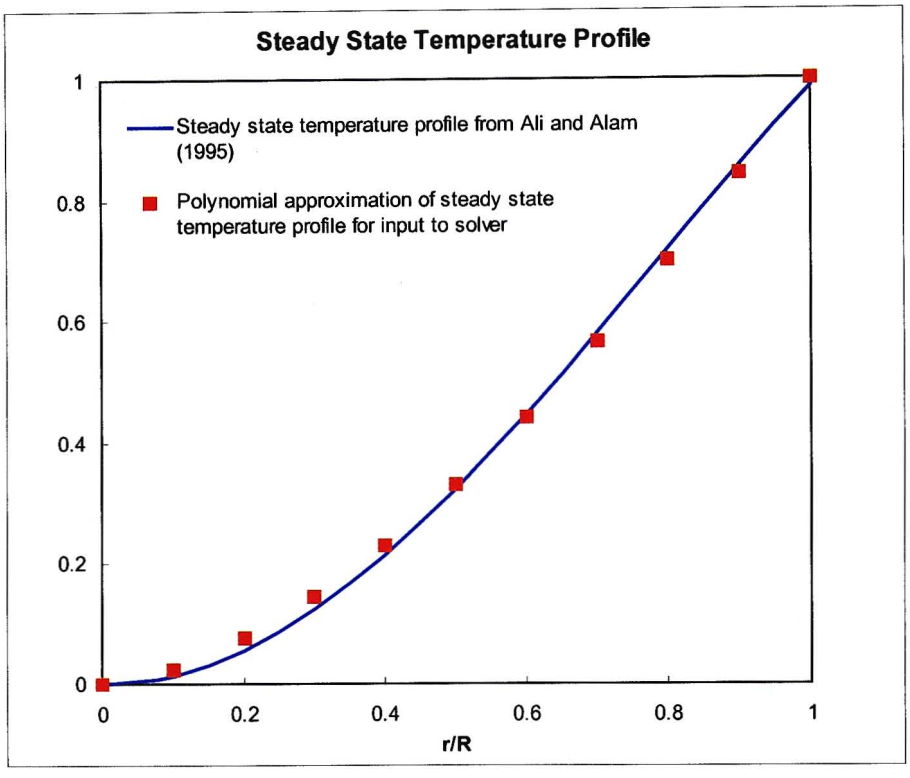

Figure 4-14: Temperature profile from Ali and Alam (1997) together with the polynomial approximation

4.4.1.3. Mark II NGV

The case of the Mark II NGV was solved in FIDAP only, because of the computational grid issue discussed in chapter 3 and the findings from the thermal analysis of the cylinder. Defining the blade as a DEFORMABLE entity enables the structural solver, which introduces the deformation variables into the problem. Being a 2-D simulation, plain strain conditions and equilibrium condition (Eq E-6) are imposed through the PLANSTRN keyword in the STUCTURALOPTIONS command. The thermal stress form of the classical stress equations are invoked by the THERMAL STRESSES keyword also in the STRUCTURALOPTIONS command.

The boundary conditions for the cooling holes are convective heat transfer coefficients. These were entered via the HTRANSFER keyword, which is invoked by defining the cooling holes as CONVECTION boundaries. The blade surface was defined as PLOT boundaries, which are 'do nothing' boundaries, meaning that no keywords are associated with that boundary and all boundary conditions have to be explicitly defined. The boundary condition for the blade surface was the surface temperature profile, which was imposed by specifying the temperature at each node on the surface. This was done through the TEMPERATURE keyword in the BCNODE command.

The properties for the blade were for ASTM 310 stainless steel, which were obtained, form a materials handbook (ASM International). These were entered through the relevant material property keywords and are shown in table B-2, Appendix B. Young's modulus and thermal expansion coefficient were defined as functions of temperature. This is done by listing data points associated with the CURVE keyword, which FIDAP joins in a piece-wise linear fashion.

4.4.2. FEM Computational Grid Development

4.4.2.1. Cylinder

For the steady state analysis, Ali and Alam employed a grid of 750 elements – 25 nodes in the radial direction and 30 along the length. It was attempted to use similar parameters for the grids in FLUENT and NASTRAN, and to generate identical grids for both but that was not possible because the two solvers used different formulations for creating the geometry. There was also the constraint of the 5000 node licence limit in NASTRAN. A grid with hexahedral elements was desirable, as it would ensure a consistent cross-sectional grid along the length of the cylinder. This also makes defining a line in the radial direction along which to plot the results much easier than if a tetrahedral grid was used.

In FIDAP, it was not possible to specify the number of elements along the length of the cylinder, only on the circular edge. The length was discretized using the element size specified on the circular edge. In NASTRAN, one can specify the element size on the circular edge as well as the length, which turned out to be advantageous for not violating the node licence limit. For both solvers, the circular edge was discretized with 36 elements, which resulted in approximately 198 elements through the cross-section in FIDAP and 148 in NASTRAN. The total number of elements for the FIDAP grid was 15048 with 72 elements along the length. In

NASTRAN, 25 elements were specified along the length, which resulted in a 3700 element grid for the cylinder. The resulting grids are shown in Figures 4-15a and b, and 4-16a and b.

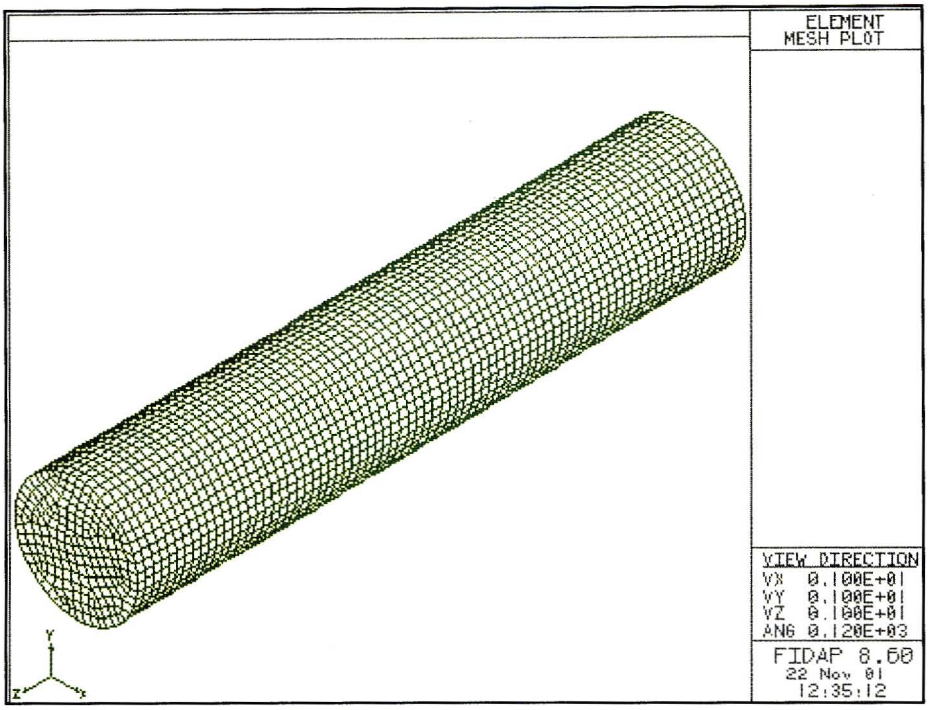

Figure 4-15a: 3-D computational grid used to discretize the cylinder for the FIDAP solution to the steady state case

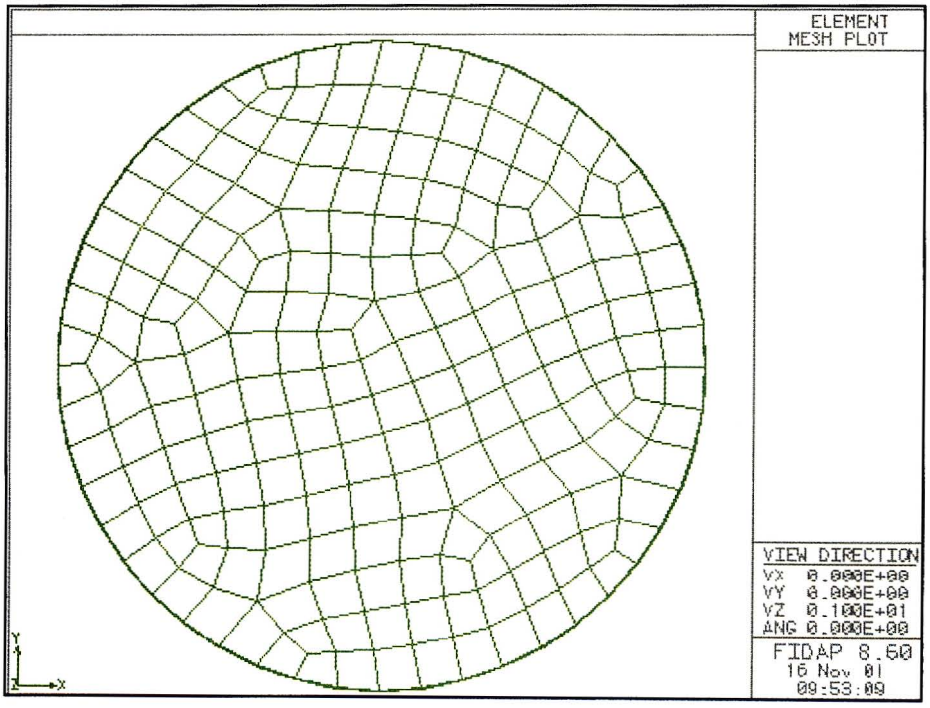

Figure 4-15b: 2-D cross-section of the FIDAP computational grid for the steady state case

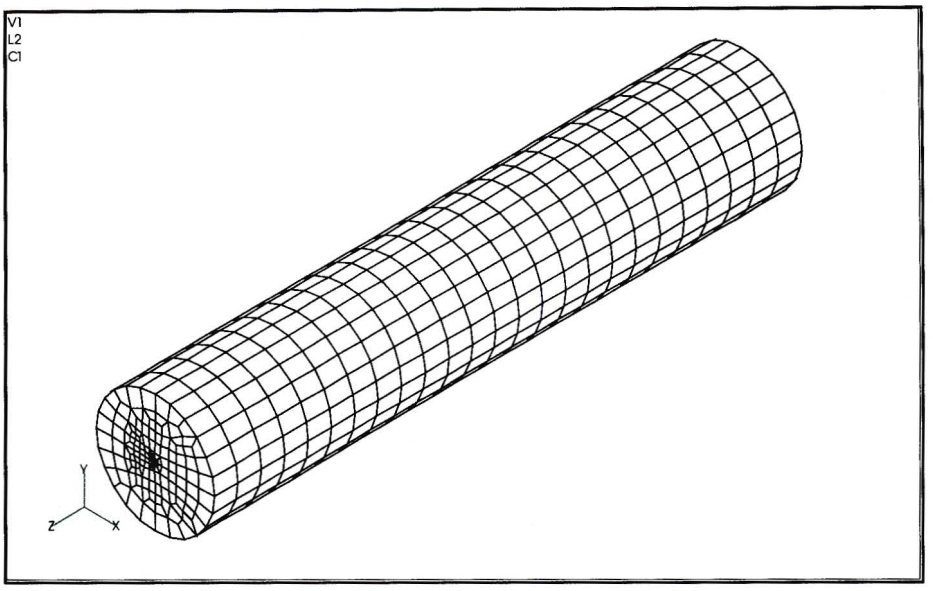

Figure 4-16a: 3-D computational grid used to discretize the cylinder for the NASTRAN solution to the steady state case

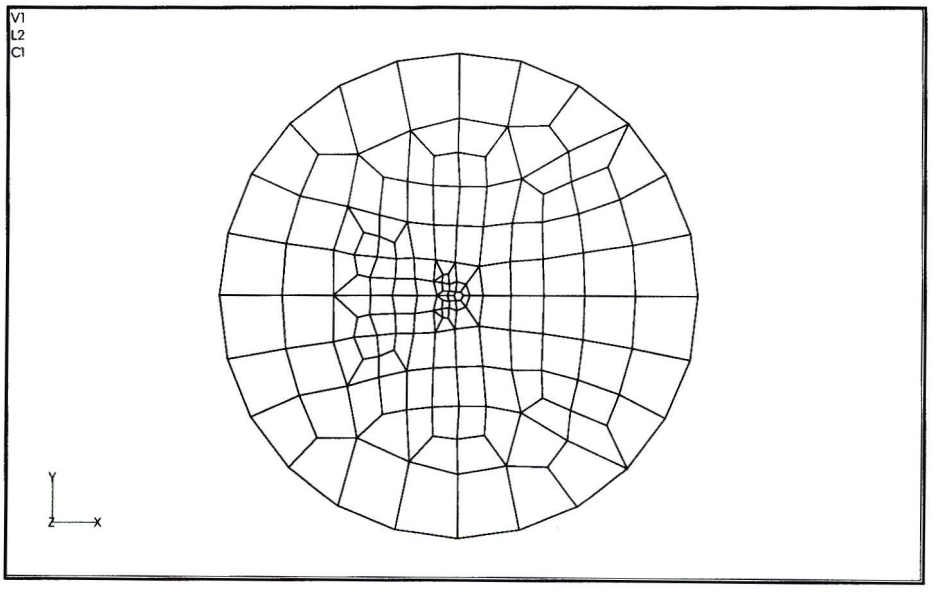

Figure 4-16b: 2-D cross-section of the NASTRAN computational grid for the steady state case

4.4.2.2. Mark II NGV

Triangular elements were used to discretize the Mark II NGV geometry because, as discussed earlier, identicle grids between FLUENT and FIDAP had to be maintained. The element size of 0.0787 cm on the blade surface was specified from the aerodynamic analysis. The cooling hole

edges were discretized with 20 elements, which resulted in the 5025 element grid shown in Figures 4-17a and b.

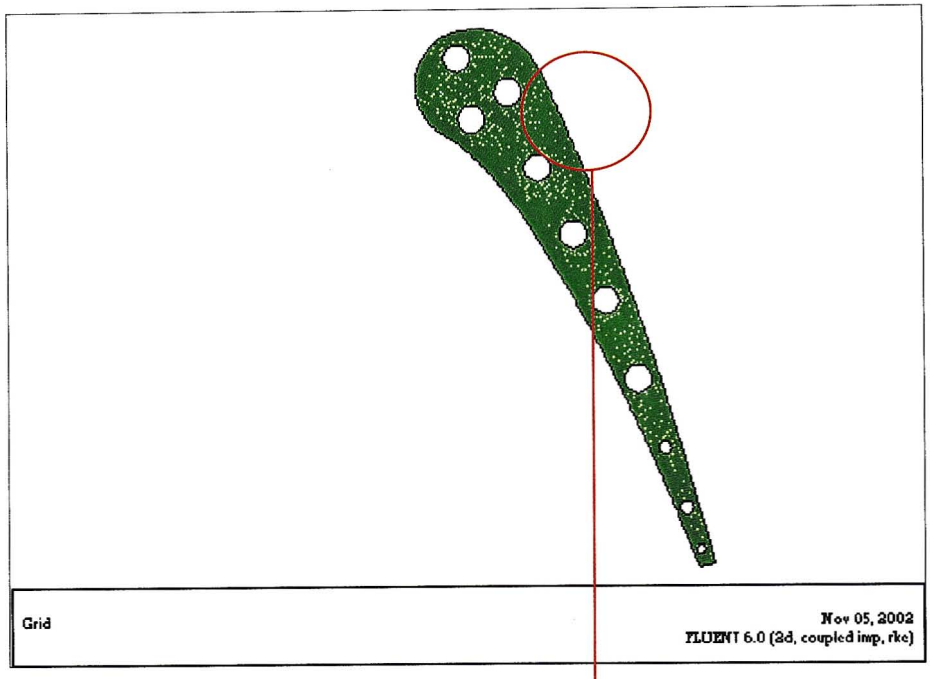

Figure 4-17a: Computational grid for Mark II NGV

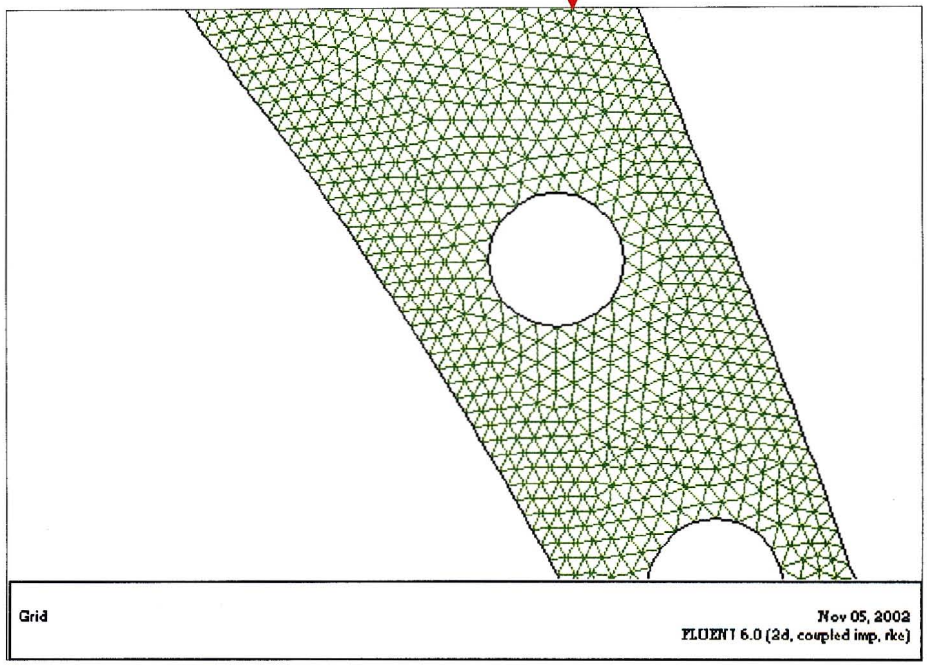

Figure 4-17b: Close-up of computational grid for Mark II NGV

4.4.3. Validation of FIDAP

4.4.3.1. Cylinder – Steady State case

The results for the thermal stresses in a cylinder with a steady state temperature profile (Eq E-2a, Appendix E) given by Ali and Alam were presented as graphs of radial variation of radial, tangential and axial stress (σ_r, σ_θ and σ_z respectively). The solution time for both FIDAP and NASTRAN was approximately 3 minutes. The cylindrical coordinate system, defined in the pre-processing stage to input the boundary condition in polynomial form, for both NASTRAN and FIDAP, was not carried over to the post-processing stage. The results are therefore expressed in Cartesian coordinates (σ_x, σ_y and σ_z) as shown in the contours (Figures E-3 and 4a to c).

The stresses in the Cartesian coordinate system can be selectively plotted to represented stresses in the cylindrical coordinate system. Plotting the results on a line coincident with the x-axis will results in σ_x being equivalent to σ_r, σ_y being equivalent to σ_θ and σ_z is unaffected. The stresses were non-dimensionalised by dividing the stresses by the term $E\alpha\Delta T$, yielding non-dimensionalised radial, tangential and axial stresses - σ_{Nr}, $\sigma_{N\theta}$ and σ_{Nz}. These results are shown in Figure 4-18a, b and c.

Both solvers are able to accurately predict the principle stress trends. The predictions accurately follow the data for radial and tangential stress except at the surface (r/R = 1), where NASTRAN over-predicts the data and FIDAP under-predicts. This trend is more pronounced in the radial stress plot. The reason for the deviation of the FIDAP solution from the data at the surface is not grid related as no change in the plot occurred when the solution was repeated with a finer grid. A solution with a finer grid could not be done in NASTRAN because of the node licence limitation, but the results were accurate enough to not warrant testing a finer grid. The other possible reason for the difference could be related to post-processing.

FIDAP tends to over-predict the axial stress for $0.6 < r/R < 1$ by at most 60 %. This trend was still present when a finer grid was tested. NASTRAN on the other hand, follows the data almost identically. Both solvers correctly predict the distribution of the principle stresses with NASTRAN generally being more accurate than FIDAP. Although NASTRAN is marginally more accurate, FIDAP will still be used for the test cases because of the reasons discussed earlier. The purpose of using both solvers for the steady state case was to so that a reference

between NASTRAN and FIDAP could be established before the two were used to solve the unsteady case.

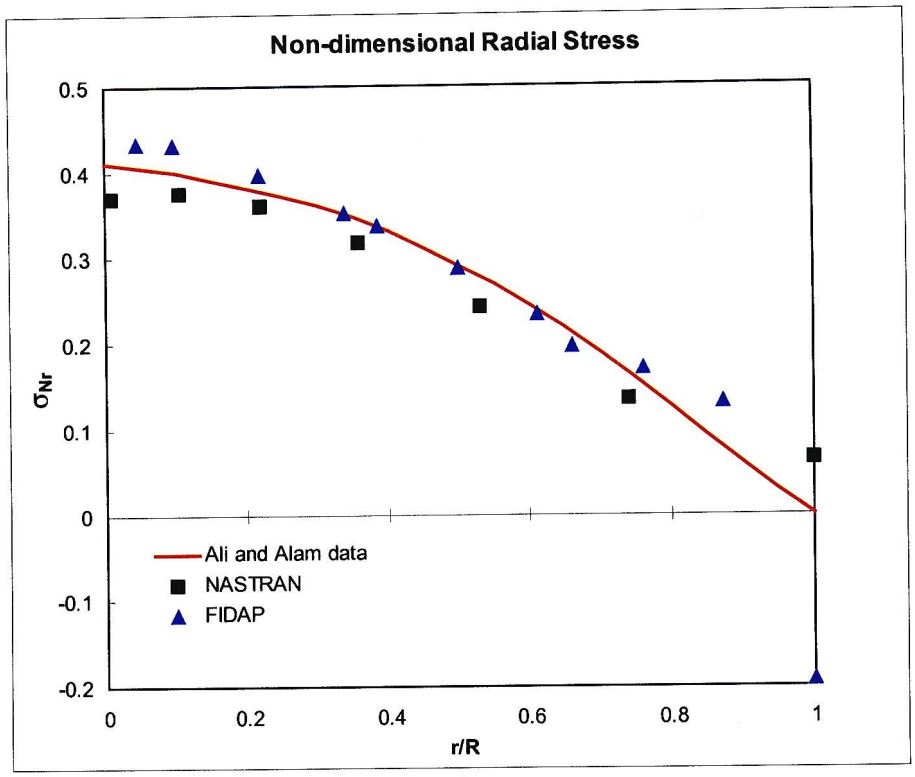

Figure 4-18a: Non-dimensionalised stress in the radial direction for a cylinder with steady state temperature profile

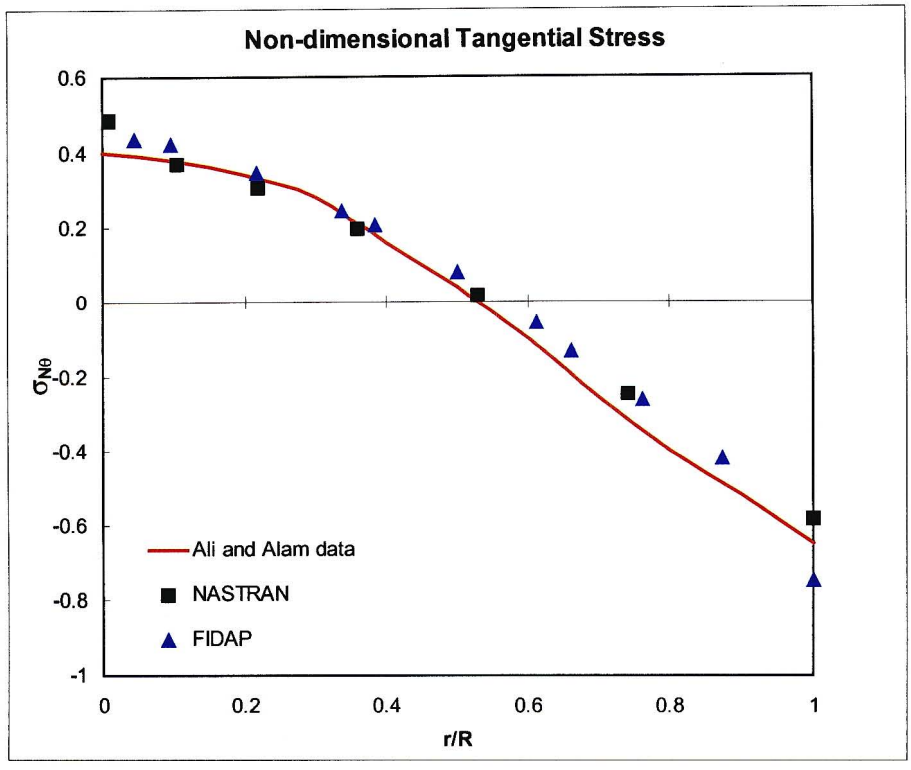

Figure 4-18b: Non-dimensional stress in the tangential direction for cylinder with steady state temperature profile

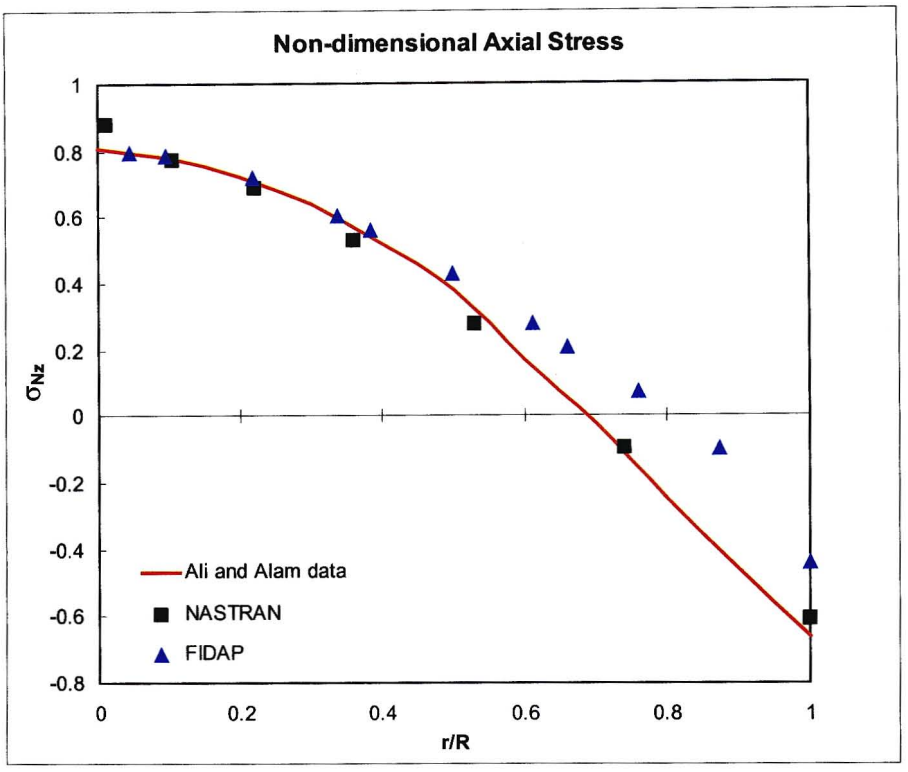

Figure 4-18c: Non-dimensionalised stress in the axial direction for a cylinder with steady state temperature profile

4.4.3.2. Cylinder – Unsteady Case

The nature of the thermal stress profiles will exhibit the same characteristics of the unsteady temperature boundary condition for the problem. The temperature profiles (Carslaw and Jaeger 1956) will start out flat i.e. equal to the initial temperature everywhere along the radius, and then increase from the surface inward as time elapses until, at some large time, when it will assume an unchanging, steady state profile. For times after the steady state profile has been reached, the actual temperature values will still increase but the distribution will remain the same, hence the term steady state. The thermal stress profiles will follow the same pattern with the distribution of the steady state profile being already known. From the elementary examples given in Goodier and Timoshenko (1970), Burgreen (1971) and Hetnarski (1986), one can get an idea of what the shape of the thermal stress profiles during the transient temperature phase, will look like.

The non-dimensionalised temperature profiles predicted by FIDAP and NASTRAN are shown in Figures 4-19a and b respectively. The profile labelled 1 is the steady state profile with '1' indicating the non-dimensionalised time taken for the temperature distribution to reach steady state. The profiles labelled 0.13, 0.29 and 0.62 are for the transient phase and indicate the

fraction of steady state time at which those profiles occur. Both solvers predict the unsteady temperature behaviour almost identically and they are consistent with the analytical trend given in Carslaw and Jaeger (1956).

FIDAP and NASTRAN use two slightly different solution procedures to solve the unsteady problem. At each time step, FIDAP solves the temperature distribution first and then the stress distribution. NASTRAN solves the only temperature distribution as an unsteady problem. The thermal stress distributions have to be solved as steady state solutions with the temperature distributions imposed as boundary conditions for the thermal stress problem. Solving the thermal stress problem as steady state is justified since stresses in a solid move at the speed of sound in that medium, this is almost instantaneous.

The two solution procedures are, for all intents and purposes are identical, and should produce the same results. Figures 4-20a and b indicate otherwise. The trends predicted by NASTRAN appear to be correct, based on the trends seen in the examples in Goodier and Timoshenko (1970), Burgreen (1971) and Hetnarski (1986). The severe deviation of the FIDAP prediction was first thought to be because the solution did not fully converge at each time step. The convergence history in the FDSTAT file was scrutinized and it was observed that convergence reached when the temperature changed by less than 10^{-6}, which was the user-specified convergence tolerance for all variables.

The displacement variables (d_x and d_y) were still oscillating when convergence was reached but the changes were of the order of 10^{-8}. This was deemed to not have a significant effect on the solution, and the reason for deviation in the FIDAP predictions can only be due to some solution parameter, which was over looked, or some error in the solver itself. The former is unlikely as assistance was sought from more learned FIDAP users, who failed to provide an explanation. The FIDAP solution was repeated by first solving the temperature only, and then solving the steady state stresses with the temperature profiles as the boundary conditions, as is done in NASTRAN. These FIDAP results are shown in Figure 4-20c.

These results are very similar to the NASTRAN prediction (Figure 4-20a). Cleary FIDAP is able to correctly predict thermal stresses when solved as steady state. It can thus be concluded that FIDAP cannot be used to solve an unsteady thermal stress problem using the default unsteady solver formulation because the results cannot be trusted and the reason for this is unclear. It can be used to solve an unsteady heat transfer problem but the resulting stresses must be solved as a steady state solution. It has been shown that FIDAP can accurately the thermal stresses when the problem is solved in this manner.

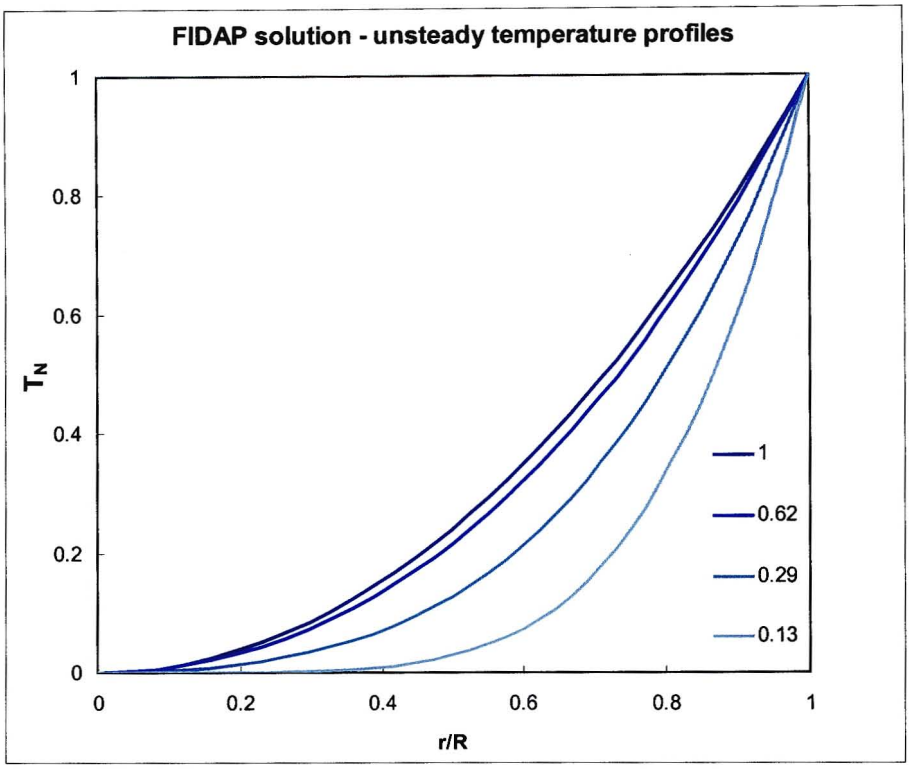

Figure 4-19a: FIDAP solution of unsteady, non-dimensional temperature profiles for a cylinder

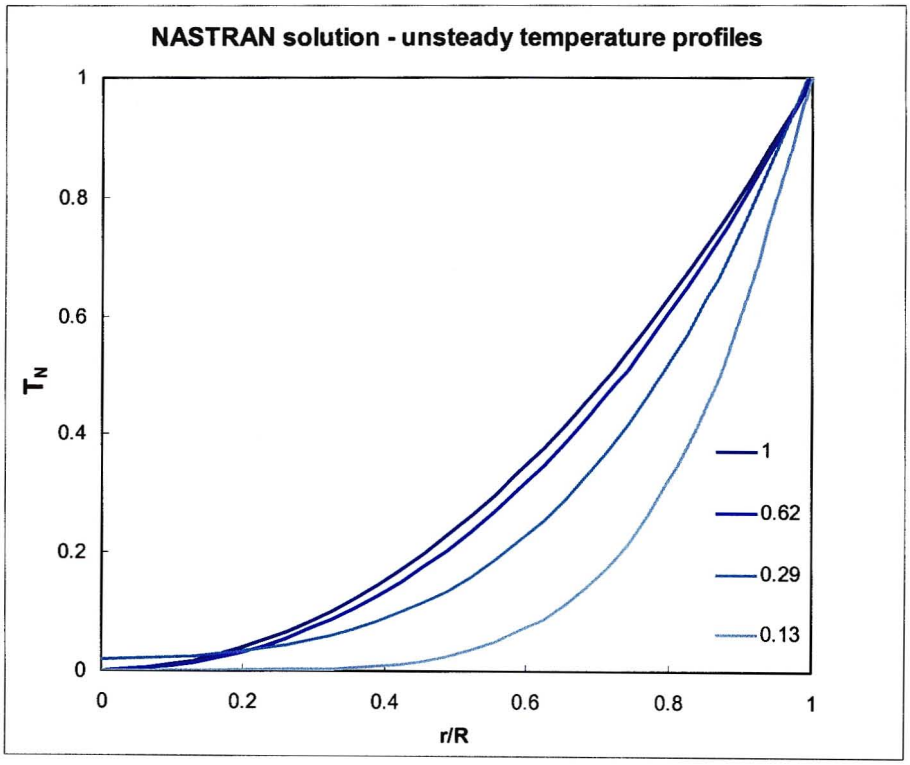

Figure 4-19b: NASTRAN solution of unsteady, non-dimensional temperature profiles for a cylinder

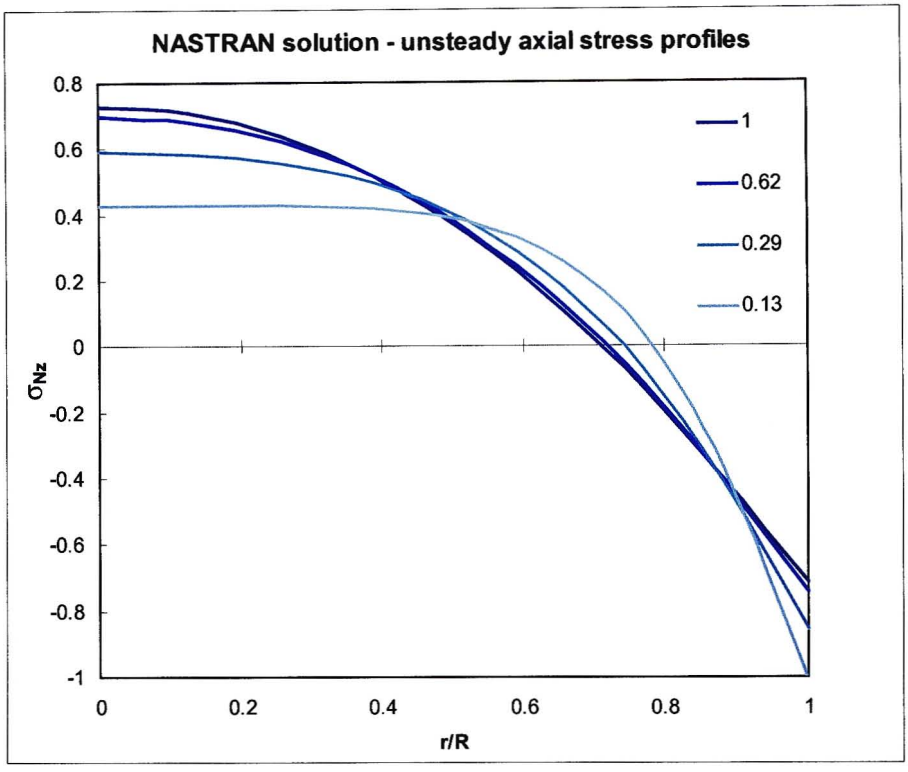

Figure 4-20a: NASTRAN solution of non-dimensional axial stress profiles for unsteady temperature

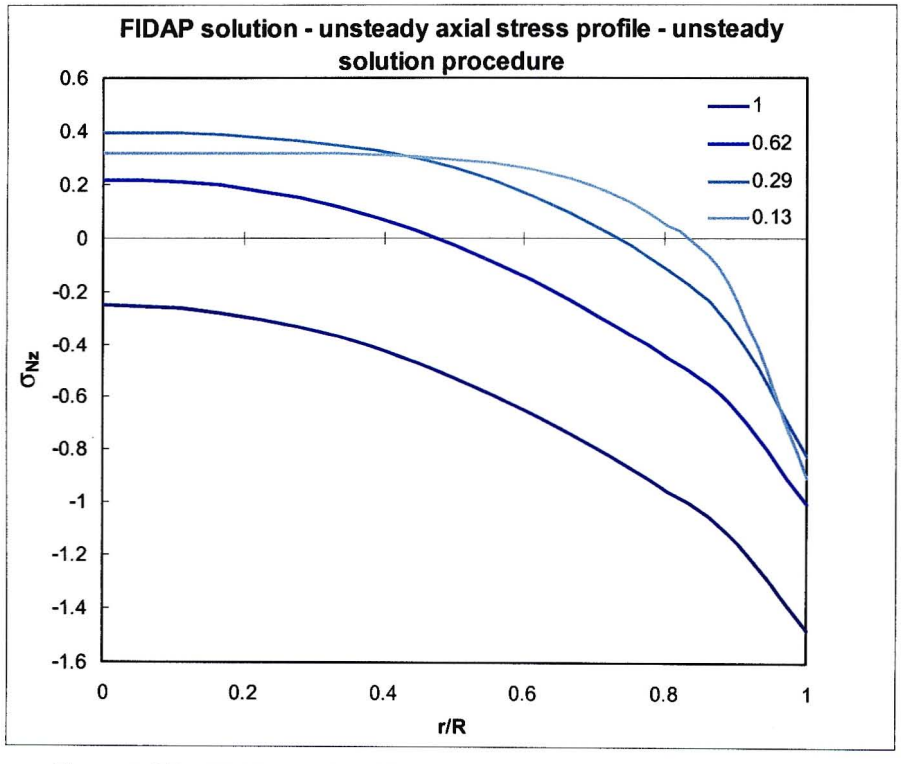

Figure 4-20b: FIDAP solution of non-dimensional axial stress profiles for unsteady temperature using default unsteady solution procedure

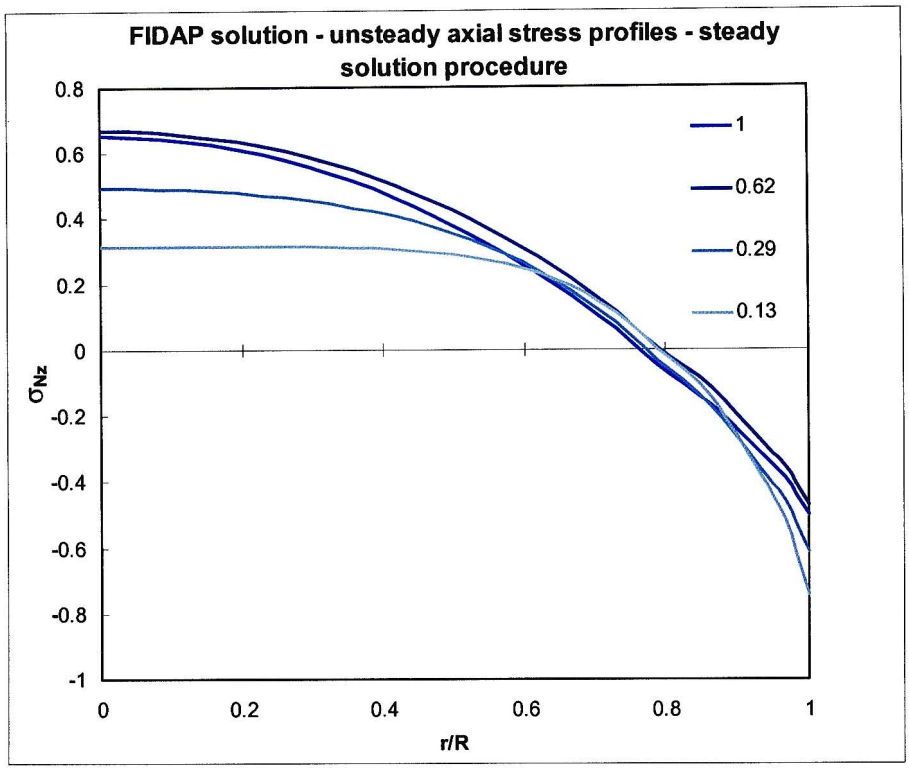

Figure 4-20 c: FIDAP solution of non-dimensional axial stress profiles for unsteady temperature using steady solution procedure

4.4.3.3. Mark II NGV

The thermal stress problem for the Mark II NGV requires the steady state solution of the conduction equation and the thermal stress equations, which FIDAP is fully capable of doing. The contours of temperature and equivalent stress (σ_e) are compared to those given by Bohn (Figures E-5 and 6a and b). The FIDAP temperature contours compare very well to Bohn's results. The locations of the overall maximum temperature, as well the minimum temperatures on the pressure and suction surfaces are correctly predicted. The FIDAP contours show and average over-prediction of 1.6 % ($\approx$ 7 K) and a worst case of 4 % ($\approx$ 18 K). The reason for this is believed to be the result of using constant thermal conductivity in the simulation whereas Bohn used a temperature dependant thermal conductivity. The use of temperature dependant thermal conductivity was intended but aborted due to a FIDAP input problem. Also, the resulting temperature showed no similarity to the data, so a constant value was chosen.

In the leading edge region, the FIDAP σ_e contours show a similar trend to Bohn, with a high equivalent stress at the edge of cooling hole 2. FIDAP predicts a σ_e of 300 MPa at this point whereas Bohn predicts 431 MPa, which is the max σ_e. In the region between cooling holes 2

and 3, FIDAP predicts a stress of 201 MPa while Bohn predicts 221 MPa. The minimum equivalent stress for the leading edge region is predicted at the same location as Bohn but is under-predicted by 35 % (≈ 26 MPa). The maximum equivalent stress is under-predicted by 27 % (≈ 116 MPa). FIDAP predicts the maximum stress at the location corresponding to the minimum temperature on the pressure side.

The stress contours in the region between holes 4 to 7 are also similar to Bohn's. Stresses of 49 MPa and 17 MPa are predicted at locations where Bohn predicts 75 MPa and 22 MPa respectively. The minimum equivalent stress is predicted at the correct location and is again under-predicted. The stress contours in the trail edge region (holes 8 to 10) differ significantly from Bohn's. A stress of 143 MPa is predicted at the edge of hole 9, which corresponds to 148 predicted by Bohn. The contours then decrease to 49 MPa outwards from hole 8 whereas Bohn's prediction increases outwards to stresses of 221 MPa and 294 MPa.

The temperature, σ_e and σ_z plotted along the line AB (line AB is shown in Figure E-6b) are shown in Figure 4-21a, b and c respectively. The x-axes in Figures 4-21a to c are labelled as position, which represents the blade thickness along AB. The FIDAP curves stop at a position of approximately 0.0164 m, which is slight short of Bohn's curve. The reason for this is that firstly, Bohn did not give the exact coordinates of A and B, and second, the LINE plot command requires that the line be defined by entering the node number of the start and end nodes. The points that lie on the line are used as data points to plot the function value. Using this command, the position of line AB was approximated and the curves in Figures 4-21a to c show that line AB was approximated fairly accurately.

The temperature curve along AB (Figure 4-21a) again shows that FIDAP is slightly over-predicting by up to 4 %, as was shown by the temperature contours. The curve trend is correctly predicted with the temperature at the positions 0 m and 0.0175 m, corresponding to the pressure and suction surfaces, being higher than the inside of the blade. The trends for σ_e and σ_z (Figures 4-21b and c) are also correctly predicted. The σ_e values are positive because of the definition of equivalent stress (Eq E-8). The positions of minimum σ_e are predicted slightly further along AB, and the peak between the minimums is under-predicted and is also flatter than Bohn's curve.

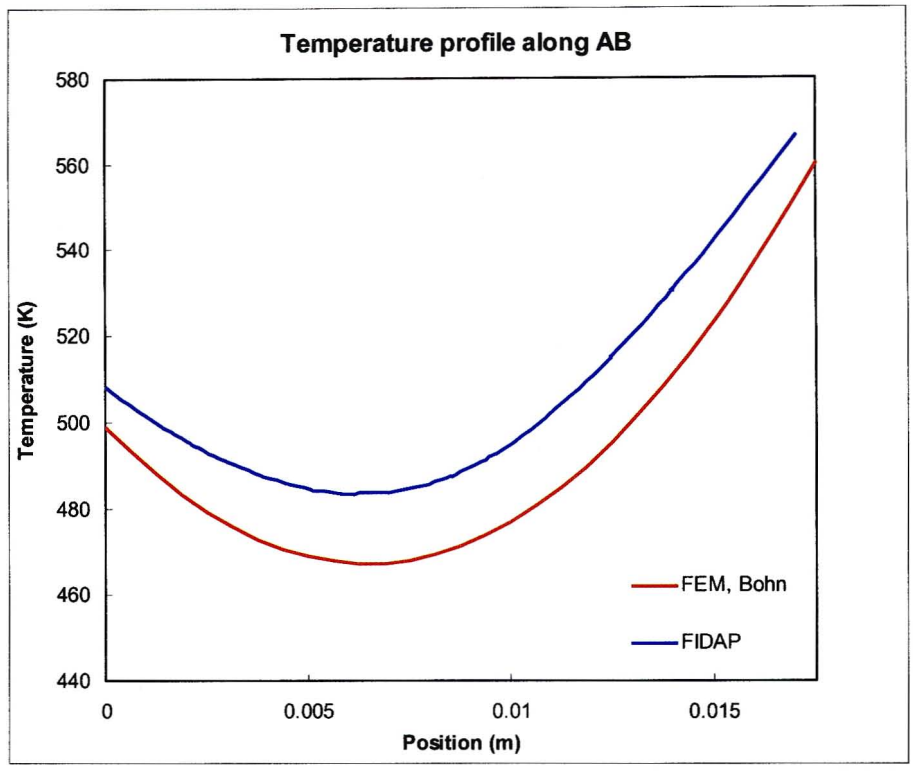

Figure 4-21a: Temperature profile along line AB through the blade thickness

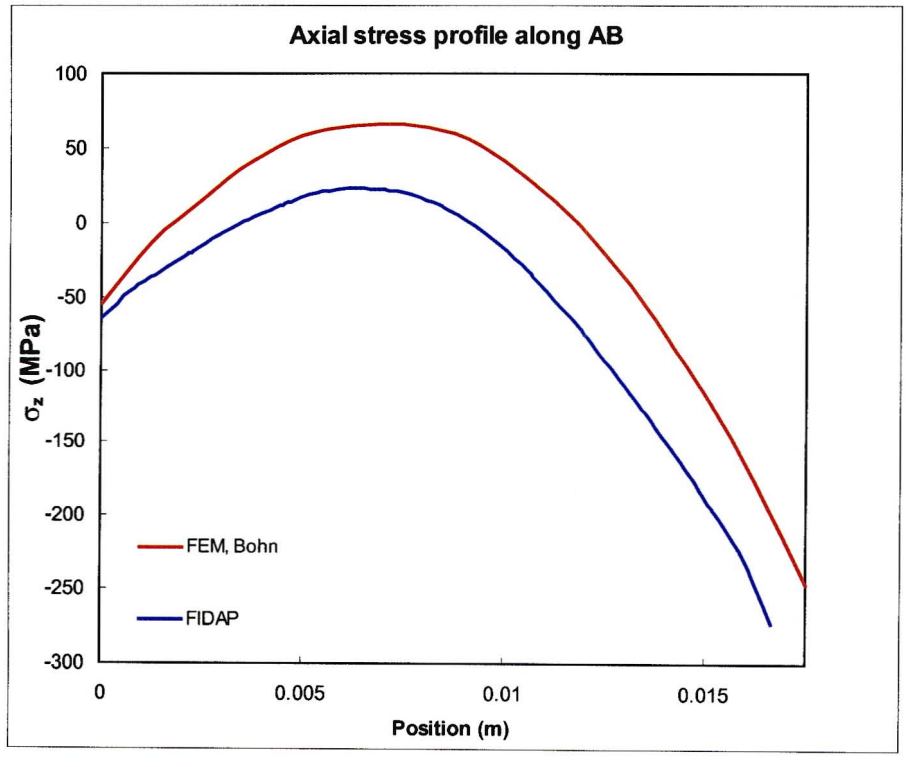

Figure 4-21b: Axial stress profile along line AB through the blade thickness

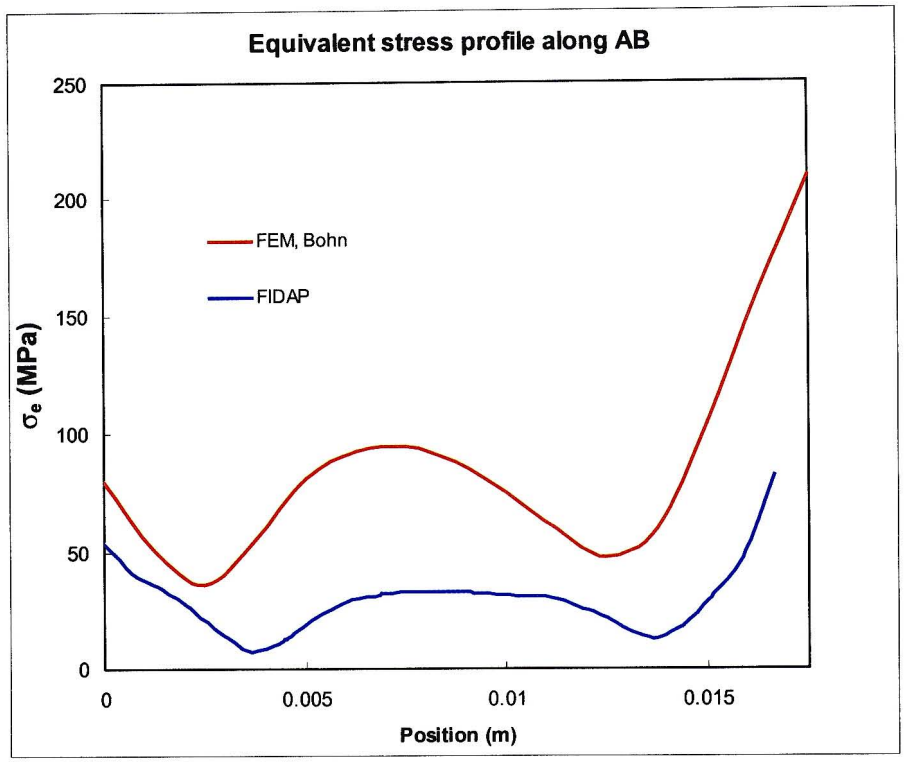

Figure 4-21c: Equivalent stress profile along line AB through the blade thickness

In the region left of the first minimum and right of the second, the FIDAP curve decreases and increases respectively, with the same gradient as Bohn's curve. The σ_z curve also tracks Bohn's with almost the same gradients. The positions of $\sigma_z = 0$ corresponds to the positions of minimum σ_e, which is also seen on Bohn's curves. Bohn indicated that stresses in the z-coordinate direction occur as a result of temperatures above and below the stress free temperature, with $\sigma_z = 0$ and σ_e minimum corresponding to the stress free temperature. These points correspond to 488 K for FIDAP but to 480 K for Bohn's curves. The graphs in Figures 4-21a to c show that σ_z and σ_e are under-predicted by as much as 60 MPa but it is also seen that FIDAP is able to predict the stress variation correctly.

The equivalent stress contours from FIDAP show the similar trends as Bohn's over approximately 90 % of the blade cross-section. The stresses are consistently under-predicted and the extent of under-prediction appears to be proportional to the stress magnitude. The difference in the results is possibly due the fact that the material properties (in particular the temperature dependant properties) used by Bohn, differ from those used in FIDAP. The reason for the severe difference in the results for the trailing edge region is unclear but it may be the result of how the initial stress free temperature was inputted in FIDAP.

A study by Moll (1990) (discussed by Bohn) showed that, for a plain strain problem, in order to satisfy the equilibrium condition shown in Equation E-6, and area weighted initial stress free temperature must be used. Bohn indicates that for the Mark II problem being simulated, Moll (1990) showed that this temperature was 488 K. The author was unable to obtain a copy of the study by Moll but proceeded to use 488 K as claimed by Bohn. The initial stress free temperature was inputted in FIDAP through the REFTEMP keyword in the VOLUMEXPANSION command.

The FIPREP manual (FLUENT.INC 2001) indicates that FIDAP takes this temperature to be the initial strain free temperature. The author found no other user input in FIDAP that related to the initial stress free temperature. Therefore, specifying the stress free temperature as indicated, was deemed correct; taking into account that the resulting stress contours over 90 % of the blade being correctly predicted and that Bohn showed the strain to be nearly directly proportional to the stress. This means that the mystery of the trailing edge stress results not correlating with the data is still unsolved.

With the temperature and stress variation over approximately 90 % of the blade cross-section predicted correctly, it could be concluded that FIDAP is able to predict the thermal stresses for the turbine blade. The reason for FIDAP under-predicting Bohn's data, is most likely because the material properties, in particular the temperature dependant properties, used in the two analyses were slightly different. Overall, the use of the CFD model using the solvers FLUENT and FIDAP to simulate the thermal stresses in a turbine blade has been justified. With the model correctly predicting the temperature and stress variation, and the locations of maximum stress intensity, its utilization to simulate turbine blade stresses for thermal shock loads and mission profiles are justified.

CHAPTER 5
TEST CASES – THERMAL SHOCK SIMULATIONS

The CFD model of a turbine blade was used to simulate five test cases. Each time varying load was simulated by defining a TRANSIENT BOUNDARY PROFILE (Appendix C), which was a text file containing data point pairs of time and temperature. The boundary profile was read into FLUENT and activated in the TOTAL TEMPERATURE field of the PRESSURE INLET boundary were the temperature value is assigned to all the nodes on that boundary. The minimum number of data points necessary to define the profile, for each case, assuming a piecewise linear fit, was used. This was done with the foresight that FLUENT linearly interpolates between the given data points to complete the profile.

An unsteady simulation was run, with the time range for the simulation set to that of the load. A text file of the temperature distribution for the pressure surface, suction surface and trailing edge was written. This was done at the times for which a FIDAP simulation was required. Each FIDAP simulation resulted in stress data at one time instant, with a series of these simulations being required to plot a time varying stress curve. An optimum number of FIDAP simulations, depending on the time range and steepness of the temperature changes, were done for each test case.

The loads for the test cases were drawn up to represent simplified versions of typical operation data. TIT data from a mission profile of a T56 engine was obtained from Glen Snedden at the CSIR. The T56 mission profile TIT data was used as the loading for the complex cycle. The shock load temperature peak and, rise and fall times was determined by the largest TIT spike and maximum TIT of the mission profile. The simplified cycle took the mission profile and simplified it into temperature rise to maximum, held at maximum temperature and then a temperature drop. The time scale for the simplified cycle was the same as the mission profile.

With only the TIT data for that mission profile available, and the PRESSURE INLET boundary requiring a TOTAL TEMPERATURE input, the transient profiles were read into FLUENT as total temperature. In doing so, the inlet and exit Mach numbers for the simulation were steady; therefore the flow features were relatively unchanged. Only the fluid temperature and blade surface temperature varied as the TIT changed. This resulted in the variation of the temperature and stress contours being the same as the validation exercise with only the range of magnitude changing. The locations of σ_e max also remained the same while only the magnitude varied with

TIT. For each test case, the maximum equivalent stress was plotted over the time range of the load.

5.1. Single Shock Load

The load was simulated as a thermal shock with the temperature increasing from 308 K to 1200 K in 30 s, and then returning to 308 K. The time of 30 s is representative of the largest shock in the mission profile, which occurs at start up. The maximum temperature of 1200 K was chosen to represents the worst possible TIT shock load that could be expected. Figure 5-1 gives the TIT and the variation of σ_e max. The locations on the blade, where the σ_e max occurs, are shown in figure E-6a in Appendix E.

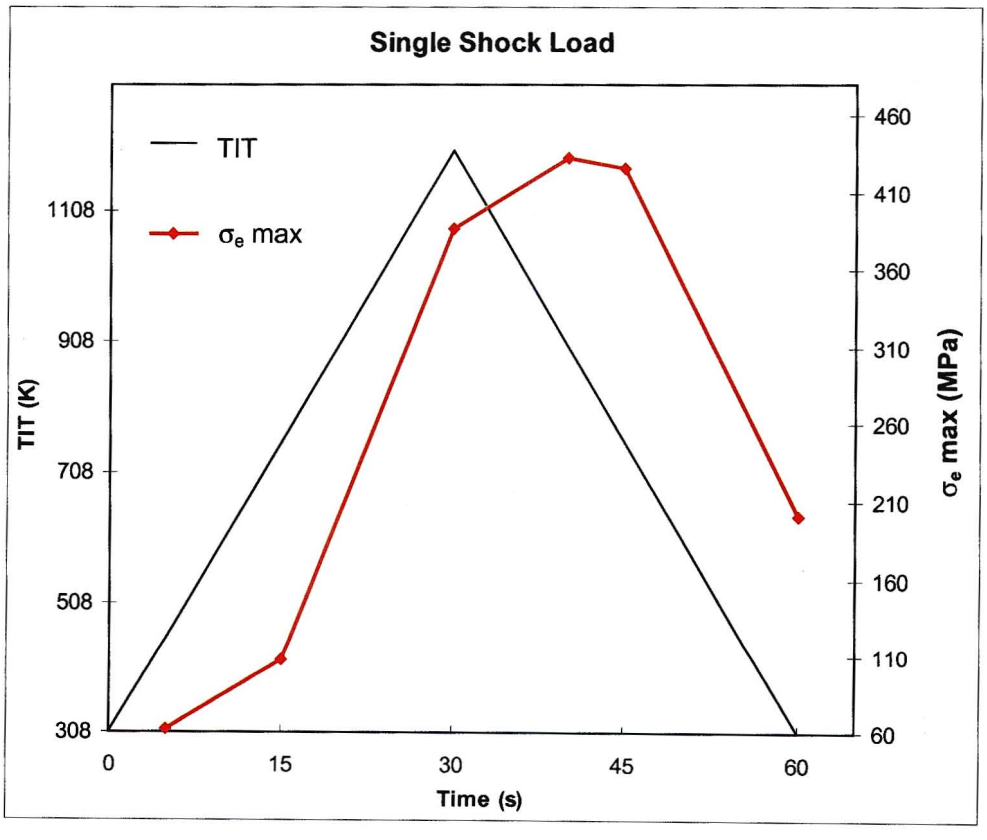

Figure 5-1: Maximum equivalent stress variation for the single shock load

The stress curves initially increases with a gentle gradient, which increases after a 100 K rise in TIT. The stress then rises sharply until TIT peaks and continues to increase but at a slower rate. The peak σ_e max of 433 MPa occurs after 40 s, decreases slowly up to 45 s then drops sharply as TIT decreases. The stress peak appears to lag the TIT peak, which is as a result of conduction. As TIT changes, the change has to be transmitted through the flow field to the blade

surface and then conducted through the blade. For the shock load simulated, the delay is about 15 s, which is one quarter of the load time or half the time to peak. The maximum σ_e max exceeds the material yield strength of 230 MPa after approximately 22 s (when TIT is 708 K) and drops below 230 MPa after 58 s (when TIT drop to 360 K).

For this test case, FIDAP simulations were done at more times than shown in the plot. The 6 data points shown in figure 5-1 are the minimum number of points required to accurately plot the σ_e max variation. The number of data points required to plot the stress had to be minimised so that only the necessary FIDAP simulations for the multiple shock test case, for which the time scale was 360 s, would be done.

5.2. Multiple Shock Loads

The multiple shock test case was simulated as a periodic series of single shocks. Figure 5-2 gives the σ_e max variation along with lines of peak and minimum σ_e max, and TIT. The rise and fall, and lag of σ_e max is consistent with the results for the single shock load. The peak σ_e max steadily increases with the maximum peak σ_e max corresponding to the third shock, i.e. after 165 s. The peak σ_e max then decreases for the fourth and fifth shocks and increases at the sixth shock. The minimum σ_e max shows a similar trend with and increase at the end of the first two shocks, decreases at the end of the third shock and then starts to increase at the end of the fourth and fifth shocks.

The data point at 360 s indicates that if the simulation was continued, the next point, which would be the minimum σ_e max at the end of the sixth shock, would have decreased from the minimum σ_e max value at 315 s. The line of peak σ_e max also indicates that the next peak σ_e max value would increase from the value at 345 s. The peak σ_e max appears to oscillate between 433 and 478 MPa and the minimum σ_e max between 178 and 212 MPa. After 22 s, σ_e max exceeds the material yield strength (230 MPa) and only drops below that limit for approximately a 30 s period after the end of each shock.

Generally, turbine blades are not expected to develop cracks from a single thermal shock application but from thermal fatigue due to cyclic stress loads. The stress gradients and locations of maximum stress, predicted by the CFD model, were shown to be accurate with respect to the data and therefore form a realistic and reliable input for thermal fatigue life calculations. The stress prediction for multiple shocks shows that the maximum stress (which

occurs between cooling holes 2 and 3 – see figure E-6a, Appendix E) is cyclic in nature, which was expected, but more importantly, the equivalent stress magnitude cycles from approximately 200 MPa (just below the material yield strength) to approximately 460 MPa, which is twice the material yield strength.

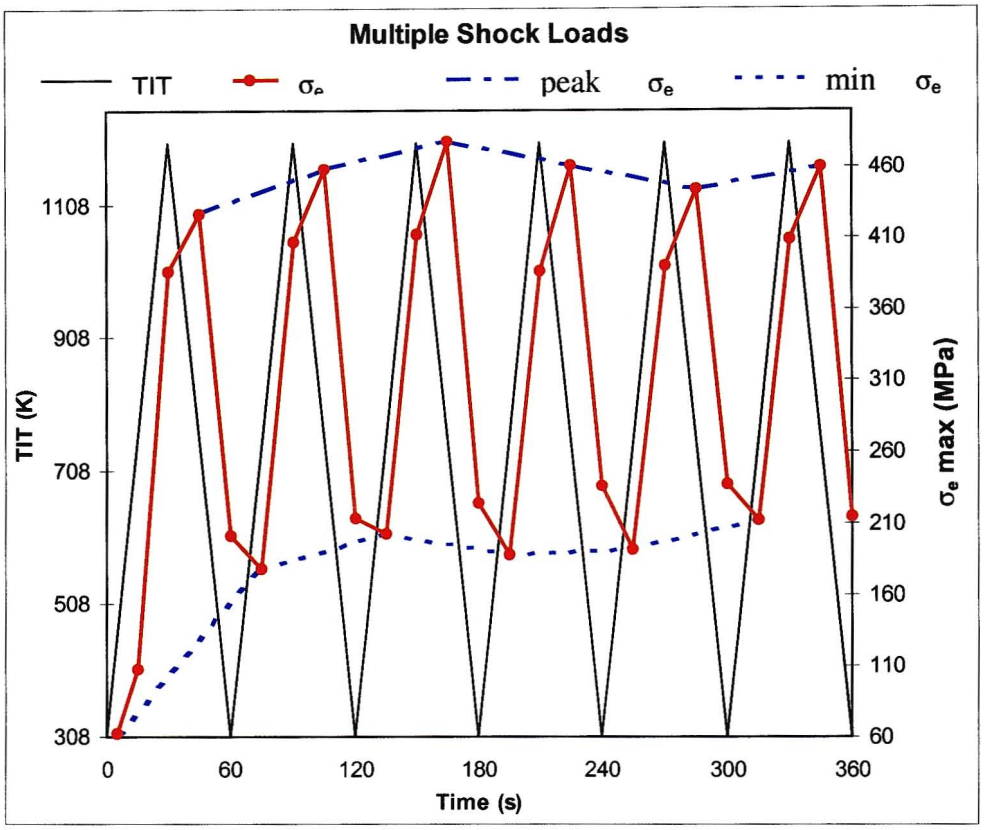

Figure 5-2: Maximum equivalent stress variation for multiple shock loads

From this, one would expect thermal fatigue cracks to develop in the critical region, i.e. between cooling holes 1 and 2, after some critical number of cycles. A simulation with this type of TIT loading condition could be used to determine the number of successive start-ups and shutdowns that would necessitate grounding the engine to replace the cracked turbine blades.

5.3. Simplified cycle

The T56 mission profile was simplified to a temperature rise from 308 K to 1349 K after 638 s, stays at 1349 K until 5425 s then returns to 308 K at 6047 s. The simplified cycle is shown in Figure 5-3 along with the σ_e max variation for the simplified cycle. The trends observed in the σ_e max variation for the single and multiple shock loads is seen here as well. The stress curve tracks the temperature increases more closely here than for the shock loads because of the

gentler gradient of the TIT. The stress curve gradient decreases after 638 s corresponding to the change in the TIT curve.

The stress still continues to rise (but rises slower) after the TIT has reached its maximum and then flattens after 1276 s. This again shows the lag due to conduction. The effect of the change in TIT that occurs after 638 s is only seen in the stress curve after 1276 s. Thereafter, the stress curve remains relatively flat until 5580 s when it decreases tracking the TIT curve very closely. The change in the stress curve occurs 155 s after the change in the TIT curve; again the lag due to conduction is evident.

The σ_e max curve goes above 230 MPa after 300 s when TIT reaches 560 K. It then reaches 800 MPa after 1276 s and increases very slowly to 817 MPa after 5580 s. σ_e max only drops below 230 MPa again after 6000 s. The simulations thus far show that σ_e max follows TIT changes but lags because of conduction in the blade. A steep change in TIT (such as the shock load) will show up much later on the stress curve than a gentler change.

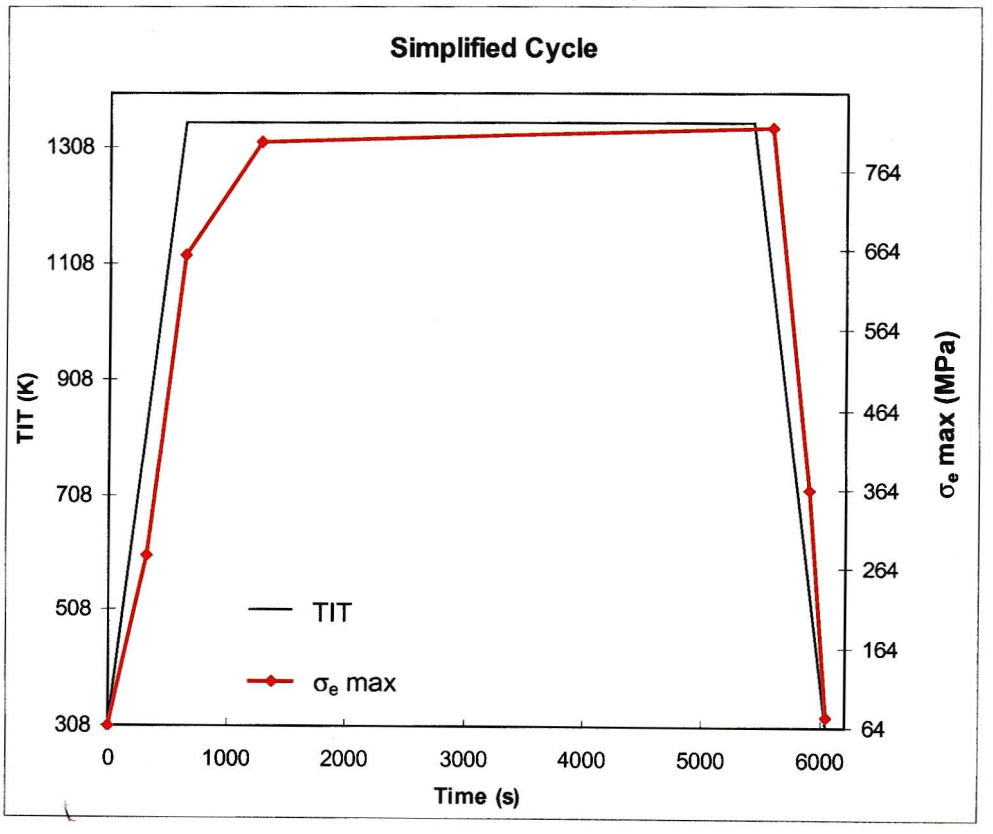

Figure 5-3: Maximum equivalent stress variation for the simplified cycle

5.4. Multiple Cycles

The simplified cycle was periodically repeated to simulate the multiple cycles test case. The σ_e max variation (figure 5-4) displayed the same features for each cycle and showed similar trends for the peak and minimum σ_e max that was seen for the multiple shock load case. The peak σ_e max remains relatively constant with 817 MPa for cycle 1, 815 MPa for cycle 2 and 816 MPa for cycle 3. The minimum σ_e max increases from 78 MPa at 6047 s to 89 MPa at 12094s and then drops to 51 MPa at 18141 s. These values are expected to stay within the same range for any number of cycles.

For the simplified cycle and multiple cycles, the regions of the graph that contribute to thermal fatigue would be the rise and fall of TIT and thermal stress. For the time between 1276 and 5580 s, the maximum stress is almost constant. If one takes the simplified cycle to represent a mission profile, a simulation with multiple cycles would represent multiple missions. Thus, the maximum stress variation predicted by the CFD model for multiple cycles would be inputted into a thermal fatigue life calculation and one can determine the number missions after which thermal fatigue cracks in the blade will develop.

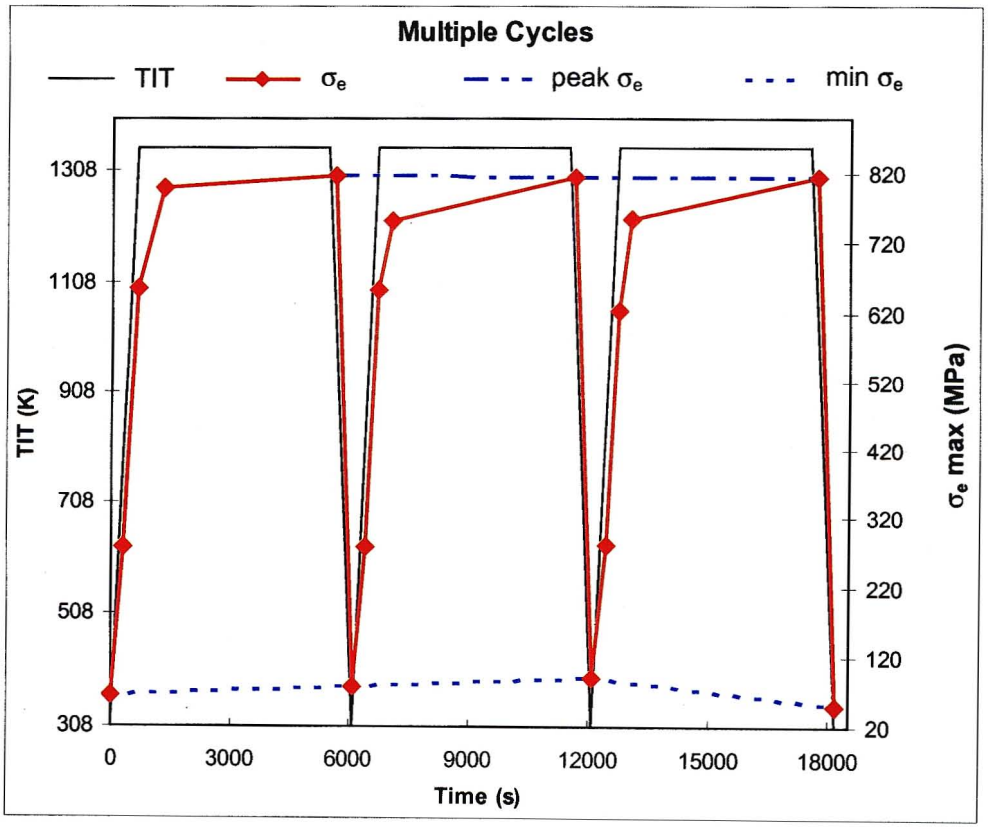

Figure 5-4: Maximum equivalent stress variation for multiple cycles

5.5. Complex Cycle

The complex cycle had to represent typical operational data; therefore the T56 mission profile TIT data was used as the loading for the simulation. The TIT (figure 5-5) profile contains a range of features from temperature spikes to gentle changes in temperature; which were simulated in the first four test cases. This gives one some foresight into what the stress curve is expected to do. The stress variation for the complex cycle (figure 5-5) clearly shows that the maximum stress tracks TIT. The stress curve undergoes a change in gradient corresponding to the change in TIT after 30 s. The first temperature spike at 450 s is almost instantaneous which to too quick to affect the stress curve. The same feature is seen at the second spike (636 s).

The stress curve does rise sharply to 656 MPa after the second spike but the delay is evident. The TIT levels off after the spike, which causes the σ_e max to level off also. Between 1372 s and 2672 s, when TIT is slowly decreasing, σ_e max slowly increases from 785 MPa to its peak value of 818 MPa. Thereafter, TIT decreases which causes σ_e max to also decrease. The spikes that occur around 5424 s are too small and too sharp to affect σ_e max, hence the continued steady decrease in σ_e max.

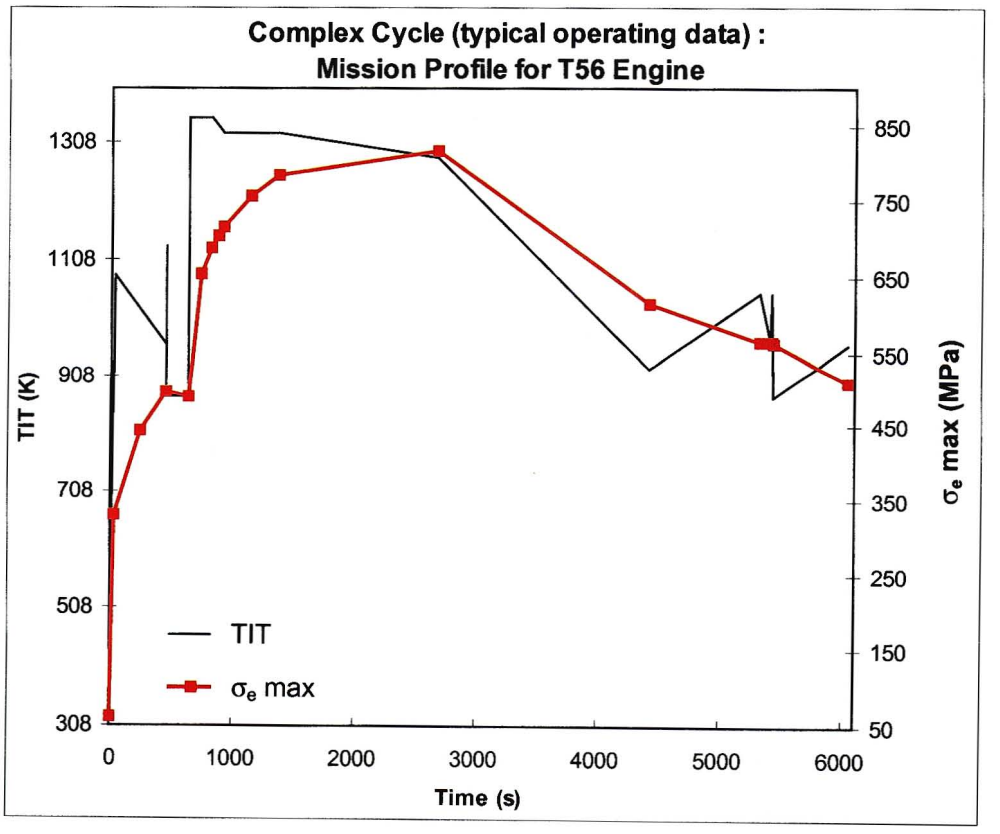

Figure 5-5: Maximum equivalent stress variation for the complex cycle

The material yield strength in exceeded after 22 s and remains above 230 MPa for the duration of the mission. The σ_e max (figure 5-5) appears to be proportional to temperature, and was plotted against TIT (red curve in figure 5-6) in an attempt to approximate σ_e max as a function of TIT. The variation of the points made it impossible to do a curve fit, which would have approximated σ_e max as a function of TIT. The region between 300 K and 900 K, which represented the first large spike in TIT (i.e. during start up), was the part of the stress variation that did not coincide with the fitted curve.

The stress curve was separated into two portions – start up and after start up. A linear fit was done for lines of max and min σ_e max in the start up region (Eqs F-1 and 5-2, Appendix F), and a 4^{th} order polynomial fit was used for the lines of max and min σ_e max over the rest of the stress curve (Eqs F-3 and F-4). The fitted curves for the maximum and minimum σ_e max are shown in figure 5-6. Using Eqs F-1 to F-5 allows one to approximate a maximum and minimum σ_e max variation for a given TIT profile, and then compute the mean σ_e max (Eq F-5), also shown in figure 5-6, as an approximate function of TIT only. Figure 5-7 shows that the mean σ_e max computed using Eqs F-1 to F-6 provides a good approximation of the thermal stress variation for the given mission profile.

The method using Eqs F-1 to F-5 can be used to get an approximate solution of the maximum stress variation for the turbine blade needing only the TIT profile from the mission to do so. This significantly reduces the computational effort in determining the maximum thermal stress variation. From the maintenance perspective, the method would quickly and easily provide an accurate enough approximation of the thermal stress variation to use in fatigue life calculations. For a more accurate thermal stress variation, for the purposes of fatigue life calculations, one must invest more effort by using the CFD model to predict the stress variation.

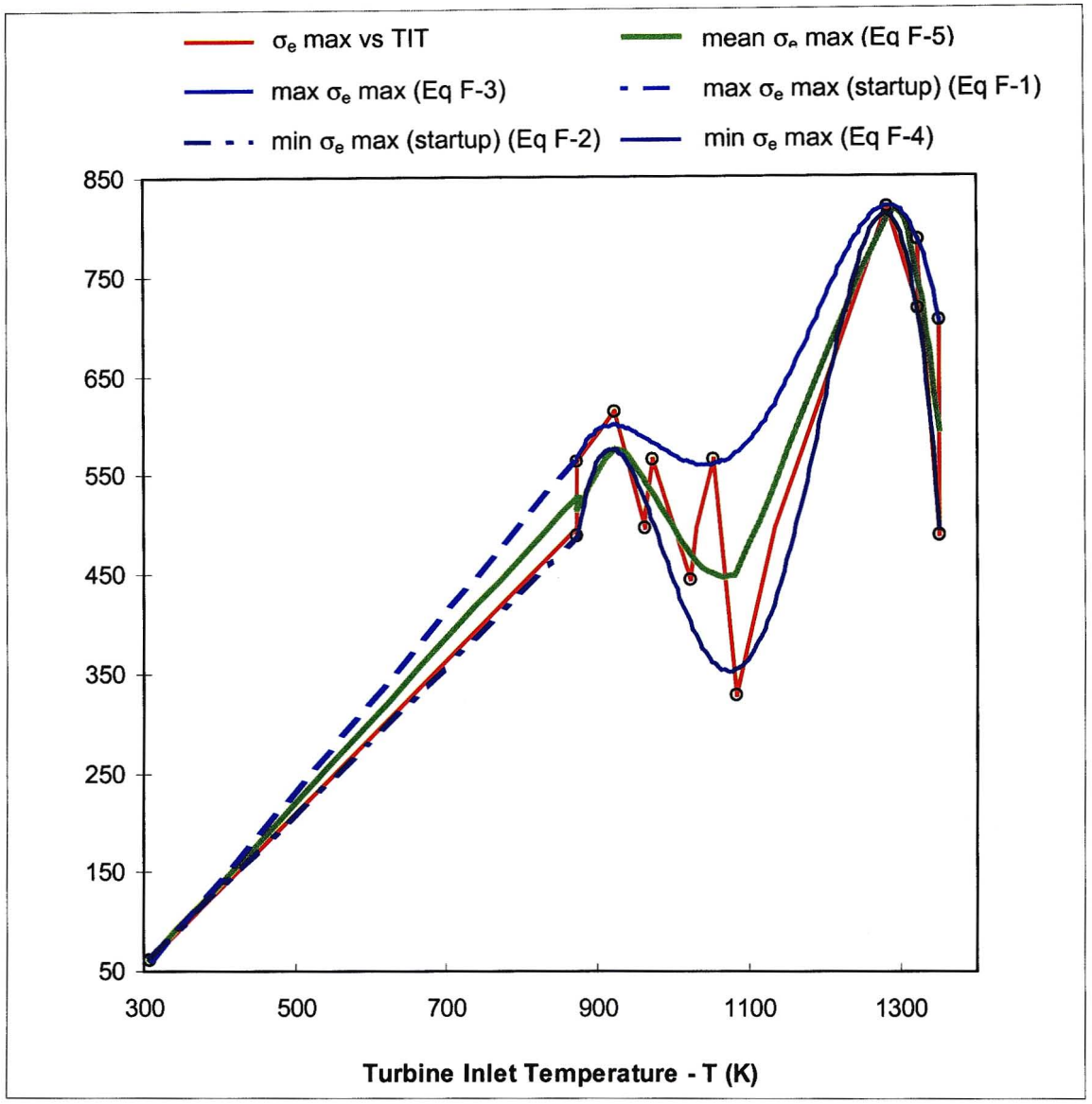

Figure 5-6: Maximum equivalent stress for the complex cycle plotted against TIT with the peak and min σ_e max computed using Eqs F-1 to 5-4 and the mean σ_e max computed using Eq F-5

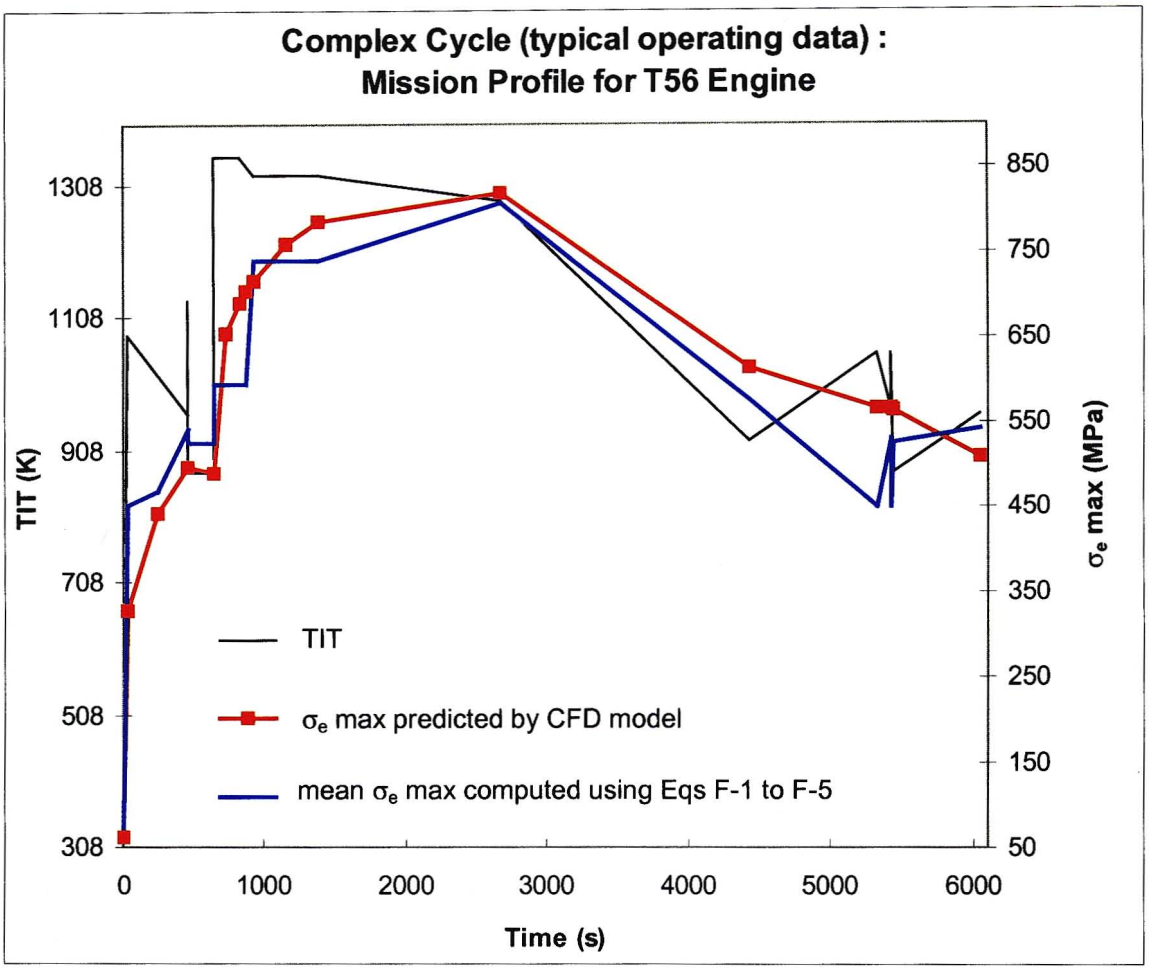

Figure 5-7: Maximum equivalent stress variation predicted by the CFD model and computed using Eqs F-1 to F-5 in Appendix F

CHAPTER 6
CONCLUSION AND RECOMMENDATIONS

6.1. Overview

Thermal fatigue of internally cooled turbine blades is an industry wide problem that to date has been difficult to quantify. With the industry pushing towards increased TIT for improved engine performance, blade cooling has become increasingly important. A consequence of internal cooling is that temperature gradients exist within the blade causing thermal stresses. The intricate cooling passages have to be designed to ensure that the thermal stresses during operation do not exceed the blade material strength limit. During operation however, the engines TIT continually rises and falls causing the thermal stresses to cycle which leads to thermal fatigue.

An intricate, quantitative understanding of thermal stress behaviour during operation is necessary in order to achieve accurate thermal fatigue life calculations. The work reported in this dissertation attempted to use numerical prediction tools to simulate the thermal stress behaviour during engine operation. Numerical predictions enable researchers to visualise physical effects within the engine components that are difficult to obtain experimentally thereby providing improved understanding of the effects. Accurate and realistic numerical modelling of turbine engine flows with all its intricacies and complexities is by no means a trivial task.

Simulating turbine blade thermal stresses is even more computational intensive in that it requires both flow and structural analyses for the blade. Presently, fluid and structural analyses using numerical codes are performed separately because of the different formulations for the governing equations. Fluid solvers use a Finite Volume formulation and structural solvers a Finite Element formulation. For the present study, the commercially available CFD code, FLUENT and FEM code, FIDAP were used to model the problem. The two solutions have to be coupled in some way which is achieved, for the given problem, through the blade surface temperature. The CFD codes must be capable of accurately resolving the flow field to obtain a realistic surface temperature distribution, which is at the least spatially non-uniform. This is then interpolated into the FEM code for the thermal analysis which yields the thermal stress distribution.

The combined CFD / FEM model of the turbine blade was used to simulate a validation case, the data for which was taken from the open literature. Validation of the model is important as it provides and understanding of the model's performance. This was very necessary since no comparative data was available for the engine mission profile simulation. A further set of simple unsteady test cases were simulated prior to the engine data being simulated to access the consistency of the model's unsteady predictions. The predicted thermal stress profile for the engine mission profile was used to draw up a loose correlation between TIT and maximum blade thermal stress. A curve fit was used to achieve this. The purpose of the correlation is that it provides a quick approximation the maximum thermal stress variation in the blade.

6.2. CFD Model of a Turbine Blade

The combined aerodynamic and thermal analysis using FLUENT and FIDAP was in fair agreement with the combined aerodynamic and thermal analysis of Bohn et. al. (1995). The computational grid was fine enough to produce mesh independent velocity and pressure fields that were in excellent agreement with the data. The Realizable k-ε turbulence model with enhanced wall treatment for the viscous affected near-wall region provided adequate closure of the governing RANS equations and at the least, qualitatively predicted the heat transfer coefficient and surface temperature trends. The surface heat transfer coefficient and temperature distribution were over-predicted for the first 50 % axial chord on both pressure and suction surfaces, but the predicted trends were consistent with the data.

The computational grid used in the viscous affected, near-wall region, was fine enough to extend the validity of the compressible Navier-Stokes equations all the way to the wall. In doing so, it was expected that full agreement with data was unlikely, but showed that full Navier-Stokes solutions for heat transfer is almost a reality. The predicted internal blade temperature profile was in excellent agreement with the data, and the predicted thermal stress profile was also in good agreement. The thermal stress contour trends were correctly predicted but the stress magnitudes under-predicted the data. The validation exercise showed that the CFD model was capable of predicting the thermal stresses in a turbine blade for a steady inlet flow condition. An additional validation exercise using a long cylinder showed that the FEM code, FIDAP, was capable of predicted thermal stresses with unsteady internal temperature profiles.

6.3. Thermal Shock Simulations

The predicted trends for the test cases were both expected and consistent with the validation exercises. The simulation of the mission profile showed that largest jump in thermal stress - 'thermal shock' - occurs during startup. During the mission, the TIT does not vary by large amounts; therefore the stresses do not change sharply. The main concern would be thermal fatigue from the cyclic thermal stress profile (i.e. startup and shut down) resulting from the engine repeatedly going through the same mission profile. The predict thermal stresses from the CFD model provides a realistic boundary condition for a thermal fatigue calculations, which would be used to determine the critical number of cycles after which thermal fatigue cracks will reach a dangerous level warranting replacement.

From the predicted thermal stress profile, the author was to develop a loose polynomial that approximates the thermal stress profile as a function of TIT. The thermal stress profile for the mission profile, calculated using the polynomial approximation was in very good agreement with the predicted thermal stresses.

6.4. Recommendations for Future work

The validation of the model should be confirmed with a well-defined set of data. The data set should contain fully defined flow boundary conditions, and a full set of material and thermal parameters. Refining the boundary layer mesh in the critical leading edge and shock regions must be addressed to improve the heat transfer prediction in these regions. The results of the thermal shock simulations were as expected but these must be validated with experimental data. The simulations would be more realistic if more realistic unsteady boundary conditions, i.e. unsteady pressure or velocity profile as well as unsteady temperature profile, were available for the aerodynamic analysis.

Thereafter, the CFD model should be extended to 3-D, the test cases re-simulated, and the predictions compared with 3-D experimental data. This step-by-step progression of model development can continue until a multistage turbine can be simulated. The main limitation for such a simulation is availability of sufficient computational power. Each improvement to the CFD model will lead more accurate and realistic thermal fatigue calculations.

APPENDIX A

Thermodynamic equations for a gas turbine engine (see figure 1-2)

Temperature at compressor entry:

$$T_2 = T_1 + \frac{V_1^2}{2Cp} \qquad \text{Eq A-1}$$

Pressure at compressor entry:

$$\frac{p_2}{p_1} = \left(\frac{T_2}{T_1}\right)^{\frac{\gamma \eta_c}{\gamma - 1}} \qquad \text{Eq A-2}$$

Since $w_t = w_c$, temperature at compressor exit is calculated from:

$$T_3 - T_2 = T_4 - T_5 \qquad \text{Eq A-3}$$

Temperature at combustor exit:

$$T_4 = T_3 + \frac{q_{in}}{Cp} \qquad \text{Eq A-4}$$

Pressure drop through turbine:

$$\frac{p_4}{p_5} = \left(\frac{T_4}{T_5}\right)^{\frac{\gamma}{(\gamma-1)\eta_t}} \qquad \text{Eq A-5}$$

Temperature at nozzle exit:

$$T_6 = T_5\left(\frac{p_6}{p_5}\right)^{\frac{(\gamma-1)\eta_n}{\gamma}} \qquad \text{Eq A-6}$$

Speed at nozzle exit:

$$V_6 = \sqrt{2Cp(T_5 - T_6)} \qquad \text{Eq A-7}$$

Mass flow rate calculated at nozzle exit:

$$\dot{m} = \rho_6 A_6 V_6 \qquad \text{Eq A-8}$$

Thermal efficiency of the engine:

$$\eta_{th} = \frac{(V_6 - V_1)V_1}{q_{in}} \qquad \text{Eq A-9}$$

Propulsion efficiency:

$$\eta_p = \frac{2}{1+\frac{V_6}{V_1}} \qquad \text{Eq A-10}$$

The symbols and subscripts in Eqs A-1 to A-10 are explained below:

Symbols

T = Temperature

p = Pressure

V = Speed

η = Efficiency

Cp = Specific heat

q_{in} = Heat input

$\dot{m}$ = Mass flow rate

γ = Specific heat ratio

Subscripts

1 to 6 = Position in the engine with reference to figure 1-2

c = compressor

t = turbine

n = nozzle

APPENDIX B

Property	Symbol	Constant value
Density	ρ	7832.7 kg/m^3
Specific Heat	Cp	487 J/kgK
Thermal Conductivity coefficient	k	56.7 W/m^{2}K
Thermal Expansion coefficient	α	1.08 E –05 m/mK
Young's Modulus	E	2.005 E 10 GPa
Poisson's ratio	ν	0.32

Table B-1: Properties of plain carbon steel

Property	Symbol	Constant value / Function of Temperature
Density	ρ	8000 kg/m^3
Specific Heat	Cp	500 J/kgK
Thermal Conductivity coefficient	k	16 W/m^{2}K
Thermal Expansion coefficient	α	5.008E-12T^2-3.4142E-9T+1.6477E-5 [m/mK]
Young's Modulus	E	-9.5588E-2T+2.4301E2 [GPa]
Poisson's ratio	ν	0.3

Table B-2: Properties of ASTM 310 stainless steel

APPENDIX C

Boundary profile for single shock simulation:

```
((singleshock transient 3 0)
(time
0
30
60
)
(total-temperature
308.15
1200
308.15
)
)
```

Boundary profile for multiple shocks simulation:

```
((multipleshock transient 3 1)
(time
0
30
60
)
(total-temperature
308.15
1200
308.15
)
)
```

Boundary profile for simplified cycle simulation:

((simplecycle transient 4 0)
(time
0
638
5425
6047
)
(total-temperature
308.15
1349
1349
308.15
)
)

Boundary profile for multiple cycles simulation:

((multiplecycles transient 4 1)
(time
0
638
5425
6047
)
(total-temperature
308.15
1349
1349
308.15
)
)

Boundary profile for complex cycle simulation:

((complexcycle transient 18 0)
(time
0
30
450
451
456
636
638
822
922
1372
2672
4427
5322
5414
5424
5439
6039
6047
)
(total-temperature
308.15
1083.15
963.15
1133.15
873.15
873.15
1349.9
1349.9
1322
1322
1283.15
923.15
1053.15
973.15
1053.15

873.15
963.15
963.15
)
)

APPENDIX D

Sample FIPREP file for test case simulations:

```
/
/  INPUT FILE CREATED ON 10 Jul 02 AT  13:12:54
/
/
/ ***  FICONV Conversion Commands ***
/ ***  Remove / to uncomment as needed
/
/  FICONV(NEUTRAL,NORESULTS,INPUT)
/  INPUT(FILE= "blade.FDNEUT")
/  END
/  *** of FICONV Conversion Commands
/
TITLE

/
/ ***  FIPREP  Commands ***
/
FIPREP
 PROB (2-D, STEA, NONL, NOMO, ENER, STRU, NORE)
 EXEC (NEWJ)
 SOLU (SEGR = 200, MESH = 10, SURF = 0.100000000000E-05)
 DATA (CONT)
 STRU (NOLA, NOUN, STNP, THER)
 PRIN (NONE)
 SCAL (VALU = 0.100000000000E-01)
 ENTI (NAME = "blade", DEFO, PROP = "blade")
 ENTI (NAME = "suction surface", PLOT)
 ENTI (NAME = "pressure surface", PLOT)
 ENTI (NAME = "trailing edge", PLOT)
 ENTI (NAME = "hole1", CONV, PROP = "hole1")
 ENTI (NAME = "hole2", CONV, PROP = "hole2")
 ENTI (NAME = "hole3", CONV, PROP = "hole3")
 ENTI (NAME = "hole4", CONV, PROP = "hole4")
```

```
ENTI (NAME = "hole5", CONV, PROP = "hole5")
ENTI (NAME = "hole6", CONV, PROP = "hole6")
ENTI (NAME = "hole7", CONV, PROP = "hole7")
ENTI (NAME = "hole8", CONV, PROP = "hole8")
ENTI (NAME = "hole9", CONV, PROP = "hole9")
ENTI (NAME = "hole10", CONV, PROP = "hole10")
DENS (SET = "blade", CONS = 8000.0)
SPEC (SET = "blade", CONS = 500.0)
COND (SET = "blade", CONS = 16.0)
VOLU (SET = "blade", CURV = 8, REFT = 488.0)
  0.2730000000E+03,  0.3730000000E+03,  0.4730000000E+03,  0.5730000000E+03,
  0.6730000000E+03,  0.7730000000E+03,  0.8730000000E+03,  0.9730000000E+03,
  0.1591800000E-04,  0.1590000000E-04,  0.1598200000E-04,  0.1616400000E-04,
  0.1644600000E-04,  0.1682800000E-04,  0.1731100000E-04,  0.1789300000E-04
HTRA (SET = "hole1", CONS = 1943.67, REFT = 336.39)
HTRA (SET = "hole2", CONS = 1881.45, REFT = 326.68)
HTRA (SET = "hole3", CONS = 1893.49, REFT = 332.68)
HTRA (SET = "hole4", CONS = 1960.62, REFT = 338.86)
HTRA (SET = "hole5", CONS = 1850.77, REFT = 318.95)
HTRA (SET = "hole6", CONS = 1813.36, REFT = 315.58)
HTRA (SET = "hole7", CONS = 1871.88, REFT = 326.26)
HTRA (SET = "hole8", CONS = 2643.07, REFT = 359.83)
HTRA (SET = "hole9", CONS = 1809.89, REFT = 360.89)
HTRA (SET = "hole10", CONS = 3056.69, REFT = 414.85)
YOUN (SET = "blade", CURV = 2, TEMP)
  0.2930000000E+03,  0.9730000000E+03,  0.2150000000E+12,  0.1500000000E+12
POIS (SET = "blade", CONS = 0.3)
BCNO (TEMP, NODE = 1, CONS = 551.48)
BCNO (TEMP, NODE = 2, CONS = 523.095)
BCNO (TEMP, NODE = 3, CONS = 550.669)
BCNO (TEMP, NODE = 4, CONS = 549.858)
BCNO (TEMP, NODE = 5, CONS = 549.047)
BCNO (TEMP, NODE = 6, CONS = 548.236)
BCNO (TEMP, NODE = 7, CONS = 547.425)
BCNO (TEMP, NODE = 8, CONS = 546.614)
BCNO (TEMP, NODE = 9, CONS = 545.803)
BCNO (TEMP, NODE = 10, CONS = 544.992)
BCNO (TEMP, NODE = 11, CONS = 544.181)
BCNO (TEMP, NODE = 12, CONS = 543.37)
BCNO (TEMP, NODE = 13, CONS = 542.559)
```

BCNO (TEMP, NODE = 14, CONS = 541.748)
BCNO (TEMP, NODE = 15, CONS = 540.937)
BCNO (TEMP, NODE = 16, CONS = 540.126)
BCNO (TEMP, NODE = 17, CONS = 539.315)
BCNO (TEMP, NODE = 18, CONS = 538.504)
BCNO (TEMP, NODE = 19, CONS = 537.693)
BCNO (TEMP, NODE = 20, CONS = 536.882)
BCNO (TEMP, NODE = 21, CONS = 535.26)
BCNO (TEMP, NODE = 22, CONS = 531.205)
BCNO (TEMP, NODE = 22, CONS = 531.205)
BCNO (TEMP, NODE = 23, CONS = 527.15)
BCNO (TEMP, NODE = 24, CONS = 527.15)
BCNO (TEMP, NODE = 25, CONS = 527.15)
BCNO (TEMP, NODE = 26, CONS = 509.308)
BCNO (TEMP, NODE = 27, CONS = 519.04)
BCNO (TEMP, NODE = 28, CONS = 514.985)
BCNO (TEMP, NODE = 29, CONS = 510.119)
BCNO (TEMP, NODE = 31, CONS = 660.5595)
BCNO (TEMP, NODE = 32, CONS = 508.497)
BCNO (TEMP, NODE = 33, CONS = 507.686)
BCNO (TEMP, NODE = 34, CONS = 507.686)
BCNO (TEMP, NODE = 35, CONS = 507.686)
BCNO (TEMP, NODE = 36, CONS = 506.875)
BCNO (TEMP, NODE = 37, CONS = 506.875)
BCNO (TEMP, NODE = 38, CONS = 506.875)
BCNO (TEMP, NODE = 39, CONS = 506.064)
BCNO (TEMP, NODE = 40, CONS = 506.064)
BCNO (TEMP, NODE = 41, CONS = 506.064)
BCNO (TEMP, NODE = 42, CONS = 504.442)
BCNO (TEMP, NODE = 43, CONS = 501.198)
BCNO (TEMP, NODE = 44, CONS = 497.954)
BCNO (TEMP, NODE = 45, CONS = 496.332)
BCNO (TEMP, NODE = 46, CONS = 494.71)
BCNO (TEMP, NODE = 47, CONS = 493.899)
BCNO (TEMP, NODE = 48, CONS = 493.088)
BCNO (TEMP, NODE = 49, CONS = 490.655)
BCNO (TEMP, NODE = 50, CONS = 489.844)
BCNO (TEMP, NODE = 51, CONS = 489.033)
BCNO (TEMP, NODE = 52, CONS = 488.222)
BCNO (TEMP, NODE = 53, CONS = 487.411)

BCNO (TEMP, NODE = 54, CONS = 486.6)
BCNO (TEMP, NODE = 55, CONS = 482.545)
BCNO (TEMP, NODE = 56, CONS = 478.49)
BCNO (TEMP, NODE = 57, CONS = 474.435)
BCNO (TEMP, NODE = 58, CONS = 470.38)
BCNO (TEMP, NODE = 59, CONS = 466.325)
BCNO (TEMP, NODE = 60, CONS = 462.27)
BCNO (TEMP, NODE = 61, CONS = 466.325)
BCNO (TEMP, NODE = 62, CONS = 470.38)
BCNO (TEMP, NODE = 63, CONS = 474.435)
BCNO (TEMP, NODE = 64, CONS = 478.49)
BCNO (TEMP, NODE = 65, CONS = 482.545)
BCNO (TEMP, NODE = 66, CONS = 486.6)
BCNO (TEMP, NODE = 67, CONS = 490.655)
BCNO (TEMP, NODE = 68, CONS = 494.71)
BCNO (TEMP, NODE = 69, CONS = 498.765)
BCNO (TEMP, NODE = 70, CONS = 502.82)
BCNO (TEMP, NODE = 71, CONS = 506.875)
BCNO (TEMP, NODE = 72, CONS = 510.93)
BCNO (TEMP, NODE = 73, CONS = 514.985)
BCNO (TEMP, NODE = 74, CONS = 519.04)
BCNO (TEMP, NODE = 75, CONS = 523.095)
BCNO (TEMP, NODE = 76, CONS = 527.15)
BCNO (TEMP, NODE = 77, CONS = 531.205)
BCNO (TEMP, NODE = 78, CONS = 535.26)
BCNO (TEMP, NODE = 79, CONS = 539.315)
BCNO (TEMP, NODE = 80, CONS = 543.37)
BCNO (TEMP, NODE = 81, CONS = 547.425)
BCNO (TEMP, NODE = 82, CONS = 551.48)
BCNO (TEMP, NODE = 83, CONS = 555.535)
BCNO (TEMP, NODE = 84, CONS = 559.59)
BCNO (TEMP, NODE = 85, CONS = 560.401)
BCNO (TEMP, NODE = 86, CONS = 561.212)
BCNO (TEMP, NODE = 87, CONS = 562.023)
BCNO (TEMP, NODE = 88, CONS = 562.834)
BCNO (TEMP, NODE = 89, CONS = 563.645)
BCNO (TEMP, NODE = 90, CONS = 564.456)
BCNO (TEMP, NODE = 91, CONS = 565.267)
BCNO (TEMP, NODE = 92, CONS = 566.078)
BCNO (TEMP, NODE = 93, CONS = 566.889)

BCNO (TEMP, NODE = 94, CONS = 566.078)
BCNO (TEMP, NODE = 95, CONS = 565.267)
BCNO (TEMP, NODE = 96, CONS = 564.456)
BCNO (TEMP, NODE = 97, CONS = 563.645)
BCNO (TEMP, NODE = 98, CONS = 562.834)
BCNO (TEMP, NODE = 99, CONS = 562.023)
BCNO (TEMP, NODE = 100, CONS = 561.212)
BCNO (TEMP, NODE = 101, CONS = 560.401)
BCNO (TEMP, NODE = 102, CONS = 559.59)
BCNO (TEMP, NODE = 103, CONS = 558.779)
BCNO (TEMP, NODE = 104, CONS = 557.968)
BCNO (TEMP, NODE = 105, CONS = 557.157)
BCNO (TEMP, NODE = 106, CONS = 556.346)
BCNO (TEMP, NODE = 107, CONS = 555.535)
BCNO (TEMP, NODE = 108, CONS = 554.724)
BCNO (TEMP, NODE = 109, CONS = 553.913)
BCNO (TEMP, NODE = 110, CONS = 553.102)
BCNO (TEMP, NODE = 111, CONS = 552.291)
BCNO (TEMP, NODE = 112, CONS = 551.48)
BCNO (TEMP, NODE = 113, CONS = 550.669)
BCNO (TEMP, NODE = 114, CONS = 549.858)
BCNO (TEMP, NODE = 115, CONS = 549.047)
BCNO (TEMP, NODE = 116, CONS = 550.669)
BCNO (TEMP, NODE = 117, CONS = 551.48)
BCNO (TEMP, NODE = 118, CONS = 551.48)
BCNO (TEMP, NODE = 119, CONS = 551.48)
BCNO (TEMP, NODE = 120, CONS = 551.48)
BCNO (TEMP, NODE = 121, CONS = 547.425)
BCNO (TEMP, NODE = 122, CONS = 543.37)
BCNO (TEMP, NODE = 123, CONS = 539.315)
BCNO (TEMP, NODE = 124, CONS = 535.26)
BCNO (TEMP, NODE = 125, CONS = 531.205)
BCNO (TEMP, NODE = 126, CONS = 532.4215)
BCNO (TEMP, NODE = 127, CONS = 533.638)
BCNO (TEMP, NODE = 128, CONS = 534.8545)
BCNO (TEMP, NODE = 129, CONS = 536.071)
BCNO (TEMP, NODE = 130, CONS = 537.2875)
BCNO (TEMP, NODE = 131, CONS = 538.504)
BCNO (TEMP, NODE = 132, CONS = 539.7205)
BCNO (TEMP, NODE = 133, CONS = 540.937)

BCNO (TEMP, NODE = 134, CONS = 542.1535)
BCNO (TEMP, NODE = 135, CONS = 543.37)
BCNO (TEMP, NODE = 136, CONS = 544.5865)
BCNO (TEMP, NODE = 137, CONS = 545.803)
BCNO (TEMP, NODE = 138, CONS = 547.0195)
BCNO (TEMP, NODE = 139, CONS = 548.236)
BCNO (TEMP, NODE = 140, CONS = 549.4525)
BCNO (TEMP, NODE = 141, CONS = 550.669)
BCNO (TEMP, NODE = 142, CONS = 551.8855)
BCNO (TEMP, NODE = 143, CONS = 553.102)
BCNO (TEMP, NODE = 144, CONS = 554.3185)
BCNO (TEMP, NODE = 145, CONS = 555.535)
BCNO (TEMP, NODE = 146, CONS = 556.7515)
BCNO (TEMP, NODE = 147, CONS = 557.968)
BCNO (TEMP, NODE = 148, CONS = 559.1845)
BCNO (TEMP, NODE = 149, CONS = 560.401)
BCNO (TEMP, NODE = 150, CONS = 561.6175)
BCNO (TEMP, NODE = 151, CONS = 562.834)
BCNO (TEMP, NODE = 152, CONS = 564.0505)
BCNO (TEMP, NODE = 153, CONS = 565.267)
BCNO (TEMP, NODE = 154, CONS = 566.4835)
BCNO (TEMP, NODE = 155, CONS = 567.7)
BCNO (TEMP, NODE = 156, CONS = 568.9165)
BCNO (TEMP, NODE = 157, CONS = 570.133)
BCNO (TEMP, NODE = 158, CONS = 571.3495)
BCNO (TEMP, NODE = 159, CONS = 572.566)
BCNO (TEMP, NODE = 160, CONS = 573.7825)
BCNO (TEMP, NODE = 161, CONS = 574.999)
BCNO (TEMP, NODE = 162, CONS = 576.2155)
BCNO (TEMP, NODE = 163, CONS = 577.432)
BCNO (TEMP, NODE = 164, CONS = 578.6485)
BCNO (TEMP, NODE = 165, CONS = 579.865)
BCNO (TEMP, NODE = 166, CONS = 581.0815)
BCNO (TEMP, NODE = 167, CONS = 582.298)
BCNO (TEMP, NODE = 168, CONS = 583.5145)
BCNO (TEMP, NODE = 169, CONS = 584.731)
BCNO (TEMP, NODE = 170, CONS = 585.9475)
BCNO (TEMP, NODE = 171, CONS = 587.164)
BCNO (TEMP, NODE = 172, CONS = 588.3805)
BCNO (TEMP, NODE = 173, CONS = 589.597)

BCNO (TEMP, NODE = 174, CONS = 590.8135)
BCNO (TEMP, NODE = 175, CONS = 592.03)
BCNO (TEMP, NODE = 176, CONS = 593.2465)
BCNO (TEMP, NODE = 177, CONS = 594.463)
BCNO (TEMP, NODE = 178, CONS = 595.6795)
BCNO (TEMP, NODE = 179, CONS = 596.896)
BCNO (TEMP, NODE = 180, CONS = 598.1125)
BCNO (TEMP, NODE = 181, CONS = 599.329)
BCNO (TEMP, NODE = 182, CONS = 600.5455)
BCNO (TEMP, NODE = 183, CONS = 601.762)
BCNO (TEMP, NODE = 184, CONS = 602.9785)
BCNO (TEMP, NODE = 185, CONS = 604.195)
BCNO (TEMP, NODE = 186, CONS = 605.4115)
BCNO (TEMP, NODE = 187, CONS = 606.2225)
BCNO (TEMP, NODE = 188, CONS = 607.0335)
BCNO (TEMP, NODE = 189, CONS = 607.8445)
BCNO (TEMP, NODE = 190, CONS = 608.6555)
BCNO (TEMP, NODE = 191, CONS = 611.8995)
BCNO (TEMP, NODE = 192, CONS = 615.1435)
BCNO (TEMP, NODE = 193, CONS = 618.3875)
BCNO (TEMP, NODE = 194, CONS = 621.6315)
BCNO (TEMP, NODE = 195, CONS = 624.8755)
BCNO (TEMP, NODE = 196, CONS = 628.1195)
BCNO (TEMP, NODE = 197, CONS = 631.3635)
BCNO (TEMP, NODE = 198, CONS = 634.6075)
BCNO (TEMP, NODE = 199, CONS = 637.8515)
BCNO (TEMP, NODE = 200, CONS = 641.0955)
BCNO (TEMP, NODE = 201, CONS = 644.3395)
BCNO (TEMP, NODE = 202, CONS = 647.5835)
BCNO (TEMP, NODE = 203, CONS = 650.8275)
BCNO (TEMP, NODE = 204, CONS = 654.0715)
BCNO (TEMP, NODE = 205, CONS = 657.3155)
BCNO (TEMP, NODE = 206, CONS = 680.0235)
BCNO (TEMP, NODE = 207, CONS = 676.1307)
BCNO (TEMP, NODE = 208, CONS = 672.2379)
BCNO (TEMP, NODE = 209, CONS = 668.3451)
BCNO (TEMP, NODE = 210, CONS = 664.4523)
BCNO (TEMP, NODE = 211, CONS = 493.088)
BCNO (TEMP, NODE = 212, CONS = 679.2125)
BCNO (TEMP, NODE = 213, CONS = 678.4015)

BCNO (TEMP, NODE = 214, CONS = 677.5905)
BCNO (TEMP, NODE = 215, CONS = 676.7795)
BCNO (TEMP, NODE = 216, CONS = 675.9685)
BCNO (TEMP, NODE = 217, CONS = 675.1575)
BCNO (TEMP, NODE = 218, CONS = 674.3465)
BCNO (TEMP, NODE = 219, CONS = 673.5355)
BCNO (TEMP, NODE = 220, CONS = 672.7245)
BCNO (TEMP, NODE = 221, CONS = 671.9135)
BCNO (TEMP, NODE = 222, CONS = 664.6145)
BCNO (TEMP, NODE = 223, CONS = 657.3155)
BCNO (TEMP, NODE = 224, CONS = 650.0165)
BCNO (TEMP, NODE = 225, CONS = 642.7175)
BCNO (TEMP, NODE = 226, CONS = 635.4185)
BCNO (TEMP, NODE = 227, CONS = 628.1195)
BCNO (TEMP, NODE = 228, CONS = 620.8205)
BCNO (TEMP, NODE = 229, CONS = 613.5215)
BCNO (TEMP, NODE = 230, CONS = 606.2225)
BCNO (TEMP, NODE = 231, CONS = 598.9235)
BCNO (TEMP, NODE = 232, CONS = 599.329)
BCNO (TEMP, NODE = 233, CONS = 599.7345)
BCNO (TEMP, NODE = 234, CONS = 600.14)
BCNO (TEMP, NODE = 235, CONS = 600.5455)
BCNO (TEMP, NODE = 236, CONS = 600.951)
BCNO (TEMP, NODE = 237, CONS = 601.3565)
BCNO (TEMP, NODE = 238, CONS = 601.762)
BCNO (TEMP, NODE = 239, CONS = 602.1675)
BCNO (TEMP, NODE = 240, CONS = 602.573)
BCNO (TEMP, NODE = 241, CONS = 602.9785)
BCNO (TEMP, NODE = 242, CONS = 603.384)
BCNO (TEMP, NODE = 243, CONS = 597.3015)
BCNO (TEMP, NODE = 244, CONS = 591.219)
BCNO (TEMP, NODE = 245, CONS = 585.1365)
BCNO (TEMP, NODE = 246, CONS = 579.054)
BCNO (TEMP, NODE = 247, CONS = 572.9715)
BCNO (TEMP, NODE = 248, CONS = 566.889)
BCNO (TEMP, NODE = 249, CONS = 560.8065)
BCNO (TEMP, NODE = 250, CONS = 564.0505)
BCNO (TEMP, NODE = 251, CONS = 567.2945)
BCNO (TEMP, NODE = 252, CONS = 570.5385)
BCNO (TEMP, NODE = 253, CONS = 573.7825)

BCNO (TEMP, NODE = 254, CONS = 577.0265)
BCNO (TEMP, NODE = 255, CONS = 580.2705)
BCNO (TEMP, NODE = 256, CONS = 583.5145)
BCNO (TEMP, NODE = 257, CONS = 571.3495)
BCNO (TEMP, NODE = 258, CONS = 559.1845)
BCNO (TEMP, NODE = 259, CONS = 547.0195)
BCNO (TEMP, NODE = 260, CONS = 534.8545)
BCNO (TEMP, NODE = 261, CONS = 522.6895)
BCNO (TEMP, NODE = 262, CONS = 529.1775)
BCNO (TEMP, NODE = 263, CONS = 535.6655)
BCNO (TEMP, NODE = 264, CONS = 542.1535)
BCNO (TEMP, NODE = 265, CONS = 548.6415)
BCNO (TEMP, NODE = 266, CONS = 545.3975)
BCNO (TEMP, NODE = 267, CONS = 542.1535)
BCNO (TEMP, NODE = 268, CONS = 538.9095)
BCNO (TEMP, NODE = 269, CONS = 535.6655)
BCNO (TEMP, NODE = 270, CONS = 532.4215)
BCNO (TEMP, NODE = 271, CONS = 529.1775)
BCNO (TEMP, NODE = 272, CONS = 525.9335)
BCNO (TEMP, NODE = 273, CONS = 522.6895)
BCNO (TEMP, NODE = 274, CONS = 519.4455)
BCNO (TEMP, NODE = 275, CONS = 516.2015)
BCNO (TEMP, NODE = 276, CONS = 512.9575)
BCNO (TEMP, NODE = 277, CONS = 509.7135)
BCNO (TEMP, NODE = 278, CONS = 506.4695)
BCNO (TEMP, NODE = 279, CONS = 503.2255)
BCNO (TEMP, NODE = 280, CONS = 499.9815)
BCNO (TEMP, NODE = 281, CONS = 496.7375)
BCNO (TEMP, NODE = 282, CONS = 499.9815)
BCNO (TEMP, NODE = 283, CONS = 503.2255)
BCNO (TEMP, NODE = 284, CONS = 506.4695)
BCNO (TEMP, NODE = 285, CONS = 509.7135)
BCNO (TEMP, NODE = 286, CONS = 512.9575)
BCNO (TEMP, NODE = 287, CONS = 516.2015)
BCNO (TEMP, NODE = 288, CONS = 519.4455)
BCNO (TEMP, NODE = 289, CONS = 522.6895)
BCNO (TEMP, NODE = 290, CONS = 525.9335)
BCNO (TEMP, NODE = 291, CONS = 522.6895)
BCNO (TEMP, NODE = 292, CONS = 519.4455)
BCNO (TEMP, NODE = 293, CONS = 516.2015)

BCNO (TEMP, NODE = 294, CONS = 512.9575)
BCNO (TEMP, NODE = 295, CONS = 509.7135)
BCNO (TEMP, NODE = 296, CONS = 506.4695)
BCNO (TEMP, NODE = 297, CONS = 503.2255)
BCNO (TEMP, NODE = 298, CONS = 499.9815)
BCNO (TEMP, NODE = 299, CONS = 496.7375)
BCNO (TEMP, NODE = 300, CONS = 493.4935)
BCNO (TEMP, NODE = 301, CONS = 490.2495)
BCNO (TEMP, NODE = 302, CONS = 495.1155)
BCNO (TEMP, NODE = 303, CONS = 499.9815)
BCNO (TEMP, NODE = 304, CONS = 504.8475)
BCNO (TEMP, NODE = 305, CONS = 509.7135)
BCNO (TEMP, NODE = 306, CONS = 514.5795)
BCNO (TEMP, NODE = 307, CONS = 519.4455)
BCNO (TEMP, NODE = 308, CONS = 524.3115)
BCNO (TEMP, NODE = 309, CONS = 521.0675)
BCNO (TEMP, NODE = 310, CONS = 517.8235)
BCNO (TEMP, NODE = 311, CONS = 514.5795)
BCNO (TEMP, NODE = 312, CONS = 511.3355)
BCNO (TEMP, NODE = 313, CONS = 508.0915)
BCNO (TEMP, NODE = 314, CONS = 504.8475)
BCNO (TEMP, NODE = 315, CONS = 501.6035)
BCNO (TEMP, NODE = 316, CONS = 498.3595)
BCNO (TEMP, NODE = 317, CONS = 495.1155)
BCNO (TEMP, NODE = 318, CONS = 491.8715)
BCNO (TEMP, NODE = 319, CONS = 488.6275)
BCNO (TEMP, NODE = 320, CONS = 491.8715)
BCNO (TEMP, NODE = 321, CONS = 495.1155)
BCNO (TEMP, NODE = 322, CONS = 498.3595)
BCNO (TEMP, NODE = 323, CONS = 501.6035)
BCNO (TEMP, NODE = 324, CONS = 504.8475)
BCNO (TEMP, NODE = 325, CONS = 508.0915)
BCNO (TEMP, NODE = 326, CONS = 511.3355)
BCNO (TEMP, NODE = 327, CONS = 514.5975)
BCNO (TEMP, NODE = 328, CONS = 517.8235)
BCNO (TEMP, NODE = 329, CONS = 514.985)
BCNO (TEMP, NODE = 330, CONS = 512.1465)
BCNO (TEMP, NODE = 331, CONS = 509.308)
BCNO (TEMP, NODE = 332, CONS = 506.4695)
BCNO (TEMP, NODE = 333, CONS = 503.631)

```
BCNO (TEMP, NODE = 334, CONS = 500.7925)
BCNO (TEMP, NODE = 335, CONS = 497.954)
BCNO (TEMP, NODE = 336, CONS = 495.1155)
BCNO (TEMP, NODE = 337, CONS = 492.277)
BCNO (TEMP, NODE = 338, CONS = 489.4385)
BCNO (TEMP, NODE = 339, CONS = 486.6)
BCNO (TEMP, NODE = 340, CONS = 483.7615)
BCNO (TEMP, NODE = 341, CONS = 480.923)
BCNO (TEMP, NODE = 342, CONS = 478.0845)
BCNO (TEMP, NODE = 343, CONS = 475.246)
BCNO (TEMP, NODE = 344, CONS = 472.4075)
BCNO (TEMP, NODE = 345, CONS = 469.569)
BCNO (TEMP, NODE = 346, CONS = 466.7305)
BCNO (TEMP, NODE = 347, CONS = 463.892)
BCNO (TEMP, NODE = 348, CONS = 468.758)
BCNO (TEMP, NODE = 349, CONS = 473.624)
BCNO (TEMP, NODE = 350, CONS = 478.49)
BCNO (TEMP, NODE = 351, CONS = 483.356)
BCNO (TEMP, NODE = 352, CONS = 488.222)
BCNO (TEMP, NODE = 353, CONS = 517.418)
BCNO (TEMP, NODE = 354, CONS = 497.954)
BCNO (TEMP, NODE = 355, CONS = 502.82)
BCNO (TEMP, NODE = 356, CONS = 507.686)
BCNO (TEMP, NODE = 357, CONS = 512.552)
BCNO (TEMP, NODE = 358, CONS = 519.851)
BCNO (TEMP, NODE = 359, CONS = 522.284)
BCNO (TEMP, NODE = 360, CONS = 524.717)
BCNO (TEMP, NODE = 361, CONS = 527.15)
BCNO (TEMP, NODE = 362, CONS = 529.583)
BCNO (TEMP, NODE = 363, CONS = 532.016)
BCNO (TEMP, NODE = 364, CONS = 534.449)
BCNO (TEMP, NODE = 365, CONS = 536.882)
BCNO (TEMP, NODE = 366, CONS = 539.315)
BCNO (TEMP, NODE = 367, CONS = 541.748)
BCNO (TEMP, NODE = 368, CONS = 544.181)
BCNO (TEMP, NODE = 369, CONS = 546.614)
BCNO (TEMP, NODE = 370, CONS = 549.047)
BCNO (TEMP, NODE = 371, CONS = 551.48)
ICNO (TEMP, CONS = 293.0, ALL)
END
```

```
/  *** of FIPREP Commands
CREATE(FIPREP,DELE)
CREATE(FISOLV)
PARAMETER(LIST)
/
/
```

APPENDIX E

Contours and Equations for Chapter 4

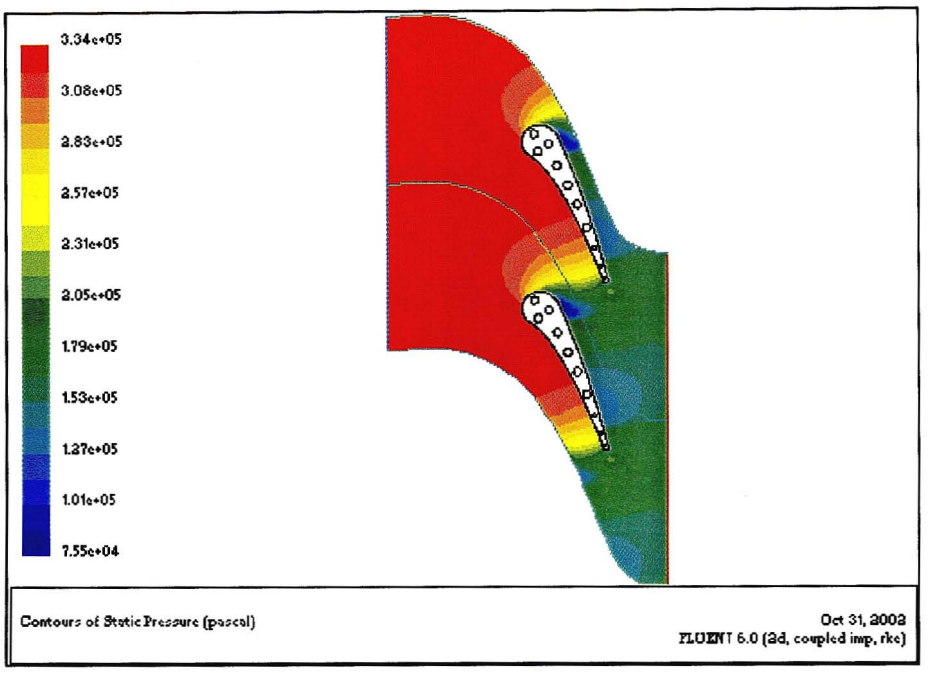

Figure E-1a: FLUENT static pressure contours

Figures E-1a and b show the static pressure contours through the Mark II cascade. The static pressure value drops from 3.34 bar through the blade passage corresponding to the flow accelerating through this region due to the reduction in area. The velocity vectors through the cascade are shown in Figures E-2a to f. The pressure loss is evident by the pressure contours reducing in magnitude from red to blue and corresponds to the velocity vectors increasing in magnitude from blue to red. The lowest static pressure (0.755 bar) occurs at the throat (the smallest area) where the velocity vectors are at their maximum supersonic value of Mach 1.6.

Pressure recovery is evident after the throat, which was expected because of the increase in area over the uncovered portion of the blade. The rate of the pressure recovery indicates a normal shock wave present just after the throat. Further evidence of this can be seen in Figures E-2b and c. The flow velocity increases up to Mach 1.6 and then suddenly drops to approximately Mach 0.8. Figures E-2d to g give the velocity vectors close to the blade surface from the top of the blade through to just past the shock wave. This was done to show the nature of the viscous affected region. The thin viscous affected zone is indicative of a turbulent boundary layer, which is emphasised by the Re_y plot in Figure E-2h where $Re_y = 200$ demarcates the turbulent region from the viscous region.

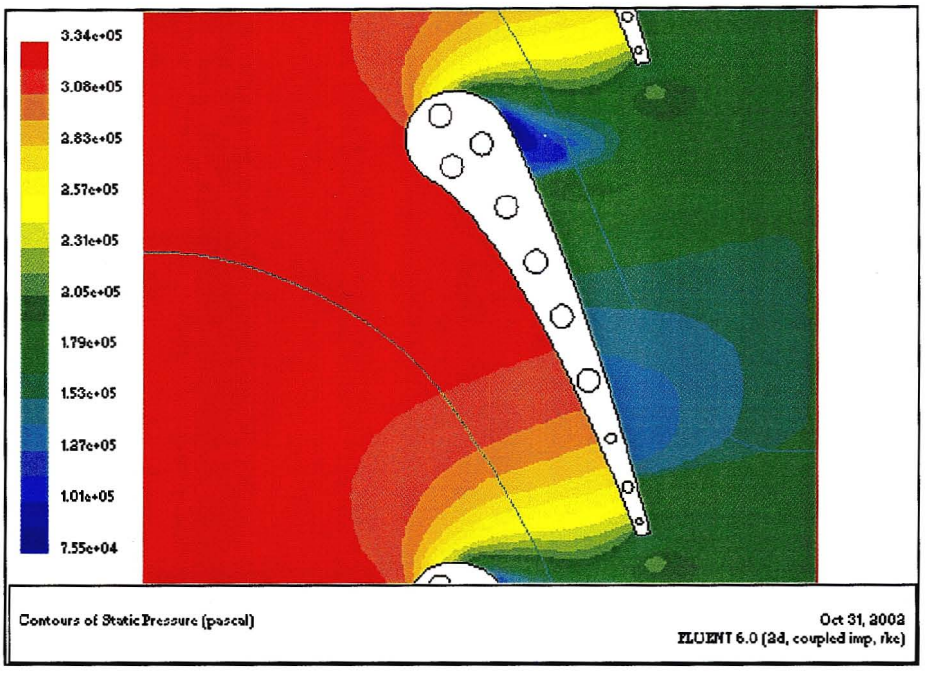

Figure E-1b: FLUENT static pressure contours - close-up around blade

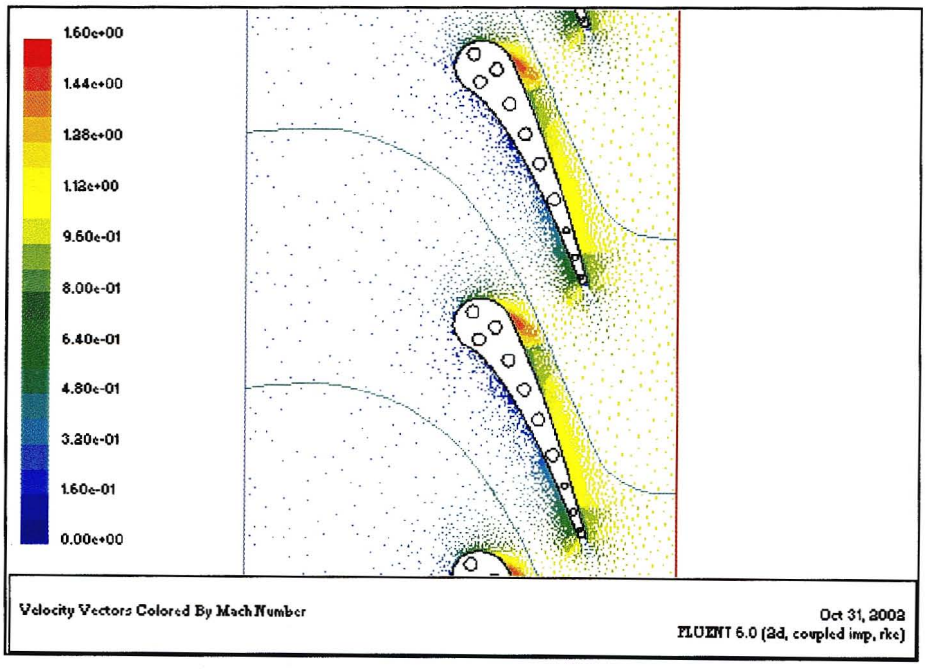

Figure E-2a: Velocity vectors for cascade - 3 periodic repetitions shown

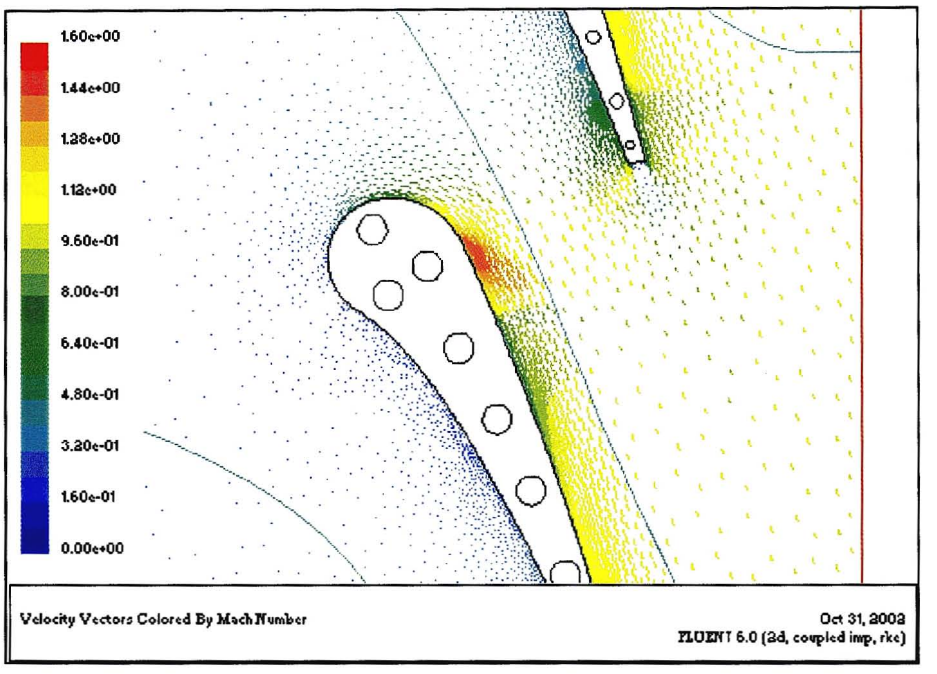

Figure E-2b: Velocity vectors for the throat region in the blade-to-blade passage

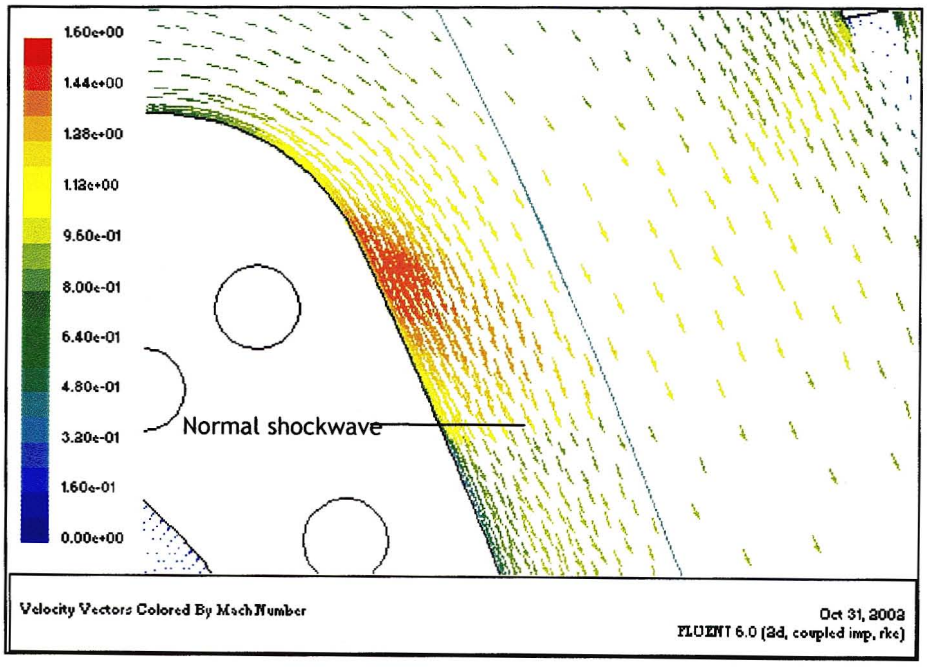

Figure E-2c: Velocity vectors for the throat region showing normal shockwave

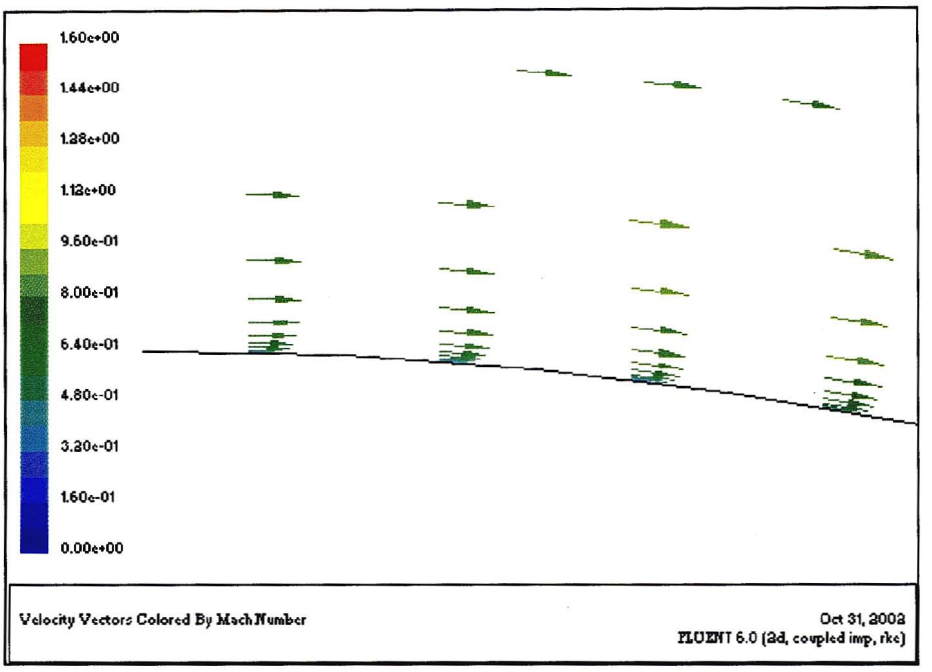

Figure E-2d: Velocity vectors before shock

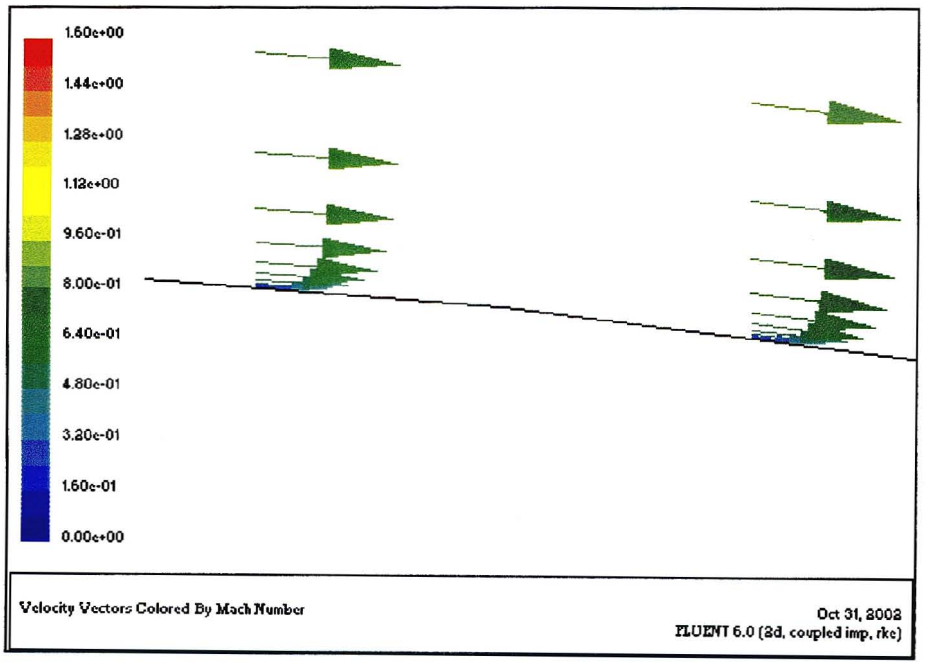

Figure E-2e: Close-up of velocity vectors before shock

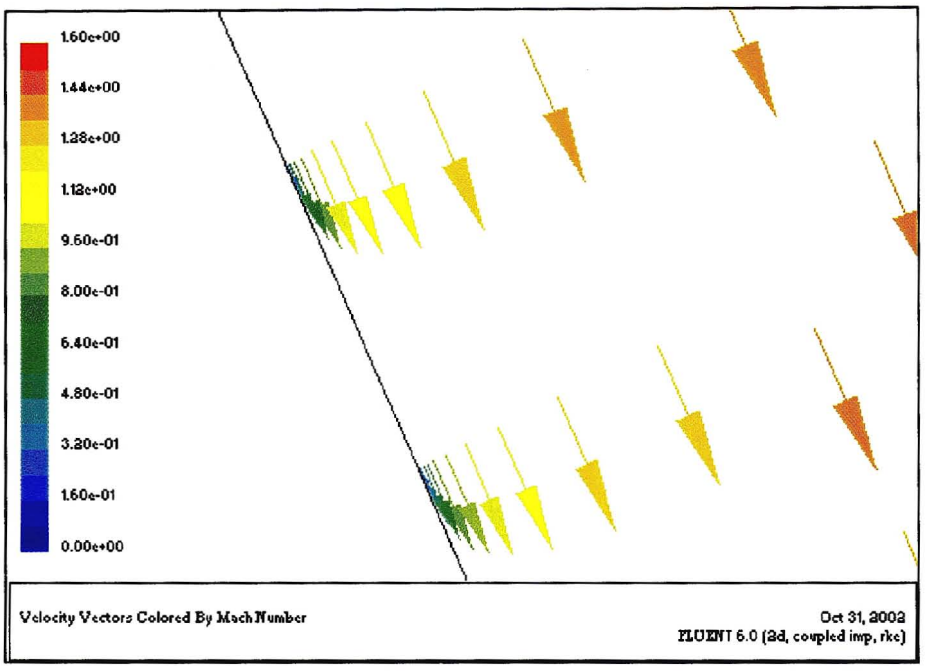

Figure E-2f: Close-up of velocity vectors at the shock showing the effect of viscosity in the near-wall region

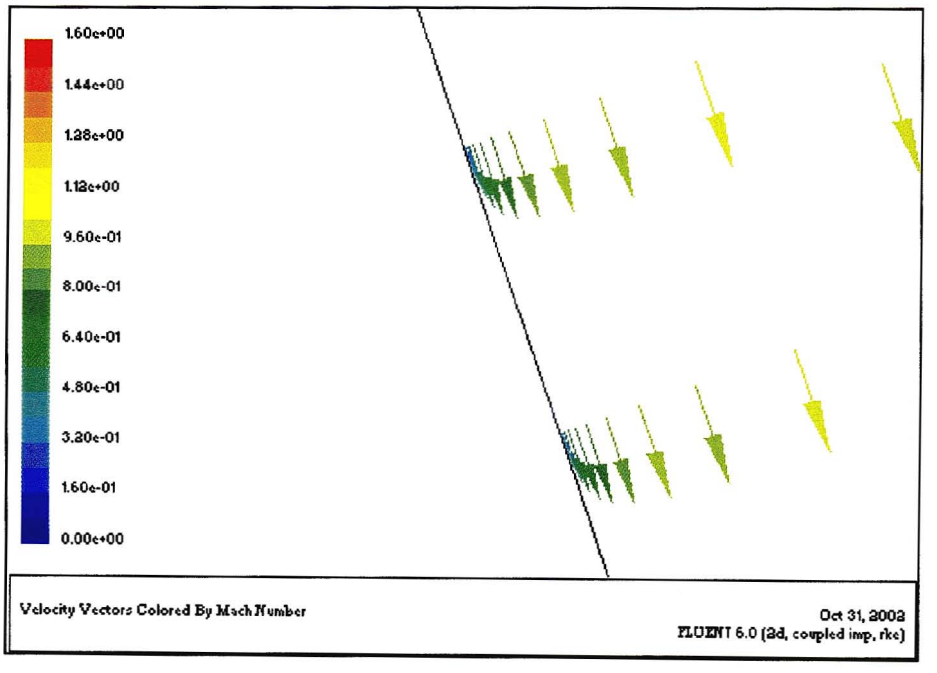

Figure E-2g: Velocity vectors after shock

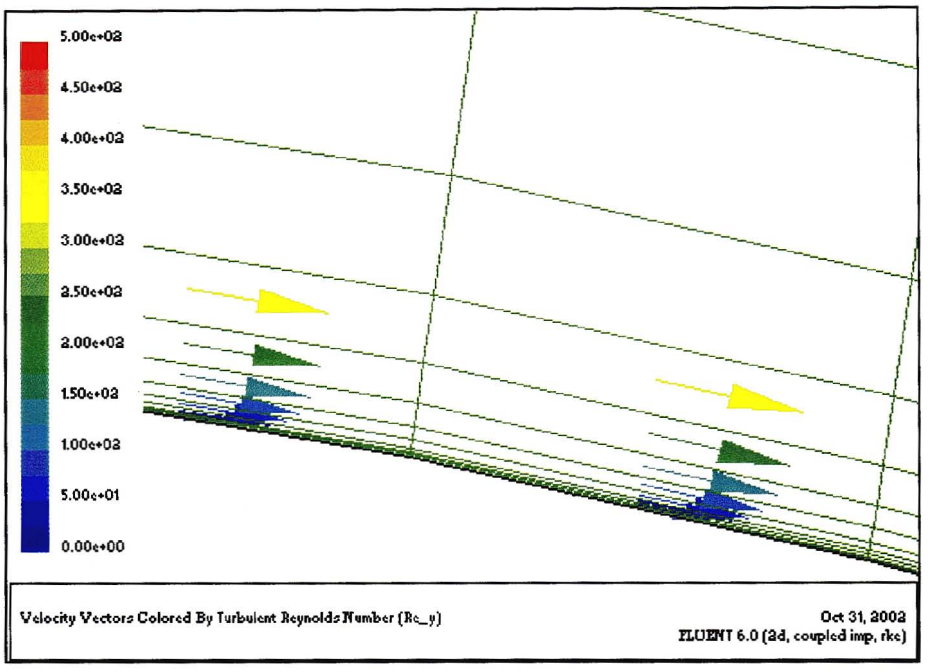

Figure E-2h: Re_y vectors shown with boundary layer mesh

Figures E-3 and 4 give the stress component contours for the cylinder predicted by NASTRAN and FIDAP. The σ_x and σ_y contours indicate maximum values at the centre and decrease towards the surface. This is also seen in the σ_z contours. From the contours it is evident that end effects are limited to approximately 1-diameter from the end.

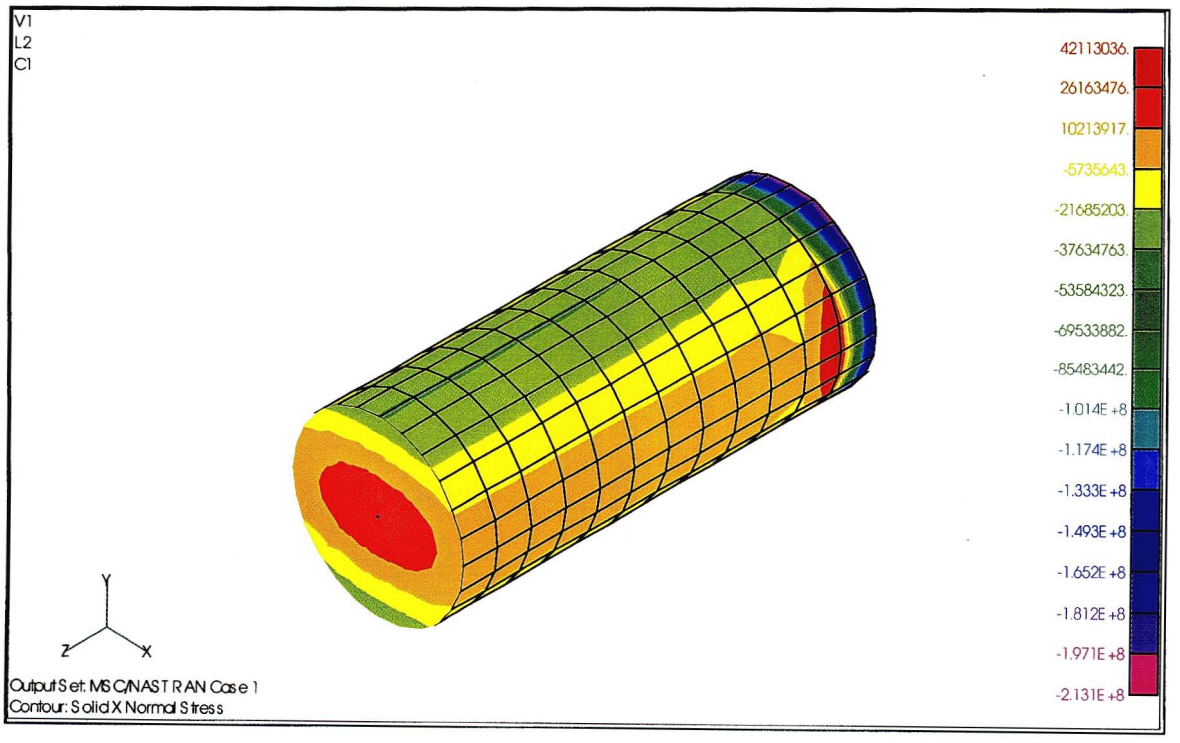

Figure E-3a: σ_x contours for the cylinder - NASTRAN

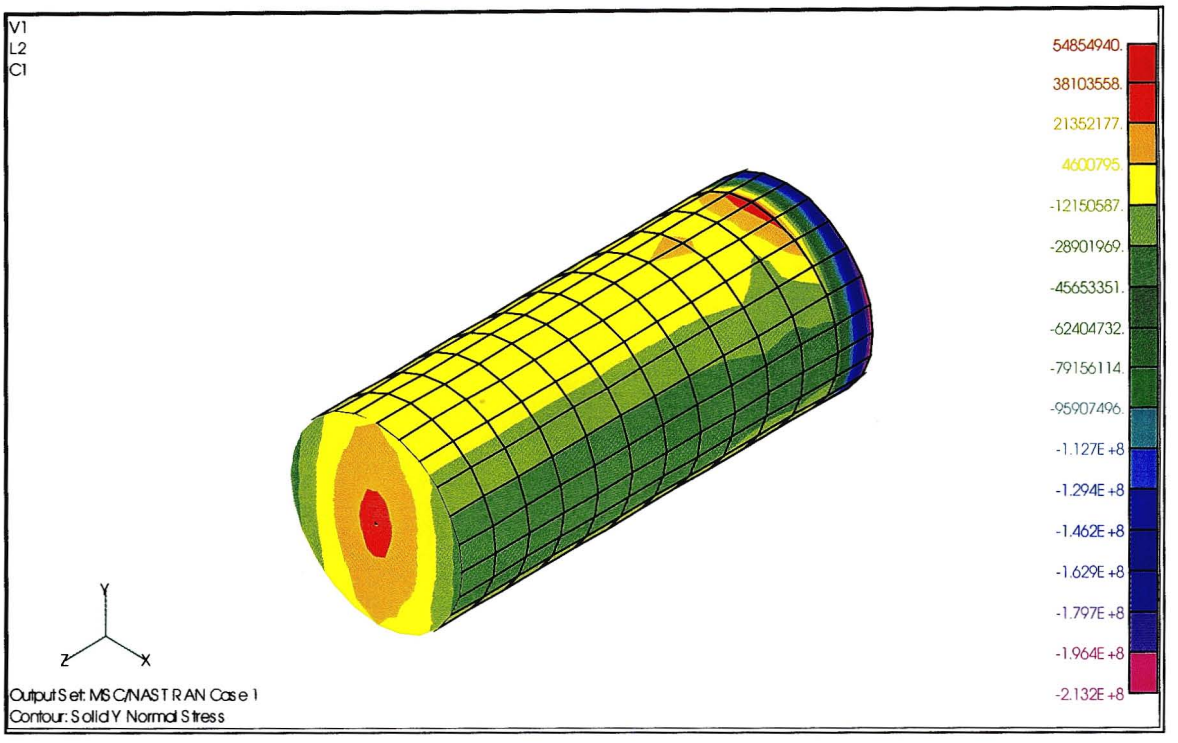

Figure E-3b: σ_y contours for the cylinder - NASTRAN

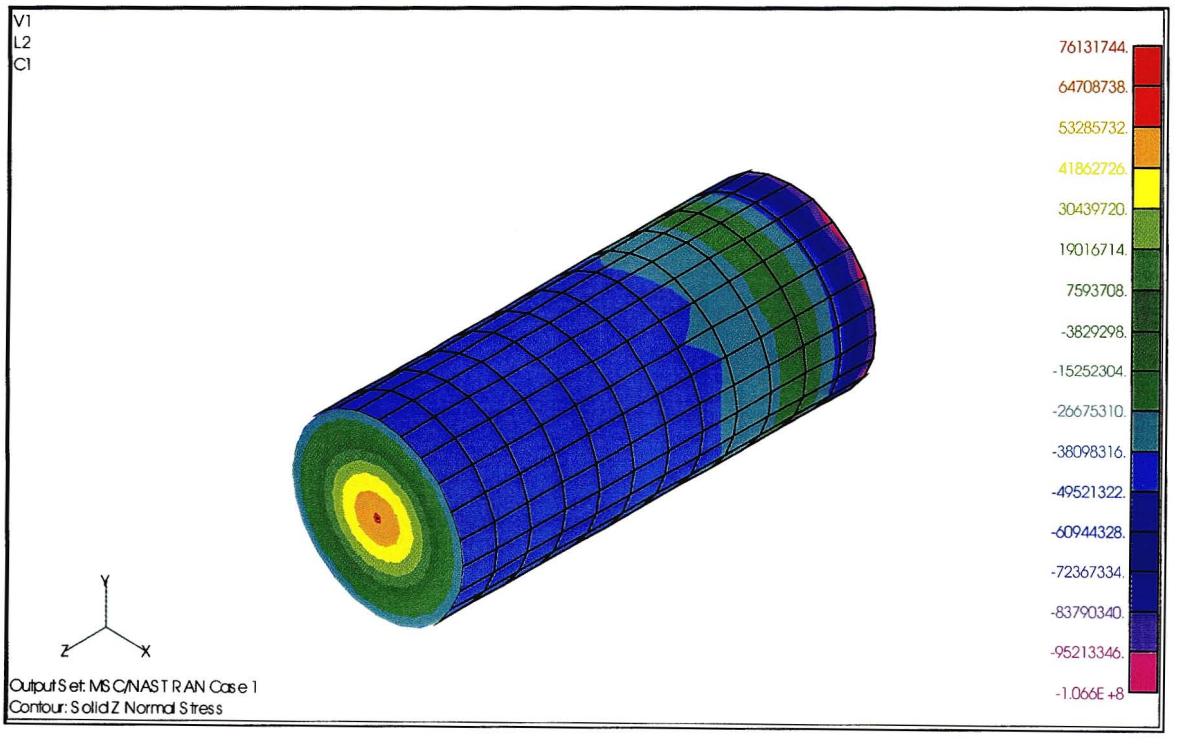

Figure E-3c: σ_z contours for the cylinder - NASTRAN

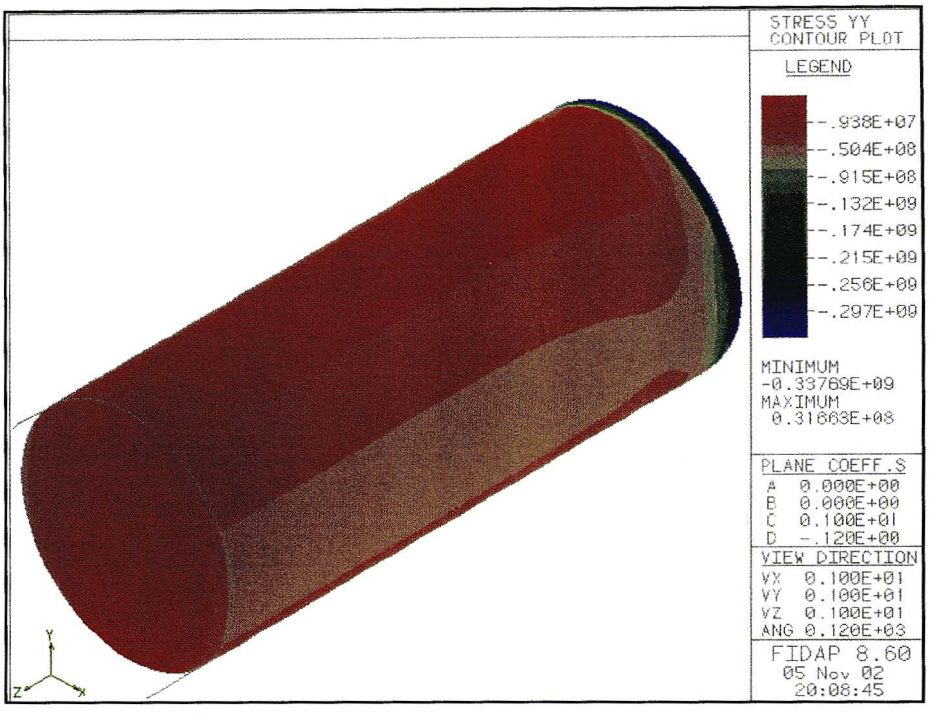

Figure E-4b: σ_y contours for the cylinder - FIDAP

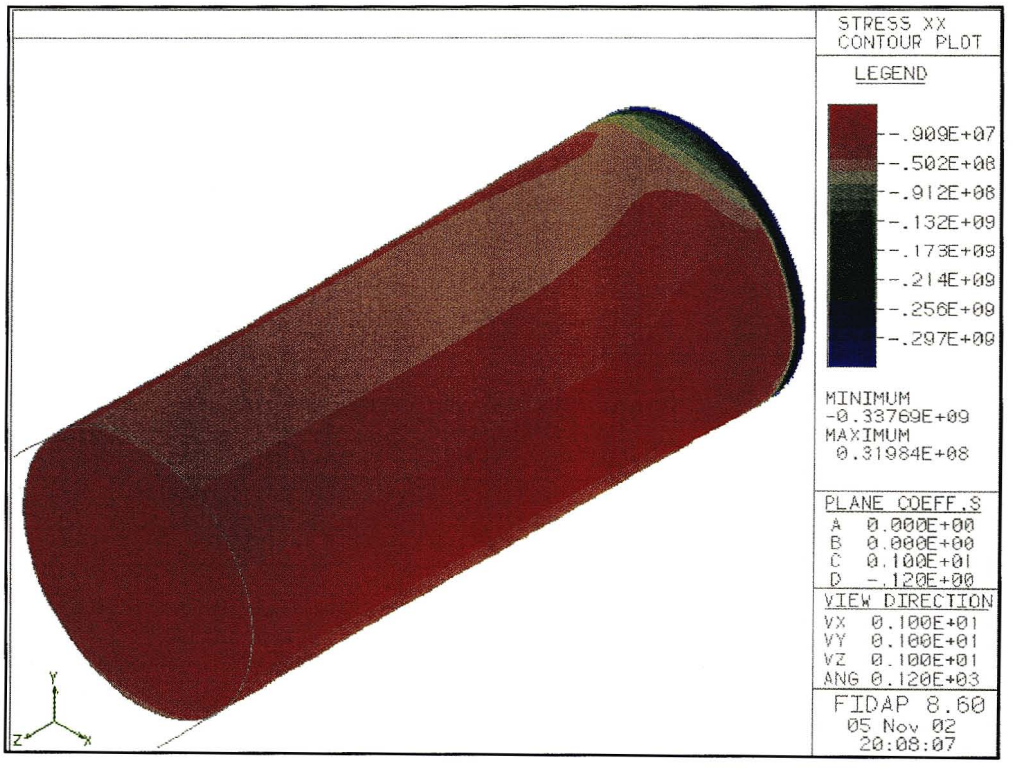

Figure E-4a: σ_x contours for the cylinder - FIDAP

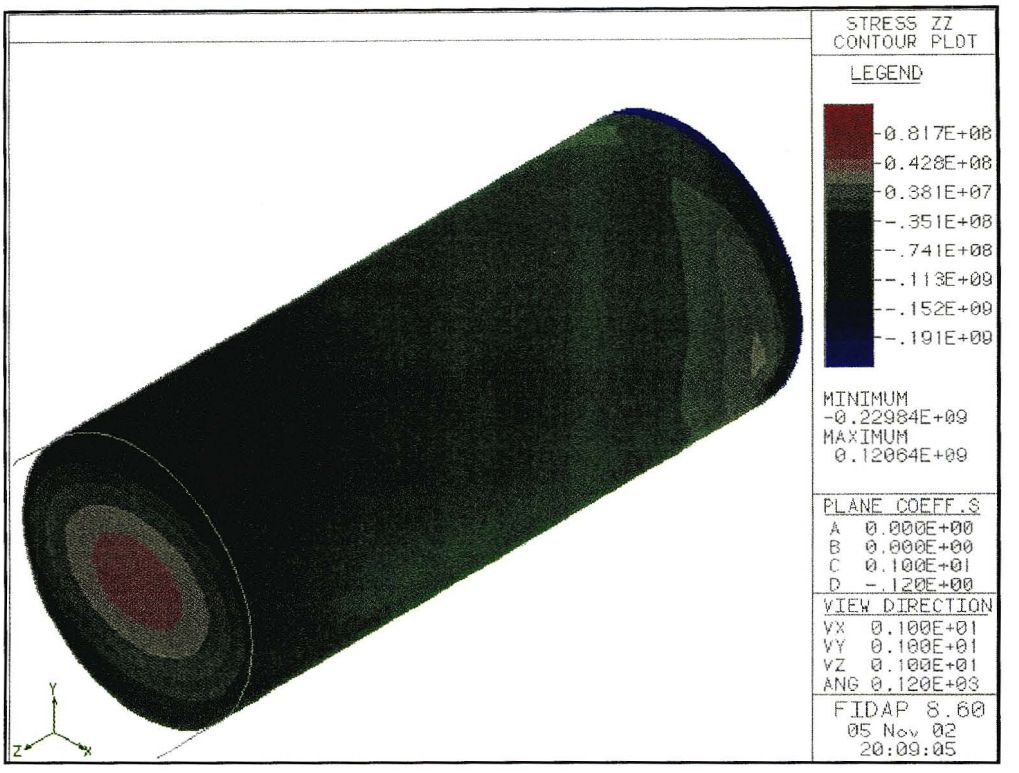

Figure E-4c: σ_z contours for the cylinder - FIDAP

The equations for the thermal stresses in the cylinder are explained below. The 1-D steady state (Eq E-1a) and transient (Eq E-1b) Fourier heat conduction equations in cylindrical co-ordinates are given by:

$$\frac{\partial^2 T}{\partial r^2} + \frac{1}{r}\frac{\partial T}{\partial r} = 0 \qquad \text{Eq E-1a}$$

$$\frac{\partial^2 T}{\partial r^2} + \frac{1}{r}\frac{\partial T}{\partial r} - \frac{1}{\gamma}\frac{\partial T}{\partial t} = 0 \qquad \text{Eq E-1b}$$

Where:

T = Temperature

r = Position along the cylinder radius, or in the radial coordinate direction

t = Time

γ = Coefficient of thermal diffusivity [m^2/s]

Eqs E-1a and b were solved, with appropriate boundary conditions, by Ali and Alam (1997) and Carslaw and Jaeger (1956) respectively, to yield the radially varying temperature profiles given by Eqs E-2a and b respectively:

$$T_N = \frac{T - T_i}{T_s - T_i} = 1 - J_0\left(\beta_m \frac{r}{R}\right) \qquad \text{Eq E-2a}$$

$$T = \frac{2Q\gamma t}{kR} + \frac{QR}{k}\left[\frac{r^2}{2R^2} - \frac{1}{4} - 2\sum_{n=1}^{\infty} e^{-\frac{\gamma}{R^2}\beta_n^2} \frac{J_0\left(\beta_n \frac{r}{R}\right)}{\beta_n^2 J_0(\beta_n)}\right] \qquad \text{Eq E-2b}$$

Where:

T, r, t and γ are as previously defined

T_N = Non-dimensionalised temperature

T_i = Temperature at the centre of the cylinder, $r = 0$

T_s = Temperature at the surface of the cylinder, $r = R$

R = Radius of the cylinder

Q = Heat flux [W/m^2]

k = Thermal conductivity [W/mK]

J_0 = Bessel function of the first king of order 0

β_m = Roots of the transcendental equation $J_0(\beta_m) = 0$ given in Table E-1

β_n = Roots of the transcendental equation $J_1(\beta_n) = 0$ given in Table E-2, where J_1 is the Bessel function of order 1

The polynomial approximation form of Eq E-2a, used to input the temperature profile into the solvers given by Eq E-3:

$$T_N = \left(\frac{r}{R}\right)^{1.6} \qquad \text{Eq E-3}$$

The thermal stresses in the cylinder, assuming plain strain conditions and zero axial force, are computed by integrating Eqs E-4a, b and c where T is the temperature profile in the cylinder given by Eq E-2a or b.

$$\sigma_r = \frac{E\alpha}{1-\nu}\left[\frac{1}{R^2}\int_0^R Trdr - \frac{1}{r^2}\int_0^r Trdr\right] \qquad \text{Eq E-4a}$$

$$\sigma_\theta = \frac{E\alpha}{1-\nu}\left[\frac{1}{R^2}\int_0^R Trdr + \frac{1}{r^2}\int_0^r Trdr - T\right] \qquad \text{Eq E-4b}$$

$$\sigma_z = \frac{E\alpha}{1-\nu}\left[\frac{2}{R^2}\int_0^R Trdr - T\right] \qquad \text{Eq E-4c}$$

Where:

σ_r	=	Component of thermal stress in the radial coordinate direction
σ_θ	=	Component of thermal stress in the tangential coordinate direction
σ_z	=	Component of thermal stress in the axial coordinate direction
E	=	Young's modulus [GPa]
α	=	Coefficient of thermal expansion [m/mK]
ν	=	Poisson's ratio

Plain strain conditions are defined by the elastic stain components $\varepsilon_{\theta z} = \varepsilon_{rz} = \varepsilon_z = 0$. The principal elastic strain components are given by Eqs E-5a, b and c:

$$\varepsilon_r - \alpha T = \frac{1}{E}[\sigma_r - \nu(\sigma_\theta + \sigma_z)] \qquad \text{Eq E-5a}$$

$$\varepsilon_\theta - \alpha T = \frac{1}{E}[\sigma_\theta - \nu(\sigma_r + \sigma_z)] \qquad \text{Eq E-5b}$$

$$\varepsilon_z - \alpha T = \frac{1}{E}[\sigma_z - \nu(\sigma_r + \sigma_\theta)] \qquad \text{Eq E-5c}$$

Under plain strain conditions and the equilibrium condition of force in the axial direction (F_z) equal to zero (Eq E-6), the axial thermal stress component obtained by integrating Eq E-4c can be approximated by setting $\varepsilon_z = 0$ in Eq E-5c to give Eq E-7:

$$\sum \sigma_i A_i = 0 \qquad \text{Eq E-6}$$

$$\sigma_z = \nu(\sigma_r + \sigma_\theta) - E\alpha T \qquad \text{Eq E-7}$$

The equations for the stress components are given in cylindrical coordinates, and will retain their form in Cartesian coordinates. The equations are easily modified for Cartesian coordinates by simply replacing the coordinate r with x and θ with y. For completeness the definition of equivalent stress is given by Eq E-8, and is written in Cartesian coordinates.

$$2\sigma_e^2 = (\sigma_x - \sigma_y)^2 + \sigma_x^2 + \sigma_y^2 \qquad \text{Eq E-8}$$

n	β_n
1	3.83171
2	7.01559
3	10.1735
4	13.3237
5	16.4706
6	19.6159
7	22.7601
8	25.9037
9	29.0468
10	32.1897

Table E-1: First 10 roots of the transcendental equation $J_1(\beta_n) = 0$

m	β_m
1	2.40482
2	5.52007
3	8.65372
4	11.79153
5	14.93091
6	18.07106
7	21.21163
8	24.35247
9	27.49347
10	30.63460

Table E-2: First 10 roots of the transcendental equation $J_0(\beta_m) = 0$

For the aerodynamics analysis, a critical parameter in the numerical simulation of heat transfer is the wall y^+ value, which is given by Eq E-9:

$$y^+ = \frac{\rho u_\tau y}{\mu} \qquad \text{Eq E-9}$$

$$u_\tau = \sqrt{\frac{\tau_0}{\rho}} \qquad \text{Eq E-9.1}$$

Where:

y^+ = The characteristic non-dimensionalised distance from the wall for the given cell centre

y = Distance from the wall to the cell centre of the wall adjacent cells [m]

ρ = Fluid density [kg/m^3]

u_τ = Friction velocity [m/s] given by Eq E-9.1, with τ_0 = viscous shear stress

μ = Dynamic viscosity [Ns/m^2 or kg/m^2]

The turbulent Reynold's number (Re_y), which is used to define the edge of the fully turbulent core, is given by Eq E-10:

$$\mathrm{Re}_y = \frac{\rho y \sqrt{k}}{\mu} \qquad \text{Eq E-10}$$

Where:

k = Turbulent kinetic energy

In the analysis, Reynolds number is defined as:

$$\mathrm{Re}_x = \frac{\rho u x}{\mu} \qquad \text{Eq E-11}$$

Where:

u = Velocity [m/s]

x = Critical length parameter, axial chord length (L) for calculation in chapter 4

Compressibility of the gas in the aerodynamic analysis was modelled using the ideal gas equation:

$$\rho = \frac{P_s}{R_{air}T} \qquad \text{Eq E-12}$$

Where:

P_s = Static Pressure [Pa]

R_{air} = Gas constant for air = 287 kJ/kgK

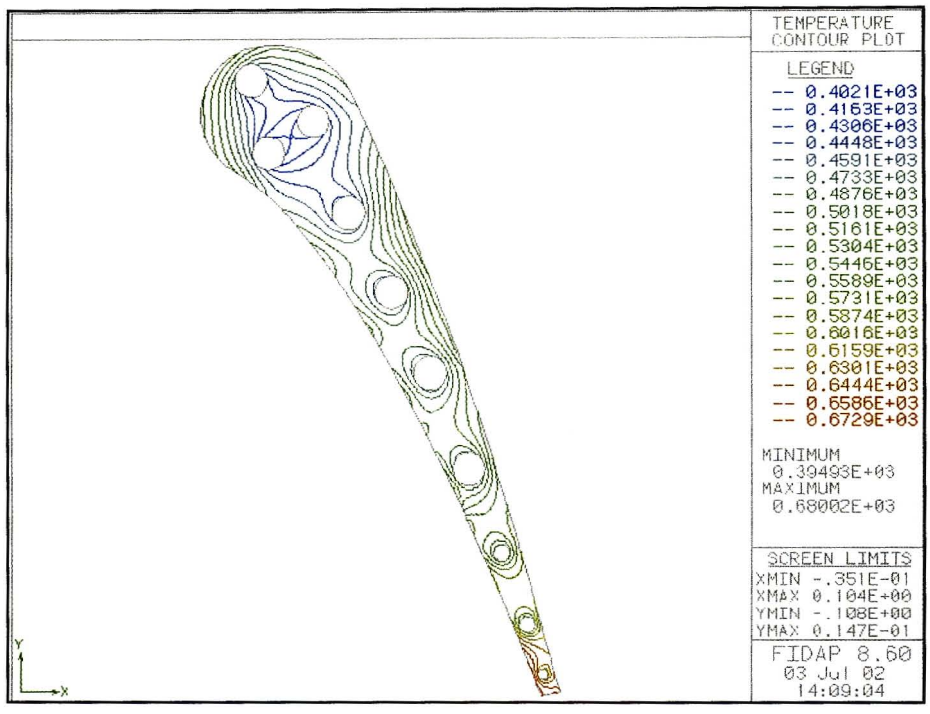

Figure E-5a: Temperature contours for the Mark II NGV - FIDAP

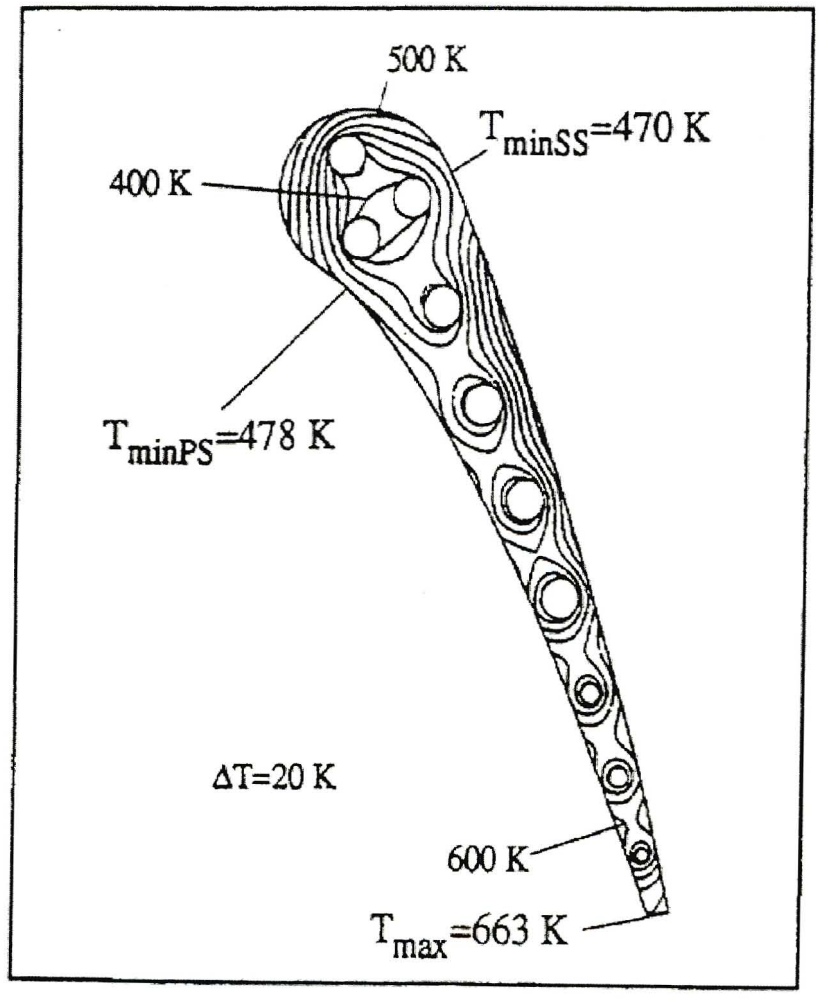

Figure E-5b: Temperature contours for the Mark II NGV - reproduced from Bohn et. al. (1995)

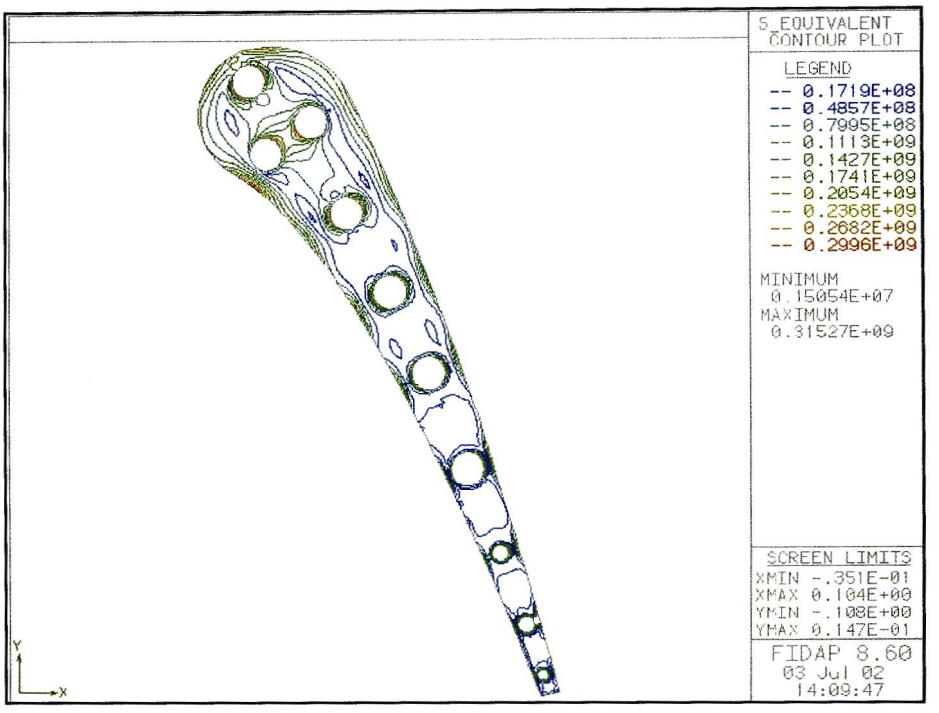

Figure E-6a: σ_e contours for the Mark II NGV - FIDAP

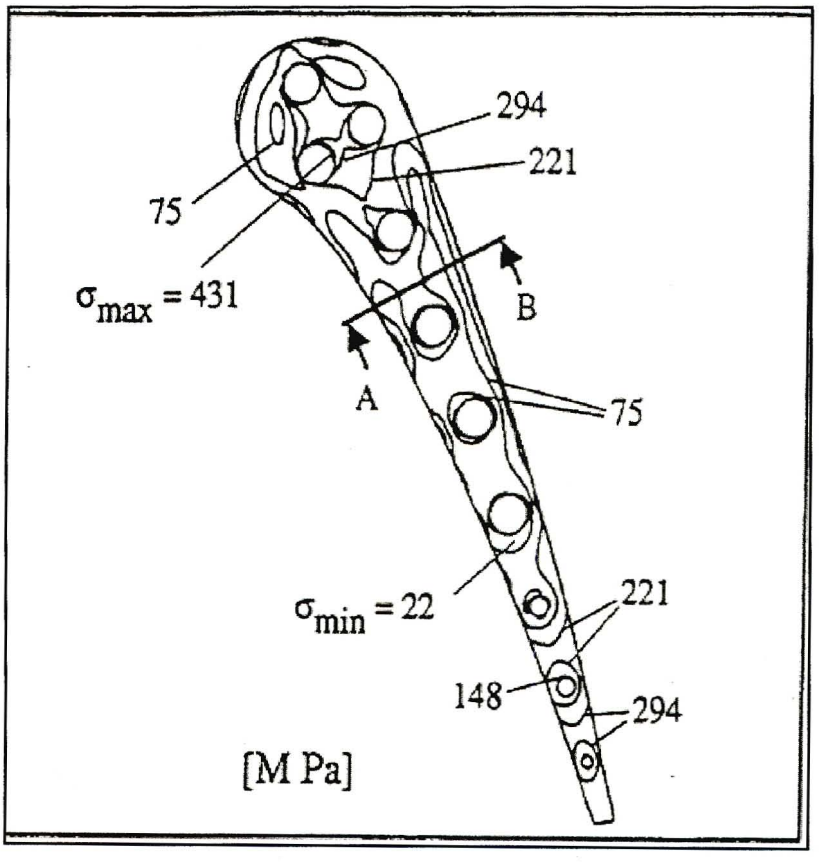

Figure E-6b: σ_e contours for the Mark II NGV - reproduced from Bohn et. al. (1995)

Figures E-5 and 6 give the predicted temperature and σ_e contours for the Mark II NGV together with the contours presented by Bohn et. al. (1995). The temperature contours show the coolest region to be at the cooling holes with the temperature increasing towards the surface. The temperature gradient in the vicinity of the trailing edge is much smaller that the leading edge region due there being less thickness in the trailing edge region. The σ_e contours show that the maximum stress occurs in the leading edge region where the temperature gradient is large. Figures E-5 and 6 were discussed in significant detail in the chapter 4.

APPENDIX F

Equations for Chapter 5

The data points in Figure 5-6 (Chapter 5) were used to develop a loose law that approximates the maximum equivalent stress as a function of TIT, by means of a polynomial. Due to the cyclic nature of the data points, a single curve could not be fitted through all the points. Instead, curves were fitted through the maximums and minimums, and the mean was calculated.

Max σ_e max (startup), where T represents turbine inlet temperature (K)

$$\max \sigma_e \max(startup) = 0.8889T - 211.83 \qquad \text{Eq F-1}$$

Min σ_e max (startup)

$$\min \sigma_e \max(startup) = 0.7564T - 171.02 \qquad \text{Eq F-2}$$

Max σ_e max

$$\max \sigma_e \max = -1.1376E-07T^4 + 4.9244E-04T^3 \ldots$$
$$-7.9157E-01T^2 + 5.6047E02T - 1.47E05 \qquad \text{Eq F-3}$$

Min σ_e max

$$\min \sigma_e \max = -3.0917E-07T^4 + 1.3487E-04T^3 \ldots$$
$$-2.186E00T^2 + 1.5604E03T - 4.1353E05 \qquad \text{Eq F-4}$$

Using Eqs F-1 to 4, one may approximate the maximum σ_e by calculating the Mean σ_e max

$$mean\sigma_e \max = \frac{\max \sigma_{e\max} + \min \sigma_e \max}{2} \qquad \text{Eq F-5}$$

BIBLIOGRAPHY

Abbot M. B., Computational Fluid Dynamics: An Introduction for Engineers, 1976.

Abramowitz M. and Stegun I. A., Handbook of Mathematical Functions with Formula, Graphs and Mathematical Tables, National Bureau of Standards, Wiley, 1972.

Adamczyk J. J., Aerodynamic Analysis of Multistage Turbomachinery Flows in Support of Aerodynamic Design., Journal of Turbomachinery, ASME, Vol. 122, 2002, pp189-217.

Adamczyk J. J., Celestina M. L., Beach T. A. and Barnett M., Simulation of Three Dimensional Viscous Flow within a Multistage Turbine, Journal of Turbomachinery, ASME, Vol. 112, 1990, pp 370-376.

Ali Z. and Alam M. K., Thermal Stresses in a Cylinder with Temperature Dependant Properties, Journal of Manufacturing Science and Engineering, Vol. 119, 1997, pp448-453.

ASM International, Properties and Selection: Iron, Steels and High Performance Alloys, Metal's Handbook, Vol. 1, 10^{th} Ed.

Baker A. J., Finite Element Computational Fluid Mechanics, McGraw-Hill, 1976.

Binder R. C., Advanced Fluid Mechanics, Vol. II, Prentice-Hall, 1958.

Blair M. F., An Experimental Study of Heat Transfer and Film Cooling on Large Scale Turbine Endwalls, Journal of Heat Transfer, ASME, November, 1974.

Blair M., Influence of Free-Stream Turbulence on Boundary Layer Transition in Favourable Pressure Gradients, Journal of Engineering for Power, ASME, Vol. 104, 1982, pp 743-750.

Bohn D., Lang G., Schronerborn H. and Bonhoff B., Determination of Thermal Stress and Strain Based on a Combined Aerodynamic and Thermal Analysis for a Turbine Nozzle Guide Vane, ASME Cogen-Turbo Power Conference, Vienna, Austria, 23-25 August 1995.

Brown A. and Burton R. C., The Effect of Free-Stream Turbulence Intensity and Velocity Distribution on Heat Transfer to Curved Surfaces, Journal of Engineering for Power, ASME, Vol. 100, 1978, pp 159-168.

Burgreen D., Elements of Thermal Stresses, Areturus, 1971.

Carslaw H. S. and Jaeger J. C., Conduction of Heat in Solids, Oxford, 1959, pp 203-204.

Cebeci T. and Smith A. M. O., Analysis of Boundary Layers, Academic Press, 1974.

Chan D.C. and Sheedy K. P., Turbulent Flow Modelling of a Three Dimensional Turbine, AIAA Paper no. 90-2024, 1990.

Chen H. C. and Patel V. C., Near-wall Turbulence Models for Complex Flow Including Separation, AIAA Journal, Vol. 26, no. 6, 1988, pp 641-648.

Chia-Shun Y., Fluid Mechanics, McGraw-Hill, 1969.

Chima R. V., Development of and Explicit Multigrid Algorithm for Quasi-Three-Dimensional Flows in Turbomachinery, AIAA Paper no. 86-0032, 1986.

Connor J. J., Finite Element Techniques in Fluid Flow, Butterworths, 1976.

Crawford M. E. and Kays W. M., STAN 5 – A Program for Numerical Computation of Two-Dimensional Internal and External Boundary Layer Flows, NASA CR 2742, 1974.

Cuvelier C., Segal A. and Von Steenhoven A. A., Finite Element Methods and the Navier-Stokes Equations, D Reidel, 1986.

Daniels L. C., Film Cooling of Gas Turbine Blades, PhD Thesis, Department of Engineering Science, University of Oxford, England, 1978.

Daniels L. D. and Browne W. B., Calculation of Heat Transfer Rates to Gas Turbine Blades, International Journal of Heat and Mass Transfer, Vol. 24, no. 5, 1981, pp 871-879.

De Villiers J. E., Investigation of Heat Transfer Characteristics to in Hollow Turbine Blades, MScEng Year End Report, Department of Mechanical Engineering, University of Natal, South Africa, 2001.

Delaney R. A., Time-Marching Analysis of Steady Transonic Flow in Turbomachinery Cascades using the Hopscotch Method, ASME Paper no. 82-GT-152, 1982.

Dorney D. J. and Davis R. L., Navier-Stokes Analysis of Turbine Blade Heat Transfer and Performance, Journal of Turbomachinery, ASME, Vol. 114, 1992, pp 795-806.

Dring R. P., Joslyn H. D., Hardin L. W. and Wagner J. H., Turbine Rotor-Stator Interaction, Journal of Engineering for Power, ASME, Vol. 104, 1982, pp 729-742.

Dunn M. G. and Stoddard F. J., Measurement of Heat Transfer Rate to a Gas Turbine Stator, Journal of Engineering for Power, ASME, Vol. 101, 1979, pp 275-280.

Dunn M. G. and Hause A., Measurement of Heat Flux and Pressure in a Turbine Stage, Journal of Engineering for Power, ASME, Vol. 104, 1982, pp 215-223.

Dunn M. G., Rae W. J. and Holt J. L., Measurement and Analysis of Heat Flux Data in a Turbine Stage: Part I – Description of Apparatus and Data Analysis, Journal of Engineering for Power, ASME, Vol. 106, 1984, pp 229-233.

Dunn M. G., Rae W. J. and Holt J. L., Measurement and Analysis of Heat Flux Data in a Turbine Stage: Part II – Discussion of Results and Comparison with Predictions, Journal of Engineering for Power, ASME, Vol. 106, 1984, pp 234-240.

Dunn M. G., Bennet W. A., Delaney R. A and Rao K. V., Investigation of Unsteady Flow Through a Transonic Turbine Stage: Data / Prediction Comparison for Time Averaged and Phase Resolved Pressure Data, Journal of Turbomachinery, ASME, Vol. 114, 1992, pp 91-99.

Dunn M. G., Kim J., Civinskas K. C. and Boyle R. J., Time-Averaged Heat Transfer and Pressure Measurements and Comparison with Predictions for a Two Stage Turbine, Journal of Turbomachinery, ASME, Vol. 116, 1994, pp 14-22.

Dunn M. G., Convective Heat Transfer and Aerodynamics in Axial Flow Turbines, ASME Turbo Expo, New Orleans, Louisiana, USA, 4-7 June 2001.

Edwards D. K., Denny V. E. and Mills A. F., Transfer Processes: An Introduction to Diffusion, Convection and Radiation, 2nd Ed, McGraw-Hill.

FLUENT.INC, FLUENT 6.0 User's Guide, FLUENT 6.0 Documentation Suite.

FLUENT.INC, FIPREP User's Manual, FIDAP 8.60 Documentation Suite.

Frost W. and Moulden T. H., Handbook of Turbulence Vol. I: Fundamentals and Application, Plenum Press, 1977.

Gaugler R. E., Some Modifications to, and Operating Experiences with the Two-Dimensional Finite Difference, Boundary Layer Code STAN 5, ASME Paper no. 81-GT-89, 1981.

Goodier J. N. and Timoshenko S. P., Theory of Elasticity, McGraw-Hill, 1970

Graziani R. A., Blair M. F., Taylor J. R. and Mayle R. E., An Experimental Study of Endwall and Airfoil Surface Heat Transfer in a Large Scale Blade Cascade, Journal of Engineering for Power, ASME, Vol. 102, 1980, pp 257-267.

Hah C., A Navier-Stokes Analysis of Three-Dimensional Turbulent Flows Inside Turbine Blade Rows at Design and Off Design Conditions, Journal of Engineering for Gas Turbines and Power, ASME, Vol. 106, 1984, pp 421-429.

Hah C., Numerical Study of Three-Dimensional Flow and Heat Transfer Near the Endwall of a Turbine Row, AIAA Paper no. 89-1989, 1989.

Hetnarski R. B., Thermal Stresses Vols. I – III, Mechanics and Mathematical Methods, North Holland, 1986.

Hinze J. O., Turbulence, McGraw-Hill, 1959.

Hodson H. P., Boundary Layer Separation Near the Leading Edge of a High-Speed Turbine Blade, Journal of Engineering for Gas Turbines and Power, ASME, Vol. 107, 1985, pp 127-134.

Hylton L. D., Milhec M. S., Turner E. R, Nealy D. A. and York R. E., Analytical and Experimental Evaluation of the Heat Transfer Distribution Over the Surfaces of Turbine vanes, NASA CR 168015, 1983.

Incropera F. P. and De Witt D. P., Fundamentals of Heat and Mass Transfer, 3rd Ed., Wiley and Son, 1990.

Jones W. P. and Launder B. E., The Calculation of Low Reynold's Number Phenomena using a Two-Equation Model of Turbulence, International Journal of Heat and Mass Transfer, Vol. 16, 1973, pp 1119-1129.

Joslyn D. and Dring R., Three-Dimensional Flow in an Axial Turbine: Part I – Aerodynamic Mechanisms, Journal of Turbomachinery, ASME, Vol. 114, 1992, pp 61-70.

Joslyn D. and Dring R., Three-Dimensional Flow in an Axial Turbine: Part II – Profile Attenuation, Journal of Turbomachinery, AMSE, Vol. 114, 1992, pp 71-78.

Kader B., Temperature and Concentration Profiles in Fully Turbulent Boundary Layers, International Journal of Heat and Mass Transfer, Vol. 24, no. 9, 1993, pp 1541-1544.

Lam C. K. G. and Bremhorst K., A Modified Form of the k-ε Turbulence Model for Predicting Wall Turbulence, Journal of Fluids Engineering, ASME, Vol. 103, 1981, pp 456-460.

Langston L. S., Nice M. L. and Hooper R. M., Three-Dimensional Flow within a Turbine Cascade, Journal of Engineering for Power, ASME, Vol. 99, 1977, pp 21-28.

Launder B. E. and Spalding D. B., Lectures in Mathematical Models of Turbulence, Academic Press, 1972.

Lee D. and Knight C. J., Evaluation of an O-H Grid Formulation for Viscous Cascade Flows, AIAA Paper no. 89-0207, 1989.

Maya T., Katsumata I. and Itoh M., The Study of Thermal Fatigue Life Prediction of Air-Cooled Turbine Blades, ASME paper no. 78-GT-58, 1978.

Mayle R. E., The Role of Lamina-Turbulent Transition in Gas Turbine Engines, Journal of Turbomachinery, ASME, Vol.113, 1991, pp 509-537.

Menter F. R., Two-Equation Eddy-Viscosity Turbulence Models for Engineering Applications, AIAA Journal, Vol. 32, no. 8, pp 1598-1605.

Moll W., Anwendung der Schaufelkuhlung fur Leitsscfaufeln von Hochtemperaturgasturbein, Dissertation, RWTH, Aachen, 1990.

Moore J. and Moore J. G., Performance Evaluation of Linear Gas Turbine Cascades using Three-Dimensional Viscous Flow Calculations, Journal of Engineering for Gas Turbines and Power, ASME, Vol. 107, 1985, pp 969-975.

Moore J. and Ransmayr A., Flow in a Turbine Cascade: Part I – Losses and Leading Edge Effects, Journal of Engineering for Gas Turbine and Power, ASME, Vol. 106, 1984, pp 400-408.

Myers G. E., Analytical Methods in Conduction Heat Transfer, Genium, 1987.

Nealy D. A., Milhec M. S., Hylton L.D. and Gladden H. J., Measurements of Heat Transfer Distribution Over the Surfaces of Highly Loaded Turbine Nozzle Guide Vanes, Journal of Engineering for Power, ASME, Vol. 106, 1984, pp 149-158.

Osisik M. N., Heat Conduction, Wiley, 1980.

Patankar S. V. and Spalding D. B., Heat and Mass Transfer in Boundary Layers, 2nd Ed., Intertext, London, 1970.

Patankar S. V., Numerical Heat Transfer and Fluid Flow, McGraw-Hill.

Patel V. C., Rodi W. and Scheuerer G., Turbulence Models for Near-Wall and Low Reynold's Flows: A Review, AIAA Journal, Vol. 23, no. 9, 1985, pp 1309-1319.

Prandtl L., Fluid Dynamics, Blachie and Son, 1969.

Rai M. M., Unsteady Three-Dimensional Navier-Stokes Simulations of Turbine Rotor-Stator Interaction Including Tip Effects, AIAA Paper no. 87-2058, 1987.

Rao K. V. and Delaney R. A., Investigation of Unsteady Flow Through a Transonic Stage, Part I – Analysis, AIAA Paper no. 90-2408, 1990.

Rhie C. M. and Chow W. L., Numerical Study of the Turbulent Flow Past and Airfoil with Trailing Edge Separation, AIAA Journal, Vol. 21, no. 11, 1983, pp 1525-1532.

Rodi W. and Scheuerer G., Calculation of Heat Transfer to Convection-Cooled Turbine Blades, Journal of Engineering for Gas Turbines and Power, ASME, Vol. 107, 1985, pp 620-627.

Roshenow W. M., Hartnet J. P. and Ganic E. N., Handbook of Heat Transfer fundamentals, 3rd Ed., McGraw-Hill.

Schlichting H., Boundary Layer Theory, Pergamon, 1955.

Schmidt R. C. and Patankar S. V., Simulating Boundary Layer Transition with a Low-Reynold's Number k-ε Turbulence Model: Part I – An Evaluation of Prediction Characteristics, Journal of Turbomachinery, ASME, Vol. 103, 1991, pp 10-17.

Schmidt R. C. and Patankar S. V., Simulating Boundary Layer Transition with a Low-Reynold's Number k-ε Turbulence Model: Part II – An Approach to Improving Predictions, Journal of Turbomachinery, ASME, Vol. 103, 1991, pp 18-26.

Sharma O. P., Pickett G. F. and Ni R. H., Assessment of Unsteady Flows in Turbines, Journal of Turbomachinery, ASME, Vol. 114, 1992, pp 79-90.

Shih T. H., Liou W. W., Shabbir A. and Zhu J., A New k-ε Eddy Viscosity Model for High Reynold's Number Turbulent Flows – Model Development and Validation, Computers Fluids, Vol. 24, no. 3, 1995, pp 227-238.

Singh R., Managing Gas Turbine Availability, Performance and Life Usage via Advanced Diagnostics, 44th Gas Turbine Users Association Annual Conference, Dubai, UAE, 9-14 May, 1999.

Spalart P. and Allmaras S., A One-Equation Model for Aerodynamic Flows, AIAA Paper no. 92-0439, 1992.

Swaminathan V. P. and Allen J. M., Surface Degradation and Cracking in Gas Turbine Blade Cooling Passages, 124th Annual Meeting and Exposition, TSM, Las Vegas, Nevada, 1995.

Temam R., Navier-Stokes Equations, Studies in Mathematics and its Application, Vol. 2, North-Holland, 1977.

Turner A. B., Local Heat Transfer Measurements and a Gas Turbine Blade, Journal of Mechanical Engineering science, Vol. 13, 1971, pp 1-12.

Wang J. H., Jen F. H. and Hartel O. E., Airfoil Heat Transfer Calculation Using a Low Reynold's Number Version of a Two-Equation Turbulence Model, Journal of Engineering for Gas Turbines and Power, ASME, Vol. 107, 1985, pp 60-67.

White F. M., Viscous Fluid Flow, McGraw-Hill, 1974.

Wilcox D. C., Turbulence Model Transition Predictions, AIAA Journal, Vol. 13, no. 2, 1975, pp 241-243.

Wilcox D. C., Turbulence Modelling for CFD, DCW Industries Inc., 1998.

Wolfstein M., The velocity and Temperature Distribution of a One-Dimensional Flow with Turbulence Augmentation and Pressure Gradient, International Journal of Heat and Mass Transfer, Vol. 12, 1995, pp 295-317.

Yakhot V. and Orszag S. A., Renormalization Group Analysis of Turbulence: I – Basic Theory, Journal of Scientific Computing, Vol. 1, no. 1, 1986, pp 1-51.

Zukausha A. and Slanciauskas A., Heat Transfer in Turbulent Flows, Experimental and Applied Heat Transfer Guide Books, Hemisphere, 1987.